

Conceptual Design of In-Space Vehicles for Human Exploration of the Outer Planets

*R.B. Adams, R.A. Alexander, J.M. Chapman, S.S. Fincher, R.C. Hopkins, A.D. Philips,
T.T. Polsgrove, R.J. Litchford, and B.W. Patton
Marshall Space Flight Center, Marshall Space Flight Center, Alabama*

*G. Statham and P.S. White
ERC, Inc., Huntsville, Alabama*

*Y.C.F. Thio
U.S. Department of Energy, Germantown, Maryland*

The NASA STI Program Office...in Profile

Since its founding, NASA has been dedicated to the advancement of aeronautics and space science. The NASA Scientific and Technical Information (STI) Program Office plays a key part in helping NASA maintain this important role.

The NASA STI Program Office is operated by Langley Research Center, the lead center for NASA's scientific and technical information. The NASA STI Program Office provides access to the NASA STI Database, the largest collection of aeronautical and space science STI in the world. The Program Office is also NASA's institutional mechanism for disseminating the results of its research and development activities. These results are published by NASA in the NASA STI Report Series, which includes the following report types:

- **TECHNICAL PUBLICATION.** Reports of completed research or a major significant phase of research that present the results of NASA programs and include extensive data or theoretical analysis. Includes compilations of significant scientific and technical data and information deemed to be of continuing reference value. NASA's counterpart of peer-reviewed formal professional papers but has less stringent limitations on manuscript length and extent of graphic presentations.
- **TECHNICAL MEMORANDUM.** Scientific and technical findings that are preliminary or of specialized interest, e.g., quick release reports, working papers, and bibliographies that contain minimal annotation. Does not contain extensive analysis.
- **CONTRACTOR REPORT.** Scientific and technical findings by NASA-sponsored contractors and grantees.

- **CONFERENCE PUBLICATION.** Collected papers from scientific and technical conferences, symposia, seminars, or other meetings sponsored or cosponsored by NASA.
- **SPECIAL PUBLICATION.** Scientific, technical, or historical information from NASA programs, projects, and mission, often concerned with subjects having substantial public interest.
- **TECHNICAL TRANSLATION.** English-language translations of foreign scientific and technical material pertinent to NASA's mission.

Specialized services that complement the STI Program Office's diverse offerings include creating custom thesauri, building customized databases, organizing and publishing research results...even providing videos.

For more information about the NASA STI Program Office, see the following:

- Access the NASA STI Program Home Page at <http://www.sti.nasa.gov>
- E-mail your question via the Internet to help@sti.nasa.gov
- Fax your question to the NASA Access Help Desk at (301) 621-0134
- Telephone the NASA Access Help Desk at (301) 621-0390
- Write to:
NASA Access Help Desk
NASA Center for AeroSpace Information
7121 Standard Drive
Hanover, MD 21076-1320
(301)621-0390



Conceptual Design of In-Space Vehicles for Human Exploration of the Outer Planets

*R.B. Adams, R.A. Alexander, J.M. Chapman, S.S. Fincher, R.C. Hopkins, A.D. Philips,
T.T. Polsgrove, R.J. Litchford, and B.W. Patton
Marshall Space Flight Center, Marshall Space Flight Center, Alabama*

*G. Statham and P.S. White
ERC, Inc., Huntsville, Alabama*

*Y.C.F. Thio
U.S. Department of Energy, Germantown, Maryland*

National Aeronautics and
Space Administration

Marshall Space Flight Center • MSFC, Alabama 35812

Acknowledgments

Thanks to Jeff Dunnivant and Harvey Jackson for computer and networking support during the execution of this project. Our sister teams at Langley Research Center and Glenn Research Center provided valuable insight and technical support. Finally, our heartfelt appreciation goes to the Revolutionary Aerospace Systems Concepts activity for funding our efforts for this interesting and enlightening project.

TRADEMARKS

Trade names and trademarks are used in this report for identification only. This usage does not constitute an official endorsement, either expressed or implied, by the National Aeronautics and Space Administration.

Available from:

NASA Center for AeroSpace Information
7121 Standard Drive
Hanover, MD 21076-1320
(301) 621-0390

National Technical Information Service
5285 Port Royal Road
Springfield, VA 22161
(703) 487-4650

TABLE OF CONTENTS

1. INTRODUCTION	1
2. DESCRIPTION	3
2.1 Mission Definition	3
2.2 Selected Destination	4
2.3 Propulsion and Power Technologies	6
2.4 Vehicle Subsystem Design	19
2.5 Magnetized Target Fusion Engine Development	38
2.6 Vehicle Design	64
3. CONCLUSIONS AND RECOMMENDATIONS	90
APPENDIX A—ELEMENTARY MAGNETIZED TARGET FUSION MAGNETIC NOZZLE THEORY	95
A.1 Initial Plasma Shell Conditions	109
A.2 Initial Magnetic Flux Derivation	110
APPENDIX B—MAGNETOHYDRODYNAMIC POWER SYSTEM MODEL	112
REFERENCES	117

LIST OF FIGURES

1.	Organization of RASC FY 2002 activities	1
2.	Relative positions of Earth-Moon Lagrange points	3
3.	Plasma jets converging on the magnetized target plasma	7
4.	Detail of an individual plasma jet	7
5.	Sequence of events during compression and fusion	8
6.	Plasma cloud expansion following the fusion burn in the target and inner liner	8
7.	Nozzle magnetic field configuration (a) at fusion and (b) after plasma expansion	9
8.	MPD thruster cross section	10
9.	LMR conversion system	12
10.	LMR system NEP vehicle layout	12
11.	Schematic for MHD power and propulsion system	16
12.	Transhab configuration and layout	19
13.	Configuration of the surface habitat in (a) the stowed position and (b) in the inflated position. Living area uses inflation technology similar to Transhab	20
14.	Configuration of the crewed lander	21
15.	ISRU configuration and deployment. Reactors must be positioned away from the ISRU before commencement of operations	22
16.	Dimensions and configuration of expendable launch vehicle fairing assumed for this study	23
17.	Gaseous oxygen/gaseous hydrogen RCS with liquid propellant storage	24
18.	Schematic of power conversion and engine thermal control systems	25

LIST OF FIGURES (Continued)

19.	Reactor shield dimensions	28
20.	Penalty for low thrust in escape maneuver from satellite orbit, as compared to impulsive thrust (tangentially directed thrust)	31
21.	Effects of artificial gravity	32
22.	HOPE vehicle configuration	35
23.	HOPE vehicle overall dimensions (side view)	35
24.	HOPE vehicle aft end detail	36
25.	HOPE vehicle forward end detail	37
26.	Typical location of MPD thrusters and PMU systems	38
27.	Conical theta pinches, spheromak creation and merging to form an FRC plasmoid	39
28.	A spheromak plasmoid	39
29.	Two spheromaks about to merge—note opposing toroidal magnetic field directions	40
30.	FRC plasmoid formed from two merged spheromaks	40
31.	Region of MTF nozzle available for plasma gun location	41
32.	Plasma gun schematic design	41
33.	Plasma gun barrel design	42
34.	Location and orientation of plasma guns relative to the coils	43
35.	MTF nozzle coil assembly cross section	45
36.	Location of major components	47
37.	MTF thermal management schematic	51
38.	Recharge system schematic	52
39.	SMES charging circuit	53

LIST OF FIGURES (Continued)

40.	Transmission line cross section	54
41.	Propellant storage and supply system	56
42.	MCNP representation of neutron shield geometry	60
43.	MTF engine configuration (iso view)	61
44.	MTF engine coils and plasma guns (detail)	62
45.	MTF engine coils and plasma guns locations (top view)	62
46.	MTF engine overall dimensions (front view)	63
47.	MTF engine configuration (top view)	63
48.	RASC HOPE design process data flow	64
49.	Trajectory graph for D-D MTF 30-day stay option	75
50.	Trajectory graph for D-D MTF 180-day stay option	76
51.	Vehicle layout for D-D MTF 180-day stay option	77
52.	Vehicle dimensions for D-D MTF 180-day stay option	78
53.	Trajectory graph for D-He3 MTF 180-day stay option	79
54.	Vehicle layout for D-He3 MTF 180-day stay option	80
55.	Vehicle dimensions for D-He3 MTF 180-day stay option	80
56.	Trajectory graph for MSR–LMR–MPD 120-day stay option	83
57.	Piloted vehicle layout for MSR–LMR–MPD 120-day stay option	84
58.	Piloted vehicle dimensions for MSR–LMR–MPD 120-day stay option (side view)	84
59.	Cargo vehicle layout for MSR–LMR–MPD 120-day stay option	85
60.	Cargo vehicle dimensions for MSR–LMR–MPD 120-day stay option (side view)	85
61.	Trajectory graph for SCR–MHD–MPD 120-day stay option	87

LIST OF FIGURES (Continued)

62.	Piloted vehicle layout for SCR–MHD–MPD 120-day stay option	88
63.	Piloted vehicle dimensions for SCR–MHD–MPD 120-day stay option (side view)	88
64.	Cargo vehicle layout for SCR–MHD–MPD 120-day stay option	89
65.	Cargo vehicle dimensions for SCR–MHD–MPD 120-day stay option (side view)	89
66.	Cumulative dose for the MTF 30-day D-D mission to Callisto	91
67.	Cumulative dose for the LaRC and GRC VASIMR mission to Callisto	92
68.	Nozzle magnetic field at fusion burn	95
69.	Nozzle magnetic field shortly after fusion burn	96
70.	Nozzle magnetic field at maximum plasma expansion	97
71.	Nozzle magnetic field geometry	98
72.	Diagram illustrating cone surface area	98
73.	Diagram illustrating an element of a plasma shell	99
74.	Geometry of a plasma element shown in (a) the φ dimension and (b) a cross-sectional view	100
75.	Isotropy of plasma expansion	102
76.	Plasma element for numerical analysis: (a) Coil and polar angle numbering system and (b) element of plasma associated with the i th coil	103
77.	Axial and radial directions	104
78.	Magnetic field configuration (a) before and (b) after compression	105
79.	Coil dimensions	107
80.	Stages of magnetic field compression	108
81.	Division of plasma shell into discrete segments	108
82.	Open portion of nozzle	109

LIST OF TABLES

1.	Comparison of MMW space reactor types	18
2.	Medium-temperature radiator analysis results summary	26
3.	High-temperature radiator analysis results summary	27
4.	Weight breakdown of the power system	29
5.	Quantitative comparison of methods for inducing artificial gravity	32
6.	Qualitative comparison of methods for inducing artificial gravity	33
7.	MTF nozzle coil assembly dimensions	45
8.	Transmission line cross-section dimensions	54
9.	MTF device mass summary	57
10.	MTF device performance summary	58
11.	Vehicle mass and power breakdown (MTF options)	67
12.	Vehicle mass and power breakdown (MSR–LMR–MPD option)	70
13.	Vehicle mass and power breakdown (SCR–MHD–MPD option)	72
14.	D-D MTF 30-day stay summary information	74
15.	D-D MTF 30-day stay mission timeline	74
16.	D-D MTF 180-day stay summary information	75
17.	D-D MTF 180-day stay mission timeline	76
18.	D-He3 MTF 180-day stay summary information	78
19.	D-He3 MTF 180-day stay mission timeline	79
20.	MSR–LMR–MPD 120-day stay summary information	81

LIST OF TABLES (Continued)

21.	MSR–LMR–MPD 120-day stay mission timeline	82
22.	SCR–MHD–MPD 120-day stay summary information	86
23.	SCR–MHD–MPD 120-day stay mission timeline	86
24.	Low-level parameters	116

LIST OF ACRONYMS AND SYMBOLS

ALKSYS	a computer program for studies of Rankine-cycle space nuclear power systems
ANP	Aircraft Nuclear Program
BN	boron nitride
CAD	computer-aided design
Cermet	uranium-tungsten
^2D	deuterium nucleus
D-D	deuterium-deuterium
D-He3	deuterium-helium-3
D-T	deuterium-tritium
ET	electrothermal
ETO	Earth-to-orbit
F	iron
FLiBe	fluorine lithium beryllium (a molten mixture of lithium fluoride and beryllium fluoride)
FRC	field reverse configuration
GH_2	gaseous hydrogen
gox	gaseous oxygen
GRC	Glenn Research Center
^3He	helium-3 nucleus
^4He	helium-4 nucleus

LIST OF ACRONYMS AND SYMBOLS (Continued)

H ₂ O	water
HOPE	human outer planet exploration
HTGR	high temperature gas reactor
HX	heat exchanger
HZTERN	heavy ion transport code
IML1	initial mass at Lagrange 1 point
ISRU	in situ resource utilization
JPL	Jet Propulsion Laboratory
K	potassium
L1	Lagrange 1 point
LaRC	Langley Research Center
LH ₂	liquid hydrogen
Li	lithium
LMR	liquid metal Rankine
LN ₂	liquid nitrogen
lox	liquid oxygen
LVA	launch vehicle analysis
MCNP	Monte Carlo transport code
MHD	magnetohydrodynamic
MMW	multimegawatt
MMW(e)	multimegawatt electric

LIST OF ACRONYMS AND SYMBOLS (Continued)

MO	molybdenum
MPD	magnetoplasdynamic
MSFC	Marshall Space Flight Center
MSR	molten salt reactor
MSRE	molten salt reactor experiment
MTF	magnetized target fusion
MW _{th}	megawatt-thermal
^1_0n	neutron
Na	sodium
NEP	nuclear electric propulsion
^1_1p	proton
PBR	pebble bed reactor
PMAD	power management and distribution
PPU	power processing unit
PR	pressure regulator
RASC	Revolutionary Aerospace Systems Concepts
RCS	reaction control system
SCR	solid core reactor
SEPTOP	Solar Electric Propulsion Trajectory Optimization Program (computer program)
SMES	superconducting magnetic energy storage
^3_1T	tritium nucleus

LIST OF ACRONYMS AND SYMBOLS (Continued)

TiB ₂	titanium diboride
TP	Technical Publication
UC	uranium carbide
UF ₄	uranium tetrafluoride
UN	uranium nitride
VARITOP	Variational Calculus Trajectory Optimization Program (computer program)
VASIMR	variable specific impulse magnetoplasma rocket
VISTA	vehicle for interplanetary space transport applications
ZBO	zero boiloff
Zr	zirconium
ZrB ₂	zirconium diboride

NOMENCLATURE

A	area; current amplification factor
A_{con}	area of a conical annulus
A_s	radiator surface area
a	distance between parabola focus and directrix; coil cross-sectional radius
a_0	distance between focus and directrix of initial parabola
$a_i(t)$	parabola constant for the i th segment
a_j	cross-sectional radius
a_L	distance between limiting parabola focus and directrix
B	magnitude of magnetic field
\mathbf{B}	applied magnetic field
$B_i(t)$	magnetic field for the i th plasma segment at time
c	speed of light in a vacuum
c_p	specific heat at constant pressure
d	plasma
$d\mathbf{A}$	vector surface area
$d\mathbf{F}$	force acting on an incrementally small element of plasma shell
dM	mass of plasma
$d\Omega$	solid angle subtended by the element at the focus
E	energy
E_B	magnetic field energy

NOMENCLATURE (Continued)

$E_{B,c}$	total magnetic field energy of all coils after compression
$E_{B,s}$	total magnetic field energy of all coils before compression
E_{cpT}	total charged particle kinetic energy
E_{cpu}	useful charged particle kinetic energy
e	electronic charge
e	element
e _{axial}	unit vector in the axial direction
e _{radial}	unit vector in the radial direction
e _{<i>r</i>}	unit vector in the <i>r</i> direction
e _{<i>θ</i>}	unit vector in the <i>θ</i> direction
e _{<i>φ</i>}	unit vector in the <i>φ</i> direction
F	force
F _{<i>i</i>}	total force experienced by coil <i>i</i>
<i>h</i>	height; specific enthalpy
<i>I</i>	electrical current
$I_{c,j}$	maximum current
$I_{s,j}$	initial current
I_{sp}	specific impulse
<i>i</i>	coil
J	current density
J _{<i>F</i>}	Faraday current density
J _{<i>H</i>}	Hall current density

NOMENCLATURE (Continued)

j	coil
j_c	current density
L	electrical inductance
$L_{c,j}$	inductance at peak magnetic compression
$L_{s,j}$	initial induction
M	total mass of plasma
M_{coil}	generator coil
M_{comp}	compressors
M_{regen}	regenerator
M_{struc}	generator structure
m	working fluid
N	discrete segments
N_c	number of compressor stages
n	integer
P_{gen}	generator power density
P_o	total pressure
p_B	magnetic pressure
$p_{Bi}(t)$	magnetic pressure at segment i
Q	rate of heat transfer
Q_{heat}	heat absorbed by working fluid from nuclear reactor
Q_{regen}	heat transferred by the regenerator

NOMENCLATURE (Continued)

q	radiative heat loss rate
R	coil major radius; pressure ratio
R_j	major radius of coil j
r	radius
r_L	radial coordinate of limiting parabolic surface
r_{\max}	maximum radius
r_{\min}	minimum radius
s_t	structural material working stress
T	temperature
T_{\max}	maximum temperature that the working fluid reaches in the reactor
T_{\min}	minimum temperature of the working fluid
T_o	ambient temperature
T_{rej}	rejection temperature
T_s	radiator surface temperature
t	time
\mathbf{U}	fluid velocity
U_{regen}	heat transfer coefficient
\mathbf{v}	velocity
v_{ri}	initial plasma speed in a radial manner away from the focus
W	watt
W_{comp}	electrical power required to run the compressors

NOMENCLATURE (Continued)

W_{gen}	total electrical power generated
α	mass per unit power values
α_{coil}	magnetohydrodynamic generator coil mass per unit net power generated
α_{comp}	compressor mass per unit power required by to operate the compressors
α_{regen}	thermal regenerator mass per unit heat transferred across the regenerator
α_{struc}	magnetohydrodynamic generator structural mass per unit net power generated
α_{tot}	overall mass per unit power
β_{regen}	regenerator mass per unit area
Γ_1	substitution variable
Γ_2	substitution variable
Γ_3	substitution variable
γ	ratio of specific heats
ΔE_B	energy input to magnetic field due to plasma expansion
ΔT_{LMD}	log-mean temperature difference
ΔV	change in velocity (delta-v)
ε	emissivity
$\varepsilon_{\text{regen}}$	regenerator effectiveness
η_N	enthalpy extraction ratio
$\eta_{s,c}$	isentropic efficiency of a compressor stage
θ	angle
μ	magnetic permeability

NOMENCLATURE (Continued)

μ_0	permeability of free space
ρ	plasma mass density
ρ_c	mass density of the coil material
σ	Stefan-Boltzmann constant; conductivity
Φ	magnetic flux
φ	azimuthal angle
Ω	solid angle

TECHNICAL PUBLICATION

CONCEPTUAL DESIGN OF IN-SPACE VEHICLES FOR HUMAN EXPLORATION OF THE OUTER PLANETS

1. INTRODUCTION

Administrator Daniel Goldin initiated the Revolutionary Aerospace Systems Concepts (RASC) activity that started in FY 2001 to address conceptual design of systems and architectures for potential missions 25–40 yr in the future. The goal of these designs is to determine the technologies and infrastructure necessary to enable those missions. Consequently, the RASC studies were intended to take a top-down approach.

In FY 2002, the RASC activity, managed from the Langley Research Center (LaRC), selected a broad range of projects for the year's activities. These projects were collected in five groups, as shown in figure 1. Marshall Space Flight Center (MSFC) participated in two of these groups. MSFC participation was led from TD30/Advanced Concepts. The work completed for Group 4—In-Space Remote Sensing—is documented in another Technical Publication (TP). MSFC participation in Group 2 activities is documented in this TP.

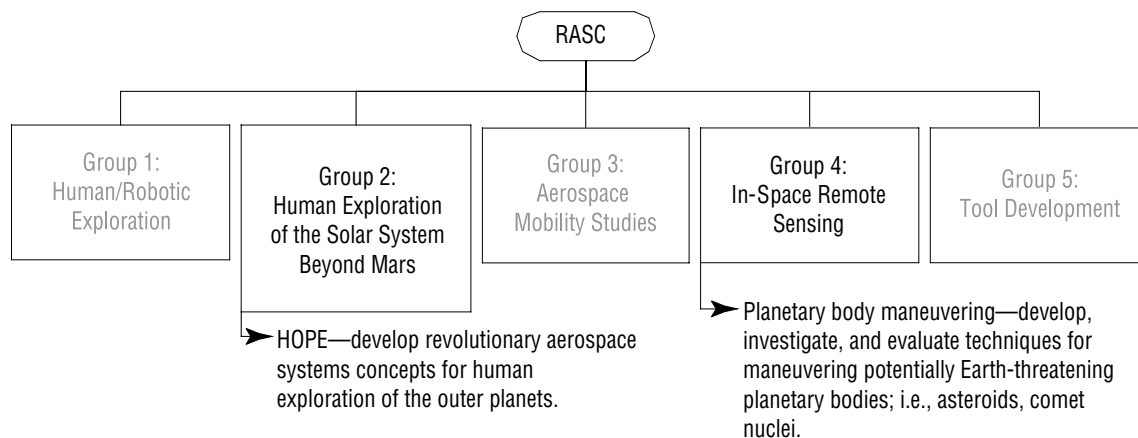


Figure 1. Organization of RASC FY 2002 activities.

In FY 2002, RASC organized the Human Outer Planet Exploration (HOPE) group to investigate the possibility of crewed travel to the outer solar system. Three scenarios were considered: (1) Nuclear thermal propulsion using both crewed vehicles and robotic support vehicles, (2) nuclear electric propulsion (NEP) also using crewed vehicles and robotic support vehicles, and (3) fusion propulsion using crewed

vehicles only. The outer solar system—from the asteroid belt outwards—was surveyed to select a suitable destination point. Using assumptions on requirements and available technology, three different Centers (Glenn Research Center (GRC), LaRC, and MSFC) designed vehicles to support a crewed trip to the chosen outer solar system destination. The emphasis in this study was to improve understanding of the major challenges associated with such missions. It is hoped that work on addressing these issues can commence in the near future.

This TP outlines the work done by the MSFC team for this study. Five concept missions were generated. The first three mission concepts used the magnetized target fusion (MTF) propulsion system with either deuterium-deuterium (D-D) or deuterium-helium-3 (D-He3) propellant and with 30- or 180-day stay times on Callisto. The fourth option used a magnetoplasmadynamic (MPD) thruster assembly powered by a molten salt reactor (MSR) with a liquid-metal Rankine (LMR) cycle power conversion system. The fifth option also used MPD thrusters, but this time powered by a solid core reactor (SCR) and magnetohydrodynamic (MHD) power conversion system. The last two options were split missions; i.e., two vehicles were involved. One vehicle carried the crew and crew support equipment, and the other carried all other cargo necessary for the mission.

Methods, calculations, and assumptions are presented in sufficient detail to allow the reader to reproduce the results. Section 2.3 defines the power and propulsion technologies discussed above. Section 2.4 describes the models used for all other vehicle subsystems and applies to both the MTF and MPD options. Section 2.5 describes, in detail, the effort expended on this study to refine the MTF propulsion system concept. Section 2.6 illustrates the vehicles designed to meet the five mission concepts. Some discussion is given on the efforts of the other Centers as they pertain to MSFC's work. The work of the other Centers is documented in other publications.¹⁻³

2. DESCRIPTION

2.1 Mission Definition

The HOPE task in the RASC activity had a simply stated goal: the conceptual design of a crewed vehicle intended to launch from the Earth-Moon Lagrange 1 point (L1), travel to the outer solar system, conduct valuable research and exploration, and then return safely to L1.

Figure 2 illustrates the position of the Lagrange points relative to the Earth and Moon. A LaRC-led team developed a conceptual design for an orbiting station at L1 during the previous fiscal year's RASC activities.

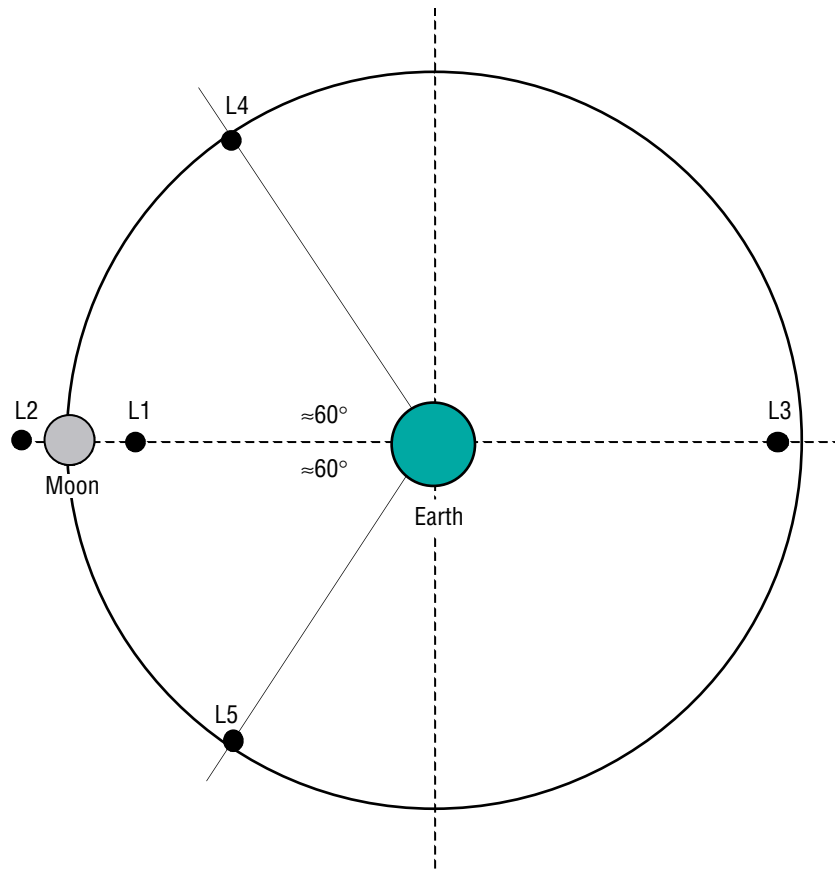


Figure 2. Relative positions of Earth-Moon Lagrange points.⁴

The HOPE task endeavored to answer the following questions pertaining to exploration of the outer planets:

- Which bodies in the outer solar system are the most attractive for a crewed landing?
- What robotic missions would be necessary and desirable preceding a crewed mission?
- Which propulsion technologies would most effectively handle the strenuous requirements for such a mission?
- What would such a vehicle look like, and what would be the major design drivers?

By answering these questions, the technologies necessary to conduct such a mission would be identified.

In the following pages, MSFC's contribution to the overall project is documented. The MSFC team participated in the destination discussions, and the data and results are reviewed in section 2.2. The physical principles behind the propulsion and power concepts used in the MSFC conceptual designs are examined in section 2.3. The theories underlying other vehicle subsystems, disciplines, and the issues that arose during the design process are discussed in section 2.4. Section 2.5 reviews the MSFC work in the development of the MTF engine, the primary propulsion system in most of our designs. Finally, section 2.6 reviews the completed vehicle designs in depth. The major lessons learned are summarized and briefly discussed in section 3.

2.2 Selected Destination

A number of candidate destinations were considered before the final selection was made. The major selection criteria can be summarized as follows:

- The destination should be a body in the outer solar system, here defined as being beyond the orbit of Mars.
- It should be suitable for human surface exploration.
- It should contain some features of legitimate scientific interest.
- The requirement for human surface exploration ruled out any of the gas giant planets—Jupiter, Saturn, Uranus, and Neptune—but not their extensive satellite systems.
- The destination should present a suitable level of challenge to the design team.

Amongst the short-listed candidates were the following bodies:

- Ceres—the largest asteroid, whose diameter is almost 1,000 km, and which is located in the main belt. Scientific interest is largely focused on determining the composition and structure of asteroids as

a key to understanding the formation and development of the solar system. Asteroid mining and planetary defense considerations prompt additional interest. Due to its relatively close proximity and low mass, Ceres presents a simpler set of design challenges than more distant destinations.

- Europa—Jupiter’s smallest Galilean satellite and the second closest to the planet. Scientific interest is largely prompted by the likely presence of a submerged ocean with tidal heating, which could offer conditions conducive to the development of life. Europa’s location within the Jovian radiation belts poses significant design problems, particularly when contemplating human surface exploration.
- Callisto—the second-largest Galilean satellite and the most distant from Jupiter. Scientific interest is prompted by the possibility of subsurface water. Callisto’s distance from Jupiter places it in a significantly less hazardous radiation environment than Europa, potentially permitting human surface operations.
- Titan—the largest satellite of Saturn and one of the largest in the solar system. Scientific interest is considerable, in part because Titan appears to be more complex than other satellites, with a significant and opaque atmosphere, possibly offering conditions conducive to the development of life. The relative remoteness of Saturn is offset by the absence of any significant radiation belts.
- Chiron—an unusual minor planet, following an eccentric orbit with perihelion just outside the orbit of Saturn and aphelion just within that of Uranus. Scientific curiosity is prompted by Chiron’s visible coma and variable brightness that appear to indicate that volatile compounds are being vaporized from this, in other respects, asteroid-like body. It is hypothesized that Chiron has only occupied its present orbit for a relatively short period, having been previously located in the (trans-Neptunian) Kuiper Belt. Access to Chiron could yield important data about the composition and structure of Kuiper Belt objects that are thought likely to be remnant objects from the solar system’s formation. Chiron’s remoteness and low temperature would pose significant technical problems.
- Triton—the largest satellite of Neptune and the only significant satellite in the solar system that follows a retrograde orbit. Scientific interest is due to its continuing seismic activity, as manifested by several ice volcanoes, and the likelihood that Triton is a Kuiper Belt object, captured by Neptune in the relatively recent past. Triton’s remoteness and low temperature pose significant design challenges.

The Jovian moon Callisto was selected because of the balance that it offers concerning scientific interest, design challenge severity, and the level of hazard to human operations posed by the local environment.

2.3 Propulsion and Power Technologies

2.3.1 Magnetized Target Fusion

MTF is a propulsion technique that combines features from both inertial and magnetic confinement fusion approaches and capitalizes on research results in both areas.⁵ The MTF technique offers the promise of both high specific impulse (I_{sp}) and low dry mass; therefore, it is well suited to the demands of high ΔV travel to the outer solar system, including missions of human exploration.

This section consists of a brief overview of the basic physical processes involved in MTF operation. For the purposes of this description, the main fusion fuel is assumed to be deuterium. Engineering descriptions of the major MTF components and the propellant storage and supply system are given in section 2.5 together with an overall mass estimate and performance summary. A more advanced variant of the MTF system, using D-He3 as the main fusion fuel, is also introduced in section 2.5.

The MTF system operates as follows. A small plasma target comprised of the most easily ignitable fuel, a 50 percent deuterium and 50 percent tritium molar mixture, is compressed to fusion conditions by converging jets of high-speed plasma, produced by an array of electromagnetic pulsed plasma accelerators, also known as plasma guns. Energy released from the deuterium-tritium (D-T) reactions initiates D-D fusion reactions within the deuterium layer immediately surrounding the target. The use of a D-T target, which has a relatively low ignition temperature, makes the initial fusion burn relatively easy to initiate, but the main energy release comes from the D-D reactions in the surrounding layer. This minimizes the need for tritium, which is relatively scarce and expensive. It also minimizes the number of high-energy neutrons produced during fusion; the high-energy neutrons produced by the D-D reaction are of much lower energy than those created from D-T fusion—2.45 MeV as opposed to 14.1 MeV.

The energy released during fusion produces very rapidly expanding hot plasma. By initiating the fusion event within the confines of a carefully shaped magnetic nozzle, the plasma expands in a radial manner, compressing the surrounding field against the coils, and is redirected out of the nozzle along the axis to produce thrust.

The processes by which MTF has been proposed as a propulsive technique are illustrated conceptually in figures 3–6, none of which are to scale.

Figure 3 shows a cross section of the magnetized plasma target with the various high-speed plasma jets converging on it.

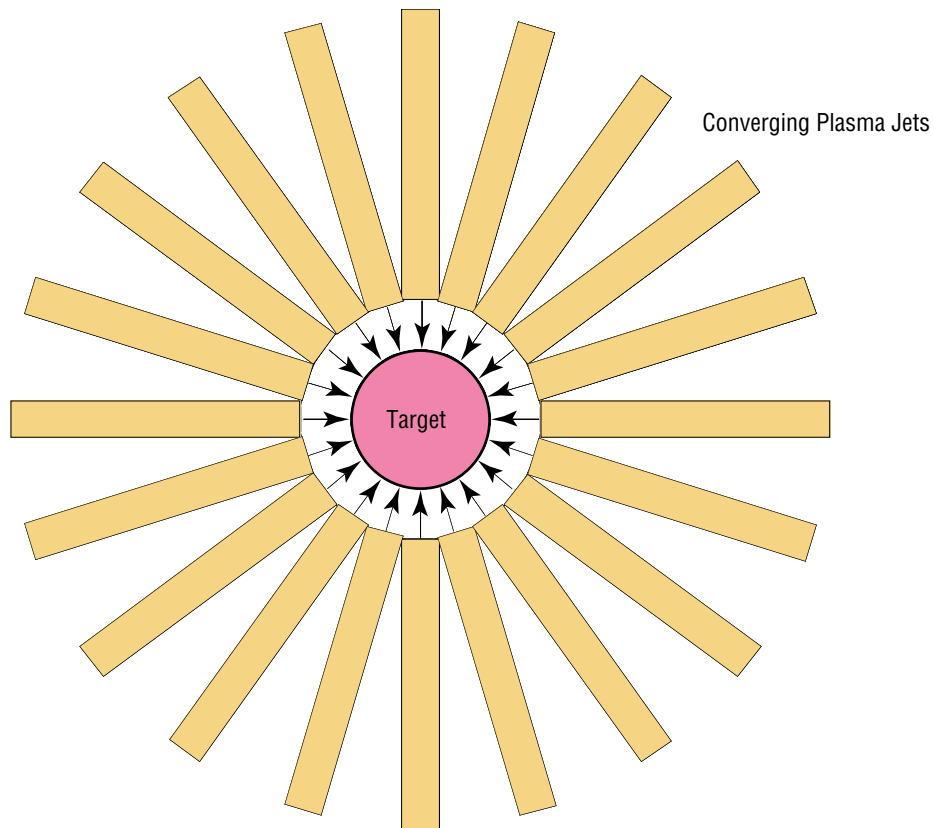


Figure 3. Plasma jets converging on the magnetized target plasma.

Figure 4 shows a single plasma jet in greater detail. The leading edge, proportionately exaggerated for clarity in the diagram, consists of deuterium plasma, and the remainder of the jet is comprised of hydrogen plasma. The jet is designed so that the plasma liner consists of an inner layer of fusible material surrounded by a neutron moderator. The presence of the hydrogen as a neutron moderator helps to shield the nozzle structure and also convert otherwise wasted neutron kinetic energy into useful charged-particle kinetic energy.

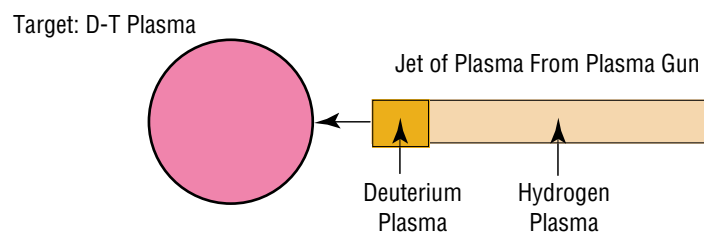


Figure 4. Detail of an individual plasma jet.

Figure 5 shows the plasmoid at three stages of the fusion process. The left-hand view shows the target and surrounding liner, formed when the individual plasma jets coalesce into a shell. The inner and outer liners, composed of deuterium and hydrogen plasma, respectively, are shown (the deuterium region is exaggerated in size). The central view shows the point at which conditions in the target initiate D-T fusion. The right-hand view shows the point at which the energy released from D-T fusion in the target initiates D-D fusion in the inner portion of the liner.

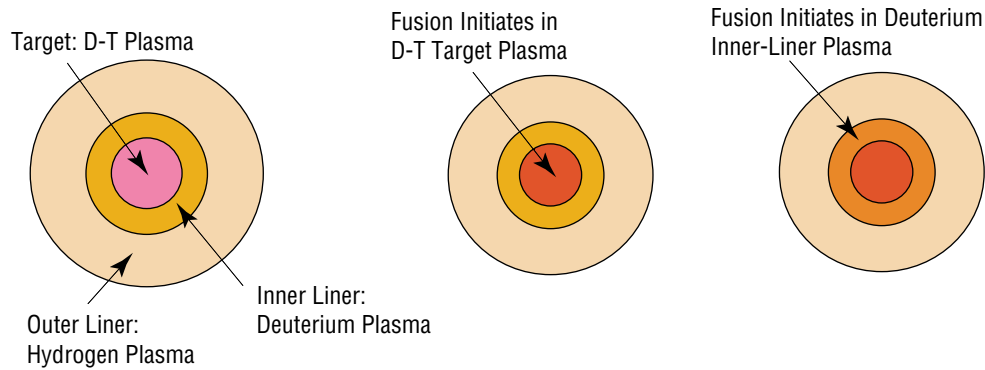


Figure 5. Sequence of events during compression and fusion.

Finally, figure 6 shows the hot plasma cloud expanding very rapidly. Fusion reactions in both the central target region and the inner liner have, at this point, ceased.

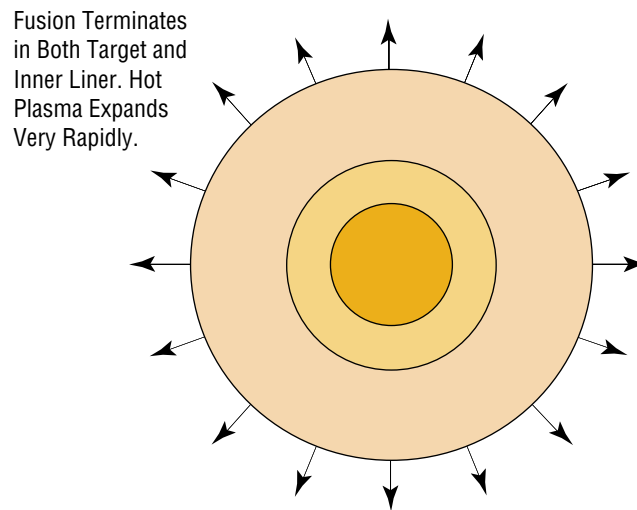


Figure 6. Plasma cloud expansion following the fusion burn in the target and inner liner.

Energy liberated during fusion, both in the target and the inner liner, appears in the form of particle kinetic energy. Charged-particle energy is transferred to useful impulse by means of a magnetic field formed by an array of current-carrying coils, which is initially (at the moment of fusion) configured, as shown in figure 7(a). As the plasma expands, the field lines are deformed, as shown in figure 7(b).

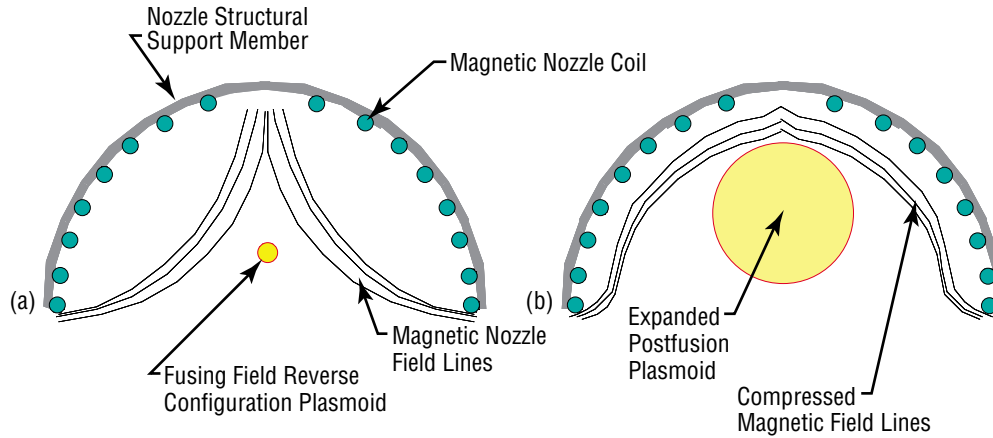


Figure 7. Nozzle magnetic field configuration (a) at fusion and (b) after plasma expansion.

Distortion and compression of the magnetic field occurs because its diffusion timescale—in the highly conductive plasma—is very long in comparison with the plasma expansion timescale. Currents are induced within the plasma cloud, and they serve to generate a magnetic field that, within the plasma, cancels the field that is due to the external coils. Outside the plasma, the field produced by these induced currents reinforces the field that is due to the coils. Hence, as it expands, the plasma cloud appears to sweep the magnetic field ahead of itself, compressing it and forcing it back towards the nozzle coils.

The initial kinetic energy of the expanding plasma cloud is transferred to potential energy in the compressed and deformed magnetic field. Note that the plasma expands freely through the lower, open portion of the nozzle, and no useful impulse is obtained from this part of the expansion.

When the plasma expansion ceases, the deformed and compressed magnetic field springs back towards its initial configuration, in the process, expelling the remains of the cloud. During both the compression and expansion phases of magnetic field distortion, a very significant force is transferred to the vehicle via the nozzle coils.

Electrical energy required to power the next pulse; i.e., to power the plasma guns and to create the initial magnetic field, is extracted by tapping off some of the current that is induced in the coils during the plasma cloud expansion. The energy required for each plasma gun is stored in a capacitor that is attached to the gun itself. The energy required to reestablish the magnetic field, prior to the next fusion pulse, is stored in a superconducting magnetic energy storage (SMES) device.

2.3.2 Magnetoplasmadynamic Thruster

The MPD thruster is a member of the electromagnetic class of electric propulsion systems. These thrusters use electromagnetic forces to accelerate plasma propellant to speeds in excess of 50 km/s. With I_{sp} values reaching 5,000 s and thrust levels of up to 2 N, the MPD thruster has a very competitive performance when compared to other electric propulsion systems.

An MPD thruster makes use of coaxially arranged electrodes consisting of a center spike cathode and an outer annular anode. An inert gas, such as xenon, enters through a rear injector plate and flows between the two electrodes. An electric potential that is large enough to ionize the gas is applied across the electrodes. Once ionized, the gas becomes electrically conductive and a current flows from the anode, through the gas, and to the cathode. This current, along with the electrode geometry, produces an induced circular magnetic field between the electrodes. The resulting Lorentz force caused by the interaction of the current and the magnetic field accelerates the ionized gas or plasma in a direction perpendicular to both the electric and magnetic fields. Thrust is imparted to the device by the reaction against this force.

The arc discharge between the two electrodes produces a large amount of heat that raises the temperature of the thruster. Most of this heat must be removed by a cooling system in order to protect the materials. Some MPD thrusters are designed to use this heat to produce additional thrust by thermodynamic expansion. Other MPD thrusters are augmented by including an external magnetic coil wrapped around the thruster. This coil increases the field strength of the induced circular magnetic field between the electrodes and can improve performance. Figure 8 shows the cross section of an MPD thruster.

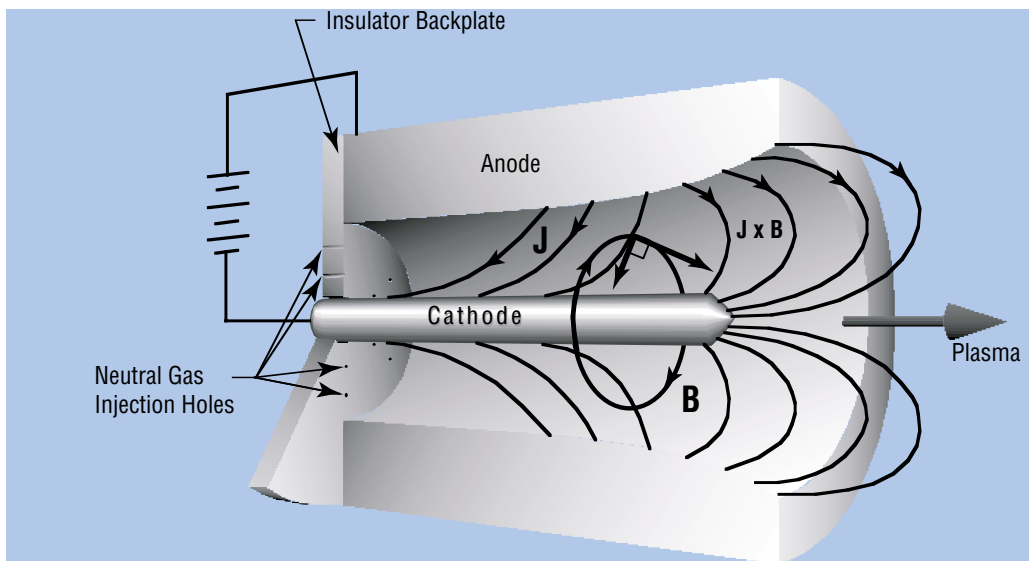


Figure 8. MPD thruster cross section (courtesy of Jet Propulsion Laboratory).

Advances in MPD performance are being pursued by using higher power systems and by using hydrogen gas as the propellant. Because hydrogen has a low molecular weight, it can exhaust at a higher velocity and deliver higher I_{sp} . It is speculated that I_{sp} values as high as 10,000 s may be achievable, but that remains to be seen. Although most MPD thrusters tested to date operate at hundreds of kilowatts of electrical power, it may be possible to push their power levels as high as the megawatt range. The efficiency of these thrusters varies between 30 and 50 percent of the input power being converted to jet power.

The performance limitations of the MPD thruster are due to plasma physics processes that take place within the electrical discharge. For an MPD thruster, most of the performance losses are due

to the thermal energy created by the high current passing through the plasma. The plasma has an electrical resistance based on the level of ionization, which is in turn determined by the voltage change between the electrodes. The higher the voltage change, the more current passes through the plasma, the stronger the induced magnetic field, and the more thrust produced. As a matter of detail, performance is limited by the geometry of the electrodes, the electrical properties of the propellant, and the magnetic Reynolds number.

In order for the propellant to be ionized, a sufficiently strong electric field must be applied. The degree of ionization is essentially a function of the density of the gas and its ionization potential, the voltage potential across the electrodes, and the distance between the electrodes. These relations govern the mass flow rate, power, and size combinations that are available to a thruster. The magnetic Reynolds number limits the I_{sp} of the thruster. This is a nondimensional number that represents the ratio of the convective properties of a magnetic field in moving plasma with the ability of a magnetic field to diffuse through the plasma. For plasma moving through a stationary magnetic field, a magnetic Reynolds number <1 indicates that the plasma can move freely through the magnetic field. The limit of this case is when the magnetic Reynolds number equals unity. In this case, the speed of the moving plasma and the rate at which the magnetic field can diffuse through the plasma are equal. If the magnetic Reynolds number becomes greater than unity, the magnetic field is dragged along with the moving plasma and produces a drag force on the plasma flow, which will result in a loss of performance and may lead to instabilities within the plasma that can further reduce performance and thruster life.

The life-limiting parts of the thruster are the electrodes. High currents cause the electrode material to sputter, which will eventually reduce performance to an unacceptable level. The lowest erosion rate achievable with current models is 0.5 ng/A/s, or a sputtering of one atom for every 5×10^6 ions collected on the electrodes. This limits the integrated impulse to $\approx 10^6$ N-s.

2.3.3 Liquid-Metal Rankine Power Conversion System

For the HOPE/RASC studies, a potassium LMR system was selected for the power conversion module, for both the solid-pin, lithium-cooled reactor and the MSR concepts.

Potassium Rankine systems are actually quite well characterized since all of the major components; i.e., turbine, condenser, alternator, and heat exchangers, have undergone many hours of extensive ground testing. One advantage of Rankine systems is that the heat is typically rejected at much higher temperatures, ≈ 900 K versus 425 K for a Brayton cycle. Thus, the radiator mass tends to be much smaller for Rankine systems. This approximate doubling of the heat rejection temperature allows the radiator mass to be reduced approximately by a factor of 16 ($2^4=16$):

$$Q = \sigma A (T_{rej}^4 - T_o^4) . \quad (1)$$

A picture of an LMR conversion system is shown in figure 9.

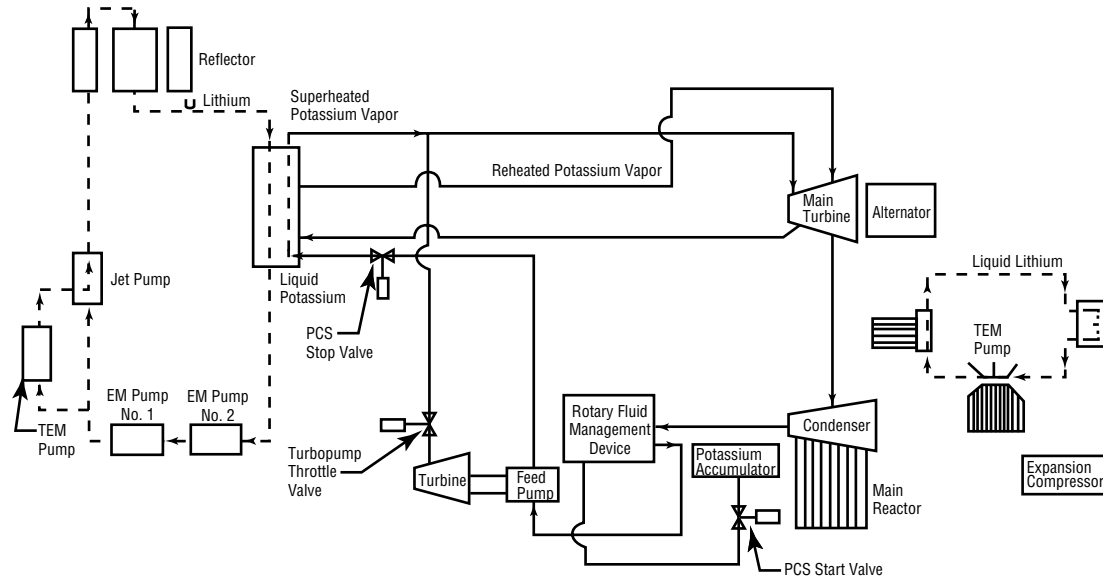


Figure 9. LMR conversion system.⁶

A typical space system layout is shown in figure 10.

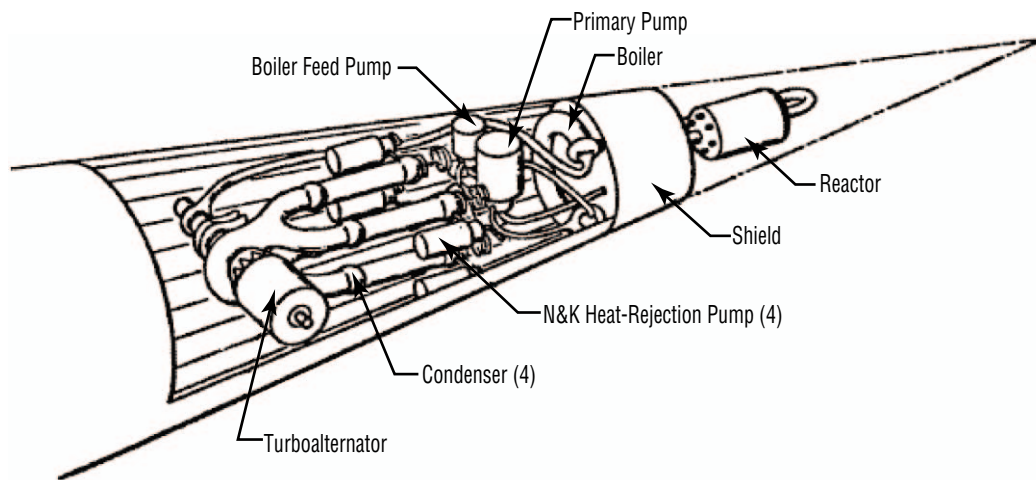


Figure 10. LMR system NEP vehicle layout.⁷

The potassium LMR cycle is similar to the typical steam cycle employed by the commercial utility industry except that potassium is used as the working fluid.

The following discussion is taken directly from the ALKSYS users manual, *ORNL—TM-10427*.⁸

“In the power conversion system, the principal flow of dry, saturated potassium vapor leaving the boiler of the lithium-cooled reactor is diverted to the turbine of the turbo feed pump. As the vapor expands through the main turbine, inter-stage and external separators are used to maintain the liquid content of the stream at <12% to avoid the potential for erosion of the turbine blades. Upon exhausting from the turbine, the vapor is condensed in tapered annular spaces surrounding the evaporator sections of the radiator heat pipes. Condensate is drawn from the small ends of the condensing annuli by a jet pump that is driven by a small stream of liquid taken from the discharge of the turbine driven feed pump. Liquid discharging from the jet pump flows to the intake of the feed pump and is then pumped through the shell sides of a specified number of feed heaters (0–3) back to the boiler. One of the heaters is heated by feed pump turbine exhaust; other heaters, if more than one are specified, are heated by vapor extracted from appropriate stages in the main turbine or taken from the boiler outlet line if necessary, to provide the specified boiler feed temperature.”

Turbine blade tip velocity is a parameter that is dependent on the strength of the turbine rotor material and is treated as an input variable in the model to allow evaluation of the effects of advanced rotor materials. This parameter has a strong effect on turbine size and rotational speed and, therefore, on the mass of the turbine and the generator.

Most of the required input information for the ALKSYS code operation pertains to the power conversion submodel. Input includes turbine inlet and outlet temperatures, dry-stage efficiency for the turbine, and the number of stages of feed heating.

The code outputs a complete mass and energy balance for the power conversion subsystem as well as mass estimates for the major components.

The major heat rejection load from the power system is from the power turbine condenser. The heat is rejected by a heat pipe radiator operating at a temperature somewhat lower than that of the condenser. A smaller heat rejection load from cooling of the reactor shield and the turbine generator is rejected by a low-temperature heat-pipe radiator.

The geometry of the radiators depends on the power system rating. Input requirements for the heat rejection submodel include launch vehicle bay dimensions and the operating temperature of the low-temperature radiator. Thermal loads for both parts of the radiator are provided by the power conversion submodel, which provides dimensional information and the estimated mass of the heat rejection system.

The SCR design is based on a fast-spectrum, metallic-clad rod fuel element containing uranium nitride (UN) pellets. The primary coolant is lithium; hence, it is similar to the SP-100 genre. The ALKSYS code limits the peak pellet burnup to 10 percent and the peak heat flux to 80 W/cm². Rod diameter is determined by heat flux and burnup, but it is limited to 0.64 cm for mechanical stability. Reactor control is provided by in-core assemblies and by drums that can be rotated and are located around the core periphery. ASTAR-811C is used for the fuel-rod cladding and structural components operating at temperatures >1,100 K, and Nb-1%Zr is used at lower temperatures. The design stress is two-thirds of that, which produces 1 percent creep during the system lifetime.

Two options are available in the ALKSYS code for estimating shield size and mass. In the 2π option, the shield configuration and dimensions are selected to provide a fast neutron fluence of 10^{13} neutrons/cm² and a total gamma dose of 10^6 rad at a plane that is 15 m from and perpendicular to the axis of the cylindrical reactor vessel. The shield is thickest along the axis that faces the payload, but it also covers the sides of the reactor to reduce scattered radiation. The 2π shield utilizes layers of lithium hydride in a honeycomb matrix and tungsten. The second option utilizes an alternative shield configuration consisting of a thin layer of lithium hydride on all exposed surfaces of the reactor and a shadow shield of lithium hydride and tungsten that faces the payload. The shadow shield is used to provide a prescribed fluence of fast neutrons and gamma dose at a payload dose plane with given diameter and distance from the reactor.

The ALKSYS code was used to estimate masses of the various subsystems of the vehicle. The lithium-cooled UN reactor option was selected to provide mass estimates of the reactor and shield. The shadow shield configuration was selected with the same radiation requirements as imposed for the 2π option as discussed above.

2.3.4 Magnetohydrodynamic Power Conversion System

Conventional electrical generation systems use a turbogenerator to extract power from a hot working fluid. Having cooled during this process, the working fluid passes on to a radiator system, where waste heat is rejected. The radiator is usually the most massive element of the system because its mass is dictated not only by the heat rejection rate but also by the temperature at which the waste heat must be rejected. A low rejection temperature demands a massive radiator. The strong dependence of radiator mass on rejection temperature (T) can be gauged from the Stefan-Boltzmann equation:

$$\text{Radiated power/unit surface area} = \sigma T^4, \quad (2)$$

where σ is the Stefan-Boltzmann constant.

By increasing the heat rejection temperature of the system, the radiated power per unit radiator area can be significantly increased (with the fourth power of temperature), permitting the radiator to be drastically reduced in both area and mass. Unfortunately, to maintain the same level of power extraction, this necessitates also increasing the working fluid temperature at the turbine inlet. With a suitable power source design, in this case a nuclear fission reactor, higher working fluid temperatures appear possible. However, there are severe technology limits imposed by the turbine itself that place an upper limit on cycle temperatures and hence dictate a high radiator mass.

MHD technology provides a means of extracting electrical power directly from the working fluid without the need for a turbine system. A perpendicular magnetic field is imposed on an electrically conducting working fluid moving through a channel. In general, this produces a Faraday current, \mathbf{J}_F , and a Hall current, \mathbf{J}_H . The Faraday current is produced as a result of the interaction between the moving conductor; i.e., the working fluid, and the magnetic field:

$$\mathbf{J}_F = \sigma \left(\frac{1}{c} \mathbf{U} \times \mathbf{B} \right), \quad (3)$$

where \mathbf{U} is the fluid velocity, \mathbf{B} is the applied magnetic field, σ is the working fluid conductivity, and c is the vacuum speed of light. The Hall current is produced by the interaction between the Faraday current and the magnetic field:

$$\mathbf{J}_H = \sigma \left(\frac{M}{\rho e c} \mathbf{J}_F \times \mathbf{B} \right), \quad (4)$$

where M is the ion mass, ρ is the plasma mass density, and e is the ion charge.

Depending on which of the two is larger, the device will use either the Faraday or Hall current for power generation. The selected current is connected to an external load through contact electrodes on the sides of the channel.

Unlike a turbine-based system, which requires rotating machinery placed in the central, and hottest, portion of the fluid flow, the MHD system does not require any moving parts nor does it require any hardware that intrudes into the hottest part of the working fluid. As a consequence, by utilizing suitable cooling techniques, the hardware temperature can be decoupled from the hottest portion of the working fluid. This offers the possibility of achieving significant increases in fluid temperature, compared with turbine-based systems, with consequently higher radiator temperature and reduced mass.

The MHD system proposed here is shown in figure 11. Note that for the purposes of this study, a gaseous Brayton cycle, sometimes known as a Joule cycle, is postulated. Although higher performance could be obtained by employing a gas-to-liquid Rankine cycle, the condensing vapor tends to be highly corrosive for most viable working fluids.

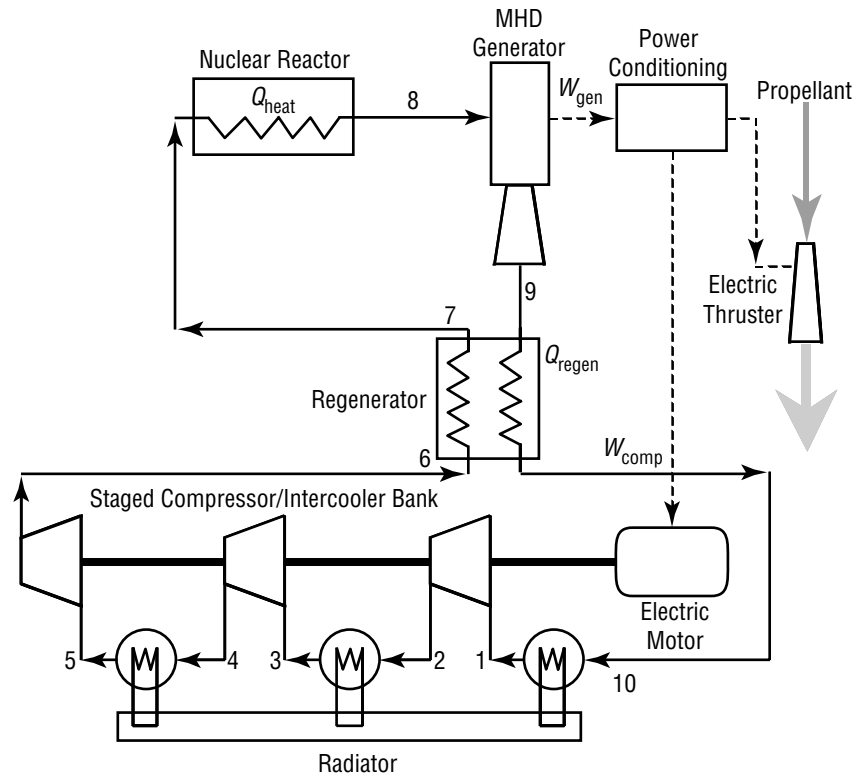


Figure 11. Schematic for MHD power and propulsion system.

As illustrated in figure 11, the MHD system consists of the following elements:

- The power source—in this case, a nuclear fission reactor.
- The MHD generator.
- A thermal regenerator—permits a measure of heat exchange between the relatively hot generator exhaust fluid and the relatively cool power source (reactor) inlet fluid.
- A set of compressors—required for circulation of the working fluid.
- Thermal radiators—disposal of waste heat.
- A power conditioning system—converts the generator output power into the required propulsion system input power.
- Electric motor(s)—powers the compressors.

Two different design configurations are available for the MHD generator. If the Faraday current is larger than the Hall current, the linear configuration is used. If the Hall current is larger, then the radial-

flow configuration is employed. In the linear configuration, the working fluid flows along a channel of rectangular cross section. The electrodes, which provide the conductive link between the fluid and the generator, are installed along two opposing walls of the duct. In order to maximize the useful Faraday current, it is necessary to take steps to minimize the Hall current, which is proportional to the Faraday current times the applied magnetic field. The practical method of accomplishing this is to segment the electrodes, thus, inhibiting the flow of Hall current along the channel. Unfortunately, this introduces significant additional complexity into the fabrication process.

In the radial-flow design, which is employed if the Hall current dominates, the flow channel consists of the space between two circular disks located one on top of the other. The working fluid is injected into the space through the center of one of the disks. It then flows outwards between the two disks in a radial manner. Unlike the rectangular duct configuration, the radial one has only two confining surfaces and the flow geometry ensures that the Faraday current just flows in a rotational sense while the Hall current flows in a radial manner.

2.3.5 Solid Core Fission Reactor

The temperatures required to obtain sufficient ionization for a conventional MHD generator are in the 2,500 to 3,000 K range. Based on *NASA/TP—2001–211274*,⁹ the required reactor outlet temperature was selected to be 2,500 K. This necessitates the use of advanced high-temperature uranium carbide (UC) or uranium-tungsten (Cermet) fuels.

Since an ALKSYS-type systems level code does not exist for a high-temperature, gas-cooled SCR, MSFC used the same reactor and shield mass numbers provided by GRC for its 2,000 K direct Brayton cycle gas-cooled reactor.

2.3.6 Molten Salt Reactor

One of the major driving factors for high-power reactor development will be the economic cost. Researchers at MSFC began looking at previous reactor studies to see if any concepts had been overlooked for possible use in multimegawatt (MMW)(e) space propulsion systems. One such concept is the MSR.

MSRs were originally conceived as response to the Aircraft Nuclear Program (ANP) of the late 1950s and early 1960s. The requirements of the program; i.e., a lightweight, reliable, high-temperature reactor, are very similar to the requirements for in-space NEP and planetary surface power. These missions also require reactors that are lightweight, operationally robust, and scalable in power for widely varying scientific mission objectives.

The ANP design effort led to the development of a homogeneous fluid fuel consisting of uranium tetrafluoride (UF_4) dissolved in an NaF-ZrF_4 fluoride salt. The first successful demonstration of molten salt fuel was the Aircraft Reactor Experiment, a 2 MW-thermal (MW_{th}) research reactor that operated for 96 MW-hr. Several different types of salts were developed as part of the ANP and the MSR Experiment (MSRE) project. The MSRE was an 8 MW research reactor project to demonstrate the viability of molten salt technology. It operated for >13,000 full-power hr.

MSRs have several advantages over conventional solid-pin reactors for in-space power missions. The fluoride salt serves the multiple roles of fuel, moderator, and coolant. Fluoride salts are resistant to radiation damage and they do not undergo radiolytic decomposition. The salts demonstrate excellent solubility of uranium and thorium, and they have very low vapor pressure at operating temperatures.

There are several specific advantages for space nuclear systems. One is the capability of the fuel to operate at very high power densities. The dimensions of a reactor are determined by criticality and heat transfer limitations. The ability to effectively remove heat from the reactor is generally the more restrictive criterion on the minimum size, especially at higher power levels. To the first order, the size of a reactor is determined by the maximum power density (MW/m^3) of the fuel. In conventional solid-pin reactors, limitations on heat generation rates are required to prevent exceeding fuel pin centerline temperatures. Ceramic oxide fuels, with their low thermal conductivity values, can be especially limiting in this regard. MSRs, however, eliminate the often large temperature rise across the fuel cladding, fuel pin to cladding gap, and the fuel pin itself. The thermal conductivity and viscosity of the fluoride salts are similar to those values for water. Table 1 lists some important parameters for various MMW space reactor types. The values listed in the table are not all-inclusive, but are taken from the open literature to represent typical values.¹⁰ The power density of an MSR can be anywhere from 5 to 20 times higher than traditional solid-pin-type reactors.

Table 1. Comparison of MMW space reactor types.

Reactor Type	Coolant Pressure (Pa)	Q_{vol} (MW/m^3)	$T_{\text{coreoutlet}}$ (K)	Typical Fuel
HTGR	2.76×10^6	57.7	1,367	UO_2 -refractory clad
PBR	2.89×10^6	40.5	1,600	UC particles
LMR	1.14×10^5	75.9	1,550	UN-W/25 Re
MSR	<10	6.6–2,500	1,000–1,300	$\text{LiF-BeF}_2\text{-UF}_4$

An important property for space reactors is the ability to scale well with respect to mass for higher power levels. The reactor shield is often one of the largest contributors to the overall system mass of an MMW(e) NEP system. The size of the shield is directly proportional to the volume of the reactor. High-power density reactors tend to be very compact in size; hence, the shield size and mass are much smaller. Again, the high-power densities of MSRs are an important advantage in this respect.

To obtain conservative estimates of the mass of an MSR reactor for the RASC studies, the reactor and shield masses from the output of the ALKSYS code were used with the code input options of (1) a lithium-cooled UN pin reactor option and (2) a shadow shield with the same radiation requirements as a 2π shield. These masses were used as an initial first-order estimate. As mentioned above, the higher power densities of an MSR should allow for a reduction in the reactor size and shield size and mass. Ongoing studies are being performed on detailed MSR designs that can provide specific mass estimates.

One of the more interesting observations of the analyses performed using the ALKSYS code is that the largest contributor to the reactor/power conversion alpha is the radiator mass, as it is typically 50 percent of the total mass. Therefore, reductions in radiator specific mass will have a much larger effect

on the power system alpha than the reactor type. For in-space propulsion systems where a low alpha is an absolute necessity, it makes much more sense to choose an economical, easily designed, and testable reactor system and then couple it with a power cycle capable of rejecting heat at a high temperature, such as the LMR system.

2.4 Vehicle Subsystem Design

2.4.1 Payloads

The payload components of the HOPE vehicle consist of a Transhab module, a surface habitat, a lander, and an in situ resource utilization (ISRU) plant. These components are responsible for providing a habitable environment on the vehicle and on the surface of Callisto as well as supporting the exploration team as it collects scientific data. The Transhab forms the main living quarters for the six crewmembers. This module has a mass of ≈ 40 t and contains an additional 4 t of consumables. An example of the Transhab concept is shown in figure 12.

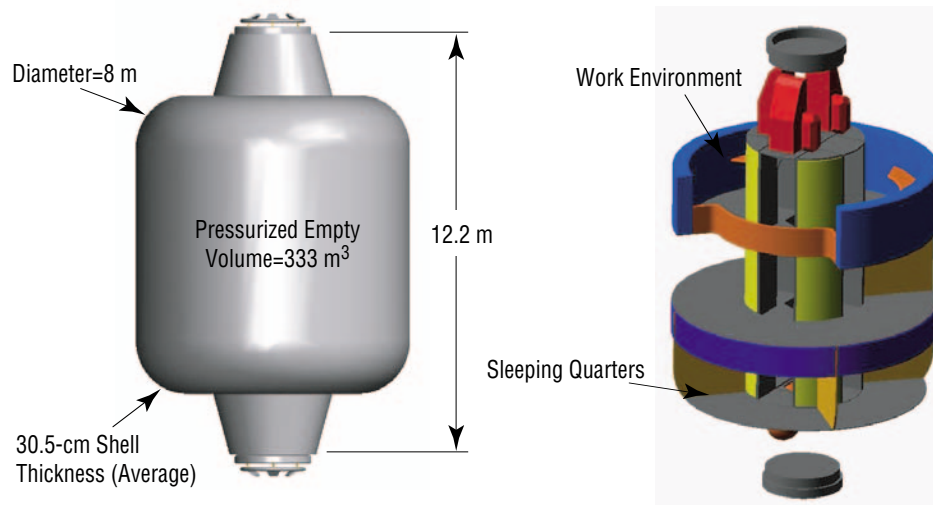


Figure 12. Transhab configuration and layout (S. Krizan et al., personal communications, March 2002–April 2003).

The surface habitat is an inflatable structure that can house three crewmembers on the surface of Callisto. It is responsible for providing shelter to the surface crew and serves as a laboratory from which surface experiments are conducted. A 250-kW electric (1 MW_{th}) reactor, located 1 km away, will generate power for transmission to the surface habitat. Figure 13 depicts the conceptual design of the surface habitat.

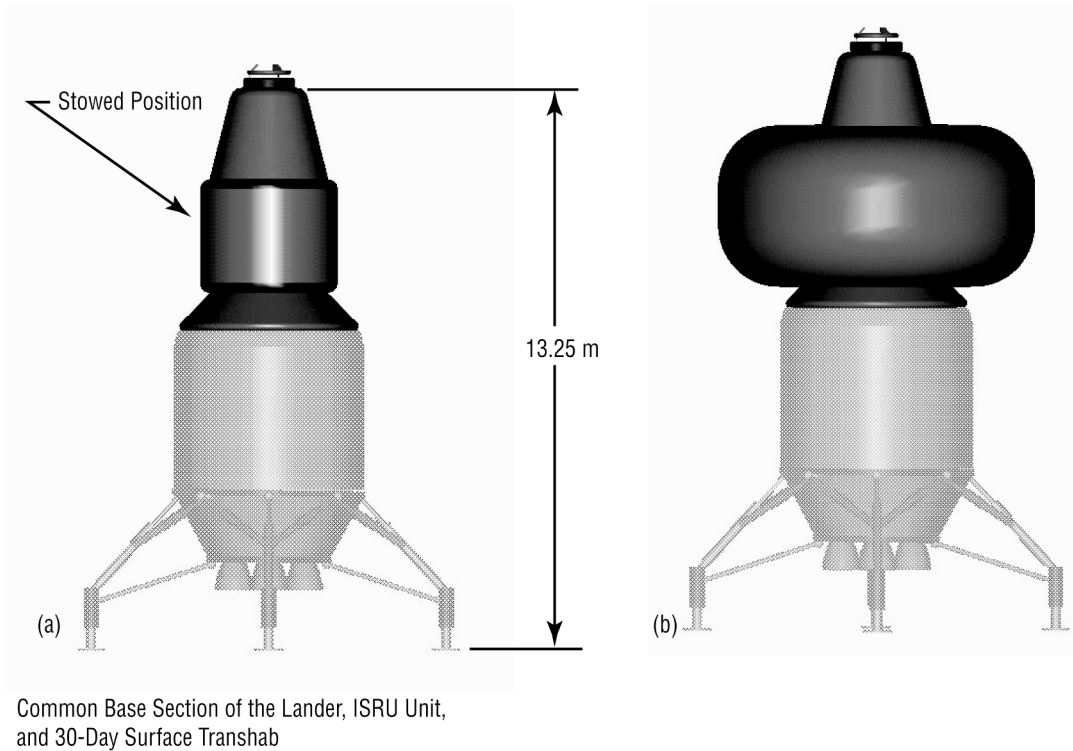


Figure 13. Configuration of the surface habitat in (a) the stowed position and (b) the inflated position. Living area uses inflation technology similar to Transhab (S. Krizan et al., personal communications, March 2002–April 2003).

The lander is used to transport crew and materials between the surface of Callisto and the orbiter. It is capable of carrying up to 40 t down to the surface. Its fuel is produced from resources present on the surface of Callisto. The lander is shown in figure 14.

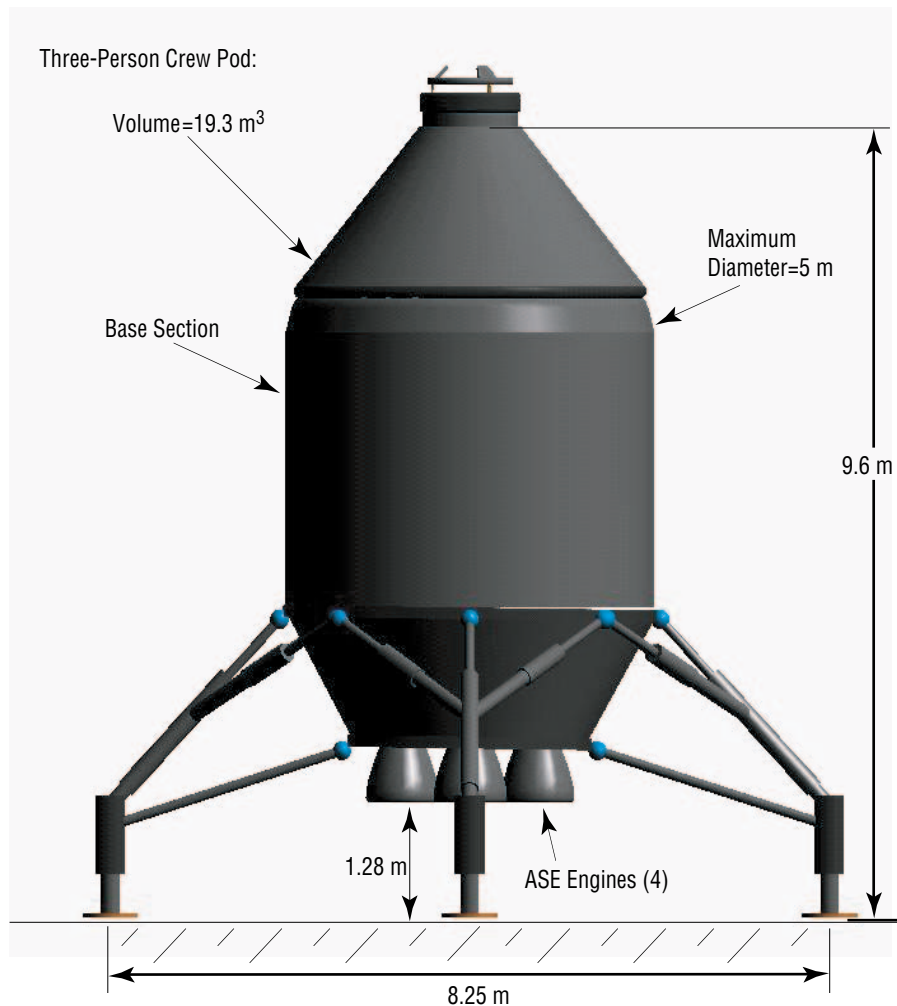


Figure 14. Configuration of the crewed lander (S. Krizan et al., personal communications, March 2002–April 2003).

Callisto is a desolate, minor planet with more impact craters than any other object in the solar system. Its crust dates back 4 billion years, which was around the time that the solar system was formed. This ancient surface may be able to provide valuable information about the state of the early solar system. In addition to scientific information, Callisto will also be able to provide mission resources; e.g., propellant for the mission lander.

Callisto has a density of 1.86 gm/cm^3 , and is comprised of ice and rock. The 200-km-thick crust is an icy layer that could be mined for water. There is believed to be a 10-km-deep ocean of salt and water beneath the crust. Because Callisto contains such an abundance of water, it can provide a variety of resources. Through simple distillation and dissociation processes, oxygen and hydrogen can be produced for fuel and air. The ISRU unit will convert the icy regolith of Callisto into water, liquid oxygen (lox), and liquid hydrogen (LH_2) at a rate equivalent to 21 kg/hr (of water). This will provide enough propellant for the lander to rendezvous with the orbiter every 30 days. The ISRU will require a power of 215 kW. Figure 15 illustrates the ISRU concept used in this study.

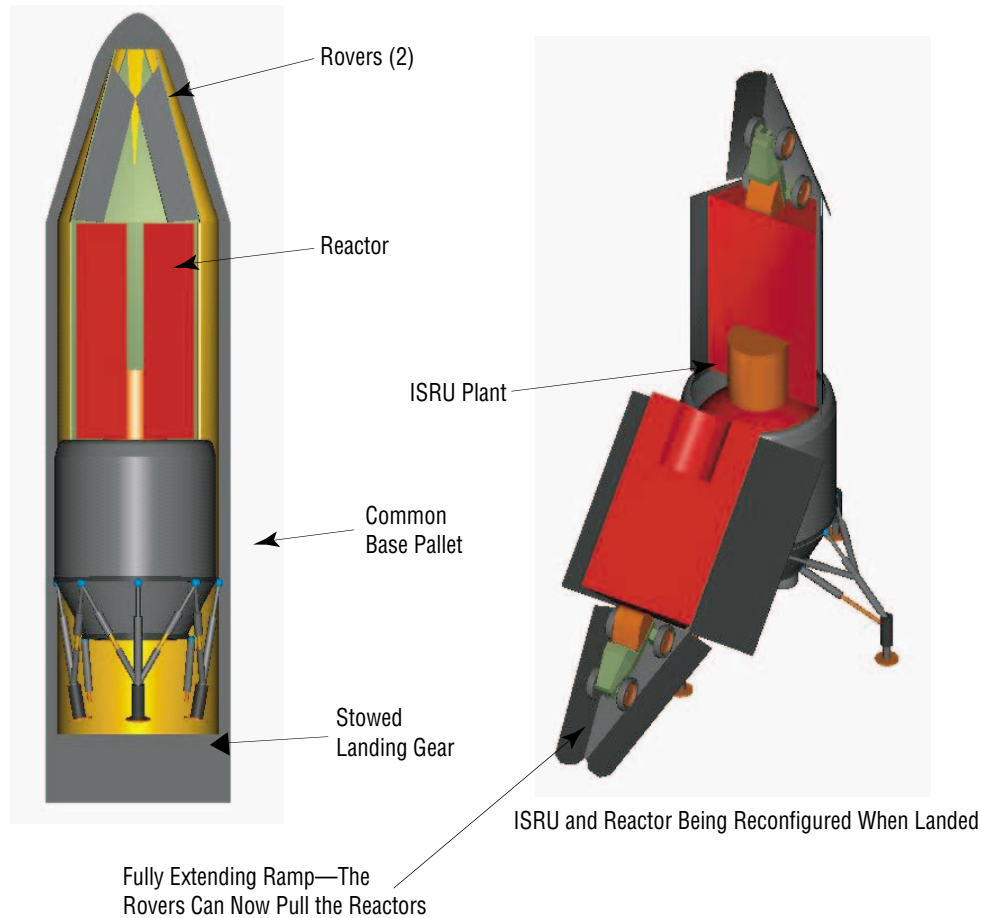


Figure 15. ISRU configuration and deployment. Reactors must be positioned away from the ISRU before commencement of operations (S. Krizan et al., personal communications, March 2002–April 2003).

One of the ground rules of the HOPE study is that all of the above systems, as well as any other payload launched from Earth, would fit inside an assumed launch vehicle fairing similar to that of a Delta IV Heavy. The dimensions of this fairing can be seen in figure 16. All of the vehicles described in this study can be broken down into their respective parts and launched within this fairing. Note that the fairing determined the size and shape of our propellant tanks. Some components, such as the MTF assembly, would require significant on-orbit assembly after launching.

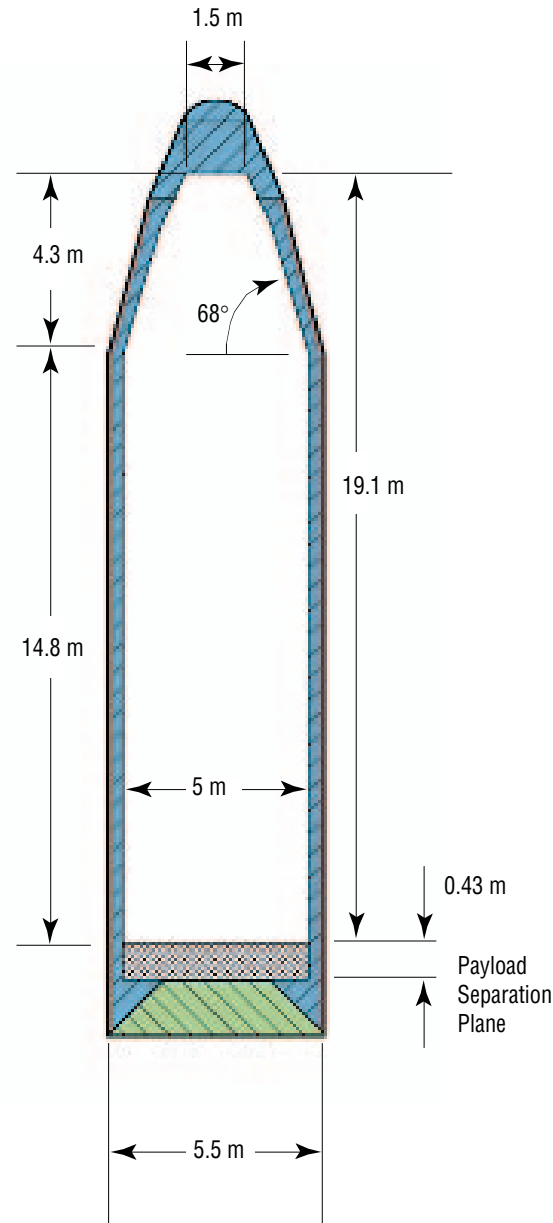


Figure 16. Dimensions and configuration of expendable launch vehicle fairing assumed for this study (S. Krizan et al., personal communications, March 2002–April 2003).

2.4.2 Reaction Control System

The reaction control system (RCS) is based on an oxygen and hydrogen chemical propulsion system. Twenty-four 500-lbf thrusters are located in two ring frames on the vehicles structure and provide full six-degrees-of-freedom maneuvering capability for attitude, docking, and spin control for artificial gravity. During the outbound and inbound portions of the flight, the manned vehicle is spun at ≈ 1.25 rpm to simulate 25 percent of Earth's gravity. To accomplish both of these tasks, up to 85,000 lb of lox and LH_2 propellant are stored separately from the main drive propellant. These propellants are

maintained in a liquid state by the liberal application of multilayer insulation with any additional heat leakage into the system removed by cryocoolers powered by the main electrical system. To ensure that the propellants are at the proper gaseous temperature and pressures required by the RCS thrusters, a series of run tanks use electrical resistance heaters to convert the cryogenically stored liquid propellants into the gaseous propellants required for the RCS thrusters. These run tanks are sized to hold ≈ 1 m/s ΔV of gaseous propellant, which is available on demand to the RCS thruster. If additional propellant is required beyond the 1 m/s stored in the run tanks, the run tanks become a conditioning plenum, converting liquid cryogenic propellant into gaseous propellant during high-demand attitude control and artificial-gravity spin maneuvers. In addition to the main RCS thrusters are a series of smaller 50-lbf hydrogen cold gas thrusters, which are used as needed for fine pointing and close proximity operations.

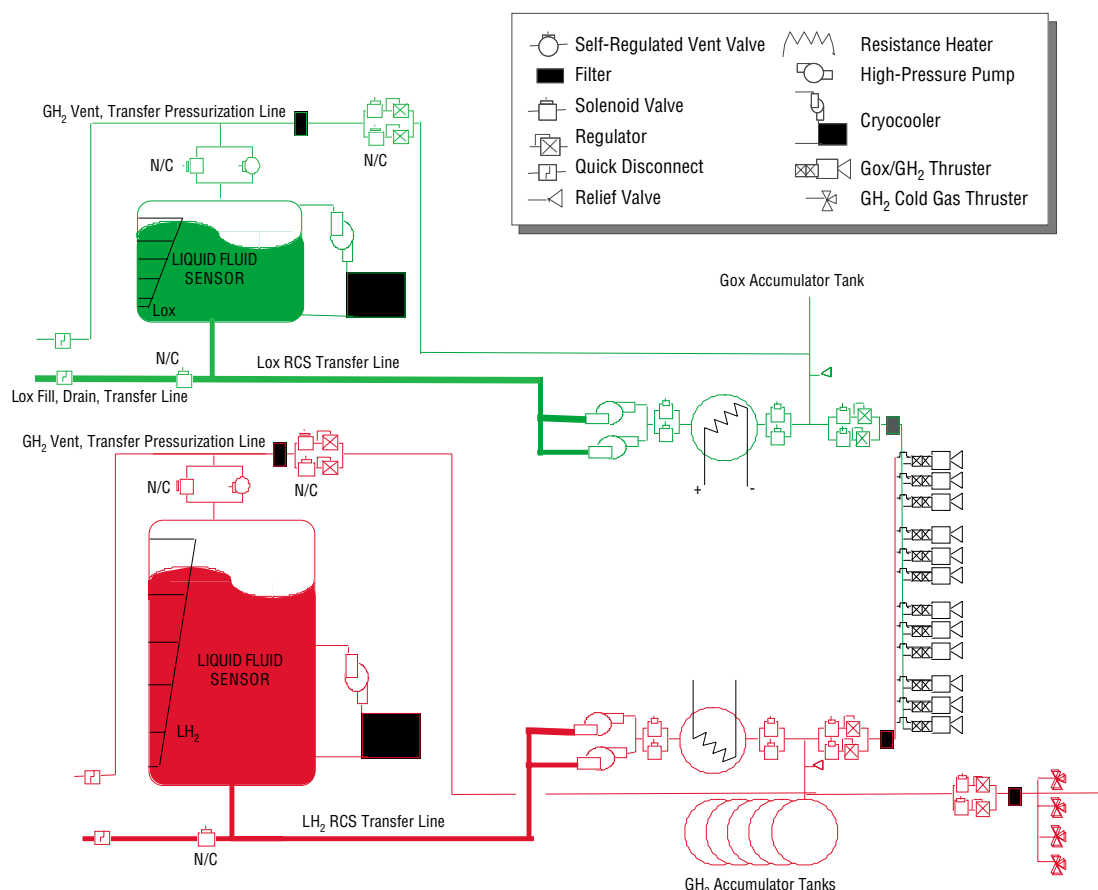


Figure 17. Gaseous oxygen/gaseous hydrogen RCS with liquid propellant storage.

2.4.3 Structures

The main propellant tanks for this study were designed by the Launch Vehicle Analysis (LVA) computer tool.¹¹ The analysis was based on the assumption that the tanks were launched fully loaded with hydrogen. The tanks were not assumed to be pressure stabilized and no shroud was required. LVA analyzed the tanks using a full gamut of prelaunch, lift-off, and flight loads. The tanks have both fore and aft skirts that remain with them throughout the mission. The necessary docking equipment is launched within the skirts.

The main truss design was based on earlier manned Mars studies. With an on-orbit assembled truss, the designing loads are not the propulsion system thrust as is commonly thought. Most of the mass results from loads imparted during the Earth-to-orbit (ETO) phase. Assembly and overall stiffness requirements are additional factors; therefore, truss sections can serve different space missions with little or no change.

2.4.4 Thermal

There are three heat rejection systems for the HOPE vehicle: (1) A low-temperature radiator system for the avionics and crew, (2) a medium-temperature radiator for the power conversion system, and (3) a high-temperature radiator for the propulsion system waste heat. These radiators are necessary due to the need to maintain the systems within required temperature limits, and the fact that in space, the only method of dumping waste heat is through radiative heat transfer. All the radiator systems use heat pipes to distribute the heat evenly across the panels. Figure 18 is a simplified schematic of the thermal control system for the power conversion system and the MTF engine.

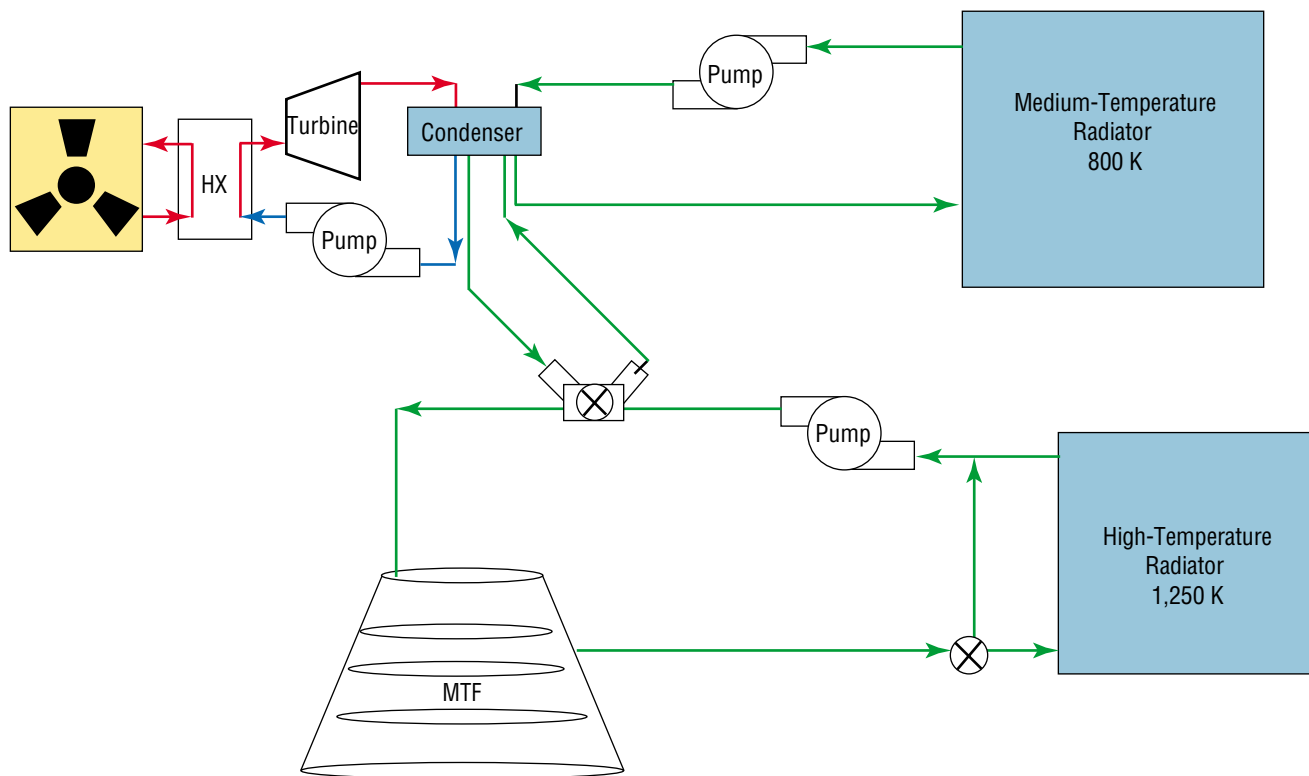


Figure 18. Schematic of power conversion and engine thermal control systems.

Thermal radiators for spacecraft systems need to be as lightweight as possible. However, some of the vehicle system requirements force the thermal radiator system to be heavier than would be necessary, provided that there is no other required functionality. The thermal radiator panels for advanced space vehicles of the type described in this TP tend to have large surface areas, requiring that they be deployed prior to usage, and deployment mechanisms add weight to the panel. Also, reliability and safety

requirements will likely add weight to the system. Many have attempted to analytically model these panels with various heat transport mechanisms and materials technology to determine the weight of the system. Near-term technology incorporates composite panels with heat pipes that are imbedded within the panels.

Eventually, for the system analysts, the input to model the radiator simplifies to a unit area or areal density. For advanced vehicles, some analysts have estimated this unit weight to be as low as 1 kg/m² and as high as 20 kg/m². Of course, technology assumptions for the study affect this number. A more advanced technology assumption implies a lower unit weight. For HOPE, the design team assumed near- to mid-term technology, which led to the assumption that the high-temperature radiator panels, with the deployment mechanisms and safety and reliability requirements, have a unit mass of 10 kg/m² for single-sided or 5 kg/m² for two-sided panels, while the medium-temperature panels were assumed to weigh 8 kg/m² for single-sided or 4 kg/m² for two-sided panels. The low-temperature radiator panels have an assumed unit mass of 3.7 kg/m² for two-sided panels. For comparison, the *International Space Station's* two-sided radiator panels weigh 8.5 kg/m².

Analyses performed to size the radiator panels assumed that the panels have a perfect view to space with no view of the Sun. The infrared emissivity (ϵ) was assumed to be 0.9. Fin effectiveness was ignored, and the panel was assumed to be at a constant average temperature. The Stefan-Boltzmann equation is used to calculate the radiator surface area. A radiator temperature was assumed, and based on the heat rejection requirements, a surface area was calculated by using

$$q = \epsilon \sigma A_s T_s^4 . \quad (5)$$

The medium-temperature radiator panels reject heat from the power conversion system at 800 K. The panels employ a combination of water and sodium-potassium heat pipes. The higher temperature NaK heat pipes are at the radiator's cooling fluid inlet with the water heat pipes near the cooler end. Figure 18 shows the radiator panel concept.

The heat rejection requirements vary with the concepts analyzed, and panel surface areas and masses vary accordingly. The requirements are summarized in table 2.

Table 2. Medium-temperature radiator analysis results summary.

Medium-Temperature Radiator			
Concept	D-D MTF 30-Day Stay	D-D MTF 180-Day Stay	D-He3 180-Day Stay
Heat rejection requirement (MW)	24.1	45.8	33.9
Heat rejection temperature (K)	800	800	800
Radiator total surface area (m ²)	1,156.6	2,192.3	1,622.7
Radiator mass (kg)	4,614.5	10,961.5	6,490.9

The high-temperature radiator panels reject the heat from the propulsion system. These panels use heat pipes with lithium as a working fluid. The temperature of these panels is assumed to be 1,250 K. The

heat is collected in the propulsion system using a high-temperature molten salt, FLiBe. The FLiBe passes through a heat exchanger to which the evaporator ends of the heat pipes are connected where the FLiBe is cooled. The cooled fluid flows back into the engine, completing the thermal control circuit. As with the medium-temperature radiator, the heat rejection requirements vary with the vehicle concepts and are summarized in table 3.

Table 3. High-temperature radiator analysis results summary.

High-Temperature Radiator			
Concept	D-D MTF 30-Day Stay	D-D MTF 180-Day Stay	D-He3 180-Day Stay
Heat rejection requirement (MW)	261.9	497.9	176.5
Heat rejection temperature (K)	1,250	1,250	1,250
Radiator total surface area (m ²)	2,103.3	3,998.6	1,417.5
Radiator mass (kg)	10,516.5	19,993	7,087.3

Cryogenic refrigeration systems are used to maintain the LH₂ propellants during the transit to Callisto. Cryogenic hydrogen has a boiling point of ≈ 20 K, so any heat leaking into the tank affects the mission through propellant boiloff. For long-term missions, passive insulation systems are massive, accounting for the propellant boiloff during the mission. Zero boiloff (ZBO) systems use a combination of active and passive thermal control to provide a minimum mass solution. ZBO systems comprise subsystems that include the refrigerator, power system, controller, and thermal radiator to reject the waste heat from the system, and the insulation system that is composed of multilayer insulation and foam. The combination of the insulation and refrigeration system is optimized to attain the minimum system mass while taking into account the propellant selection.

The ZBO system, sized for the HOPE mission, uses present day cryocooler technology assuming two-stage coolers for the LH₂ tanks. The mass and power calculations were based on research and analyses performed by NASA's GRC, MSFC, and Ames Research Center. The analysis methodology takes into account the mass of the propellant, the size and surface area of the propellant tanks, the number of propellant tanks, and the type of propellant, tank pressure, and environmental conditions. Using this methodology, a ZBO system can be adequately sized to maintain the required cryogenic propellant for the HOPE mission.

2.4.5 Auxiliary Power

All auxiliary power requirements on board the MTF vehicle are provided by an SP-100 lithium-cooled fast-spectrum nuclear reactor. The SP-100 reactor project was started in 1983 by Defense Advanced Research Projects Agency in cooperation with the Department of Energy. Its focus was to design and demonstrate technology to provide nuclear power at a wide range of power levels, from 100 kW to MMW, for space applications. It was designed to fit in the Space Shuttle payload bay and to operate for 7 to 10 yr. It has found application in the areas of nonterrestrial ground-based power, satellite/weapon systems power, and space vehicle power and propulsion.

For this study, a 375 kW electrical (2 MW_{th}) Rankine-cycle nuclear reactor with a net system efficiency of 19 percent was selected. A typical layout of this system is shown in figure 10. This three-loop system heats lithium metal in the primary cooling loop and then carries heat from the reactor to the boiler. Potassium metal is evaporated in the boiler and expanded through a 10-pole homopolar turboalternator to generate the electrical power (300 kW nominal). Waste heat is removed from the turboalternator exhaust by exchanging with the third loop, which carries a heated NaK metal mixture to the radiators. Electromagnetic pumps are used in all of the liquid-metal cooling loops.

To reduce the uniform radiation dose rate to 2 mrem/hr at a distance of 50 ft, a 4π shield is required. This shield utilizes layers of lithium hydride and tungsten metals as shown in figure 19. These layers effectively block the neutronic and gamma radiation that is produced by the reactor. This shield is extremely massive (table 4) and accounts for most of the weight associated with this system.

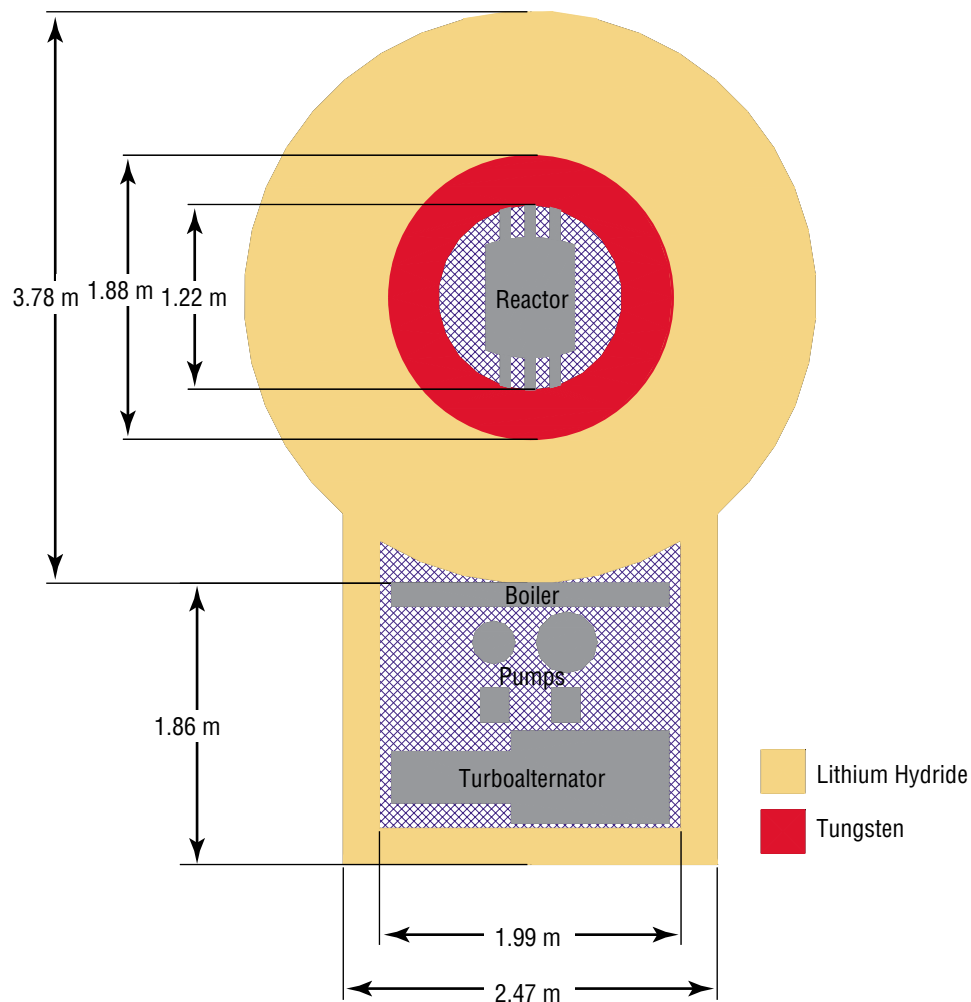


Figure 19. Reactor shield dimensions.

Table 4. Weight breakdown of the power system.¹²

	Weight			Weight	
	lb	kg		lb	kg
Reactor (2-MW thermal, 3.8 at% fuel burnup, 50,000-hr life) and reactor controls, drive, and structure	4,000	1,810			
Primary loop (Li):			Alternator coolant loop (K):		
Boiler	300	136	Radiator panel	320	145
Pump	700	317	Pump	130	59
Pipe and insulation	320	145	Expansion tank	50	23
Expansion tank	180	82	Piping	80	36
Lithium inventory (6.5 ft ³ (0.18 m ³) =160 lb (72.5 kg))	(a)	(a)	Potassium inventory	(a)	(a)
Total Weight	1,500	680	Total weight	580	263
Power conversion loop (K):			Turbine coolant loop (K):		
Turboalternator	1,300	590	Radiator	75	34
Condensers (4)	240	110	Pump	50	23
Boiler feed pump	300	136	Expansion tank	50	23
Condensate heat exchangers (2)	100	46	Piping	35	16
Separator	50	23	Potassium inventory	(a)	(a)
Potassium inventory control	100	46	Total weight	210	96
Potassium injection tank	250	114	Electronics cooling loop (DC-200):		
Potassium inventory	150	68	Radiator	275	124
Vapor piping	250	114	Pump	25	11
Liquid piping	50	23	Expansion tank	25	11
Total weight	2,800	1,270	Piping	105	48
Main heat-rejection loop (NaK):			Inventory	100	46
Radiator panels (4)	2,170	982	Total weight	530	240
Pumps (4)	480	217	Electrical equipment:		
Expansion tanks (4)	400	181	Speed control	100	46
Piping	430	195	Voltage regulator-exciter	200	92
NaK inventory	(a)	(a)	Internal power conditioning	200	92
Total weight	3,480	1,575	Parasitic load resistor	600	270
4 π shielding (50 m to payload at a dose rate of 2 mrem/hr)	142,000	64,000	Interconnecting cable	50	23
			Controls and instrumentation	50	23
			Total weight	1,200	546
			Structure (assumed to be 10% of engine weight)	1,962	890
Total estimated weight				158,262	71,370

(a) Included in weights above.

2.4.6 Trajectory Simulation

The computer program VARITOP was the primary tool used for trajectory analysis in the HOPE study.^{13,14} VARITOP is a low-thrust trajectory optimization program that was developed by the Jet Propulsion Laboratory (JPL) and first used in the 1970s. It is now widely used at JPL, GRC, and MSFC for preliminary mission design studies. Its sister program, SEPTOP, was used to provide trajectory support for the Deep Space 1 mission.

2.4.6.1 Heliocentric Analysis Method. VARITOP, a two-body Sun-centered analysis tool, is used for the heliocentric phase of the trajectory. The planets are assumed to be without mass, and targeting constraints match planetary positions and velocities relative to the Sun. Solution of the problem involves numerical integration of the state and costate or variational equations and the solution of a two-point boundary value problem to satisfy terminal constraints. The optimization, based on the calculus of variations, allows users to optimize many design variables. Departure date, flight time, and power required were some of the variables optimized in the HOPE mission analysis.

2.4.6.2 Planetocentric Analysis Method. VARITOP also offers several endpoint bias conditions that address the planetary departure and arrival phases of the trajectory. Of these, the most useful for this study is the low-thrust escape or capture spiral bias. For this option, it is assumed that the spacecraft departs from or is captured into a circular orbit around the planet using the low-thrust propulsion system. The formulation of the performance equations for these spiraling escape or capture maneuvers can be found in the paper, “Performance Computations With Pieced Solutions of Planetocentric and Heliocentric Trajectories for Low-Thrust Missions,” by Melbourne and Sauer.¹⁵

The current version of VARITOP, VARITOP 2000, performs one spiral capture maneuver at the target body; however, the HOPE mission requires two. The capture maneuver at Jupiter consists of a spiral descent to the mean altitude of Callisto’s orbit around Jupiter, and then another spiral around Callisto to descend to an orbit that is 500 km above the surface. For piloted vehicles, this same problem is encountered at Callisto orbit departure, where two departure spiral maneuvers are required to escape Jupiter. There are two ways to account for the additional ΔV needed for the Callisto spiral: (1) Let VARITOP compute the spiral down to the altitude of Callisto’s orbit around Jupiter, then, outside of VARITOP, calculate the additional ΔV needed and account for additional propellant separately, or (2) let VARITOP compute the spiral down to an altitude slightly lower than that of Callisto’s orbit around Jupiter. The resultant altitude from option (2) is calculated in such a way that the resulting spiral maneuver performs the equivalent ΔV of both the Jupiter- and Callisto-centered spiral maneuvers. The first method was used for the MPD missions. The fusion-powered missions required a completely different strategy.

For some combinations of vehicle acceleration and spiral initial or final altitude, the VARITOP spiraling approximations are not valid, which was the case for the fusion-powered missions that were considered. For those three fast missions, the initial vehicle acceleration was between 0.0005 and 0.0008 g with higher accelerations at subsequent mission phases due to propellant depletion. For these cases, figure 20 was used to approximate the velocity increment needed to escape from, or capture into, planetocentric orbits for cases where VARITOP could not. Figure 20 was first generated by Sandorff, and is based on the work of Irving and Tsien.^{16–18}

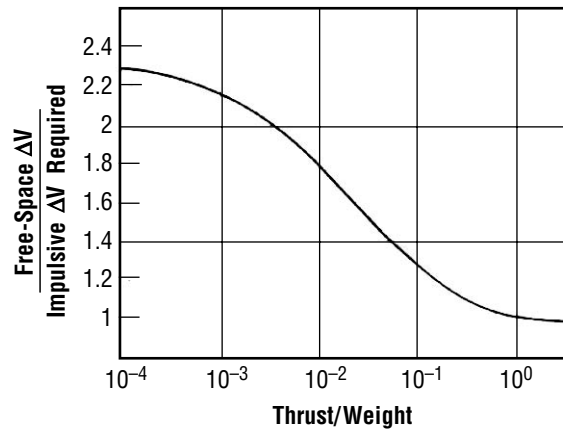


Figure 20. Penalty for low thrust in escape maneuver from satellite orbit, as compared to impulsive thrust (tangentially directed thrust).¹⁹

2.4.7 Artificial Gravity

All current artificial gravity systems involve the substitution of rotation and their corresponding centripetal acceleration for the gravity of Earth. The following types of systems are presently under consideration:

- Vehicle rotation about its longitudinal axis.
- Vehicle rotating about a lateral axis; i.e., end-over-end.
- Internal carousel rotating about longitudinal axis.
- External carousel rotating about longitudinal axis.

The following considerations and criteria were used to determine which of the possible vehicle configurations is most appropriate for extended mission artificial gravity generation:

- Comfort limit bounds for long-duration artificial gravity:
 - 0.375 to 4 rpm angular velocity.
 - 56 to 1,000+ ft rotational radius.
 - Zero to 12 percent change in gravity head to foot (gravity gradient).
 - 0.035 to 1 radial g.
 - 20 to 200 ft/s rim speed.
- Minimum energy necessary to spin up/down artificial gravity system.
- Minimum structural mass necessary to support artificial gravity system.
- Minimum overall system complexity.

- Ability to maintain spin balance—quantified by moving five crewpersons, 90 kg each, 6 m in a radial direction and determining the change in spin required to maintain spin balance (smaller change is clearly better).

The effects of artificial gravity, as they depend on rotational radius and angular velocity with their relation to the comfort zone, are shown in figure 21.

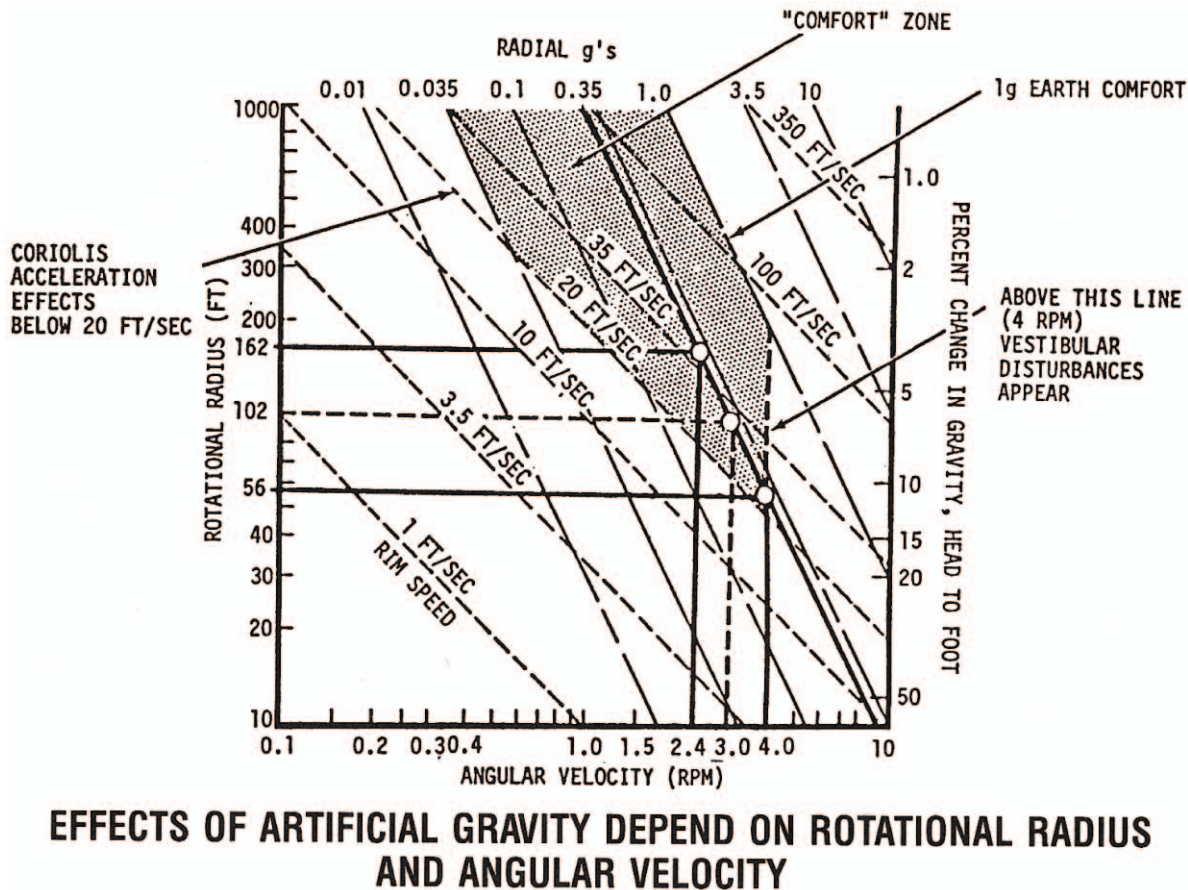


Figure 21. Effects of artificial gravity.²⁰

Note that all subcriteria for the first bullet must be met while this criterion is quantified by calculating the gravity gradient on a 1.8-m-tall crewperson for the relevant configuration.

Measurements of the current vehicle computer-aided design (CAD) model were taken and incorporated into an EXCEL[®] spreadsheet in order to quantify the various criteria. The results are shown in table 5.

Table 5. Quantitative comparison of methods for inducing artificial gravity.²¹

Concept	Criteria				
	Comfort (Δg %)	Energy to Spin Up/Down (MJ)	Δ Structural Mass (kg)	System Complexity	Spin Balance ($\Delta\omega$ rpm)
Longitudinal rotation	11.87	7,707	11,500	(1)	0.001
Lateral rotation	1.30	8,651	0	(2)	0.00002
Internal carousel	11.87	1,670	15,115+	(3)	0.003
External carousel	11.87	1,670	15,115	(4)	0.003

Concept 1 makes use of cables to reel out/in the Transhab after vehicle spin up and before vehicle spin down. The counterweight is assumed to have the mass of the Transhab plus consumables, but located at a distance of twice the tether length of the Transhab. Tether length was set at the minimum to meet comfort limit bounds. No intermodule crew movement is permitted after spin up. The crew will be uncomfortable during spin up and spin down, because the local gravity gradient and angular velocities will exceed limits. The main engines may not be fired during spin.

Concept 2 uses the current vehicle configuration with only minor structural modifications due to the differing loads during spin. Intermodule crew movement is permitted after spin up, but the main engines may not be fired during spin. The crew will be comfortable during spin up and spin down. The spin rate was set to achieve the 0.25 g required at the Transhab center of mass.

Optimization using concept 3 will require a total redesign of the crewed portion of the vehicle (also see concept 4).

Concept 4 uses opposing trusses with a Transhab on one end and a counterweight on the other. This requires a rotating joint with power, data, and fluid transfer between the crewed and uncrewed portions of the vehicle. Assuming the current airlock and transfer tunnel design, crew movement between modules is not possible. A redesign of the airlock and transfer tunnel would be a significant challenge. The truss lengths to the Transhab and the counterweight were set at the minimum required to meet comfort conditions. The crew will be comfortable during spin up and spin down, and the main engine may be fired during spin. However, unless a counterrotation device of some sort is used, thruster actuation must take precession effects into account.

Equal weight was given to all criteria. Systems were rated from 1 (best) to 4 (worst) based on the data in table 5. The resulting scores are given in table 6.

Table 6. Qualitative comparison of methods for inducing artificial gravity.

Concept	Criteria					Total Score
	Comfort	Energy to Spin Up/Down	Structural Mass	System Complexity	Spin Balance	
Longitudinal rotation	2	2	2	2	2	10
Lateral rotation	1	3	1	1	1	7
Internal carousel	2	1	4	4	3	14
External carousel	2	1	3	3	3	12

Therefore, the results, in order, are as follows:

1. Lateral rotation.
2. Longitudinal rotation.
3. External carousel.
4. Internal carousel.

All vehicles completed in this project incorporate lateral rotation.

2.4.8 General Vehicle Layout

The baseline MTF HOPE vehicle configuration is designed for launch on a Delta IV-type expendable launch vehicle. Multiple launches and in-space assembly are required due to the overall size and mass of the vehicle. The payload envelope of the launch vehicle is assumed to be approximately 5 m in diameter by 17 m in length.

The major components of the HOPE vehicle (fig. 22) follow:

- Six LH₂ tanks.
- One deuterium tank.
- The RCS thrusters and propellant tanks.
- Dual two-sided radiators for high-temperature, medium-temperature, and crew and avionics heat rejection.
- An SP-100 reactor.
- Four D-T tanks.
- A water-filled tank, which provides radiation shielding for the vehicle.
- A single MTF engine is located at the aft end of the vehicle.

The HOPE vehicle payload consists of the following:

- A surface habitat module.
- A Transhab module.
- A lander.
- An ISRU plant.

Open truss segments provide structural support of the HOPE vehicle components and the main propellant tank cluster has additional support at the forward and aft ends. The payload modules dock to a single node located at the front of the vehicle.

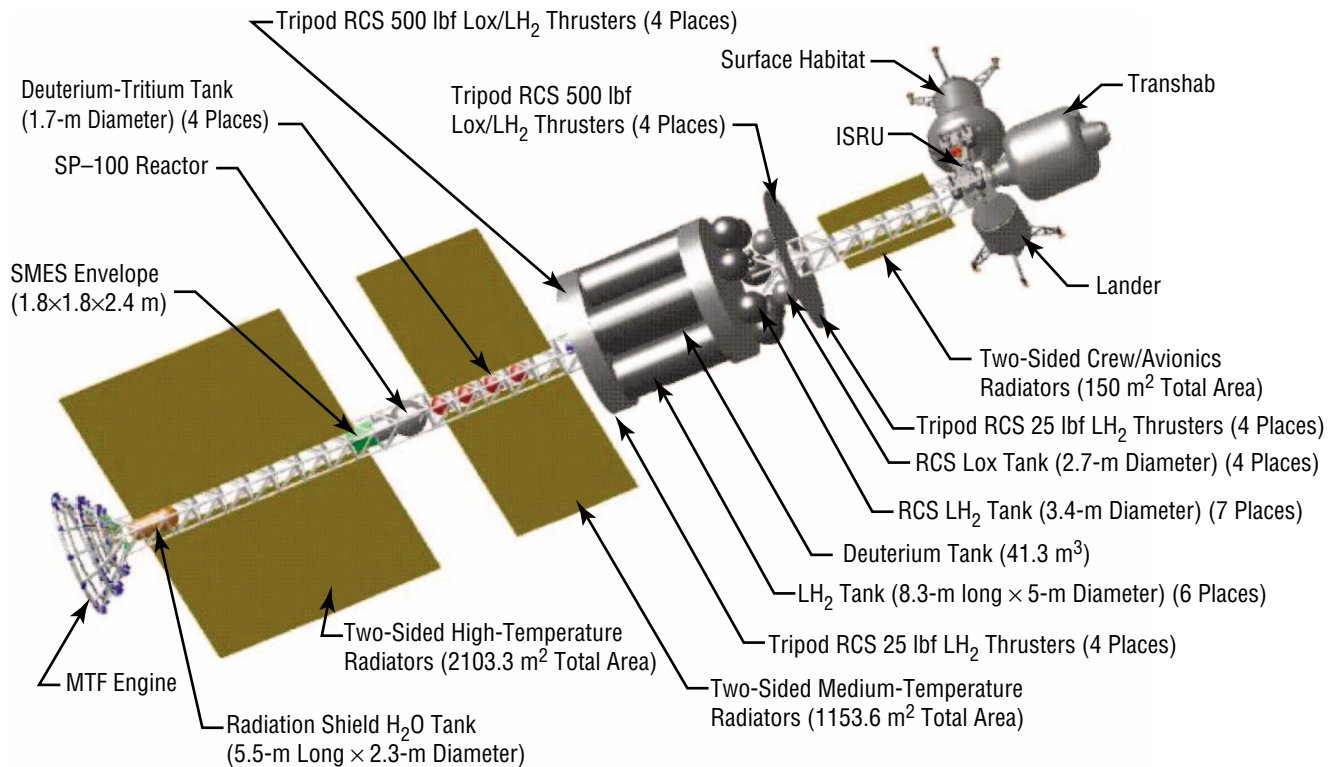


Figure 22. HOPE vehicle configuration.

The fully assembled vehicle is approximately the size of a standard football field. The HOPE vehicle overall deployed dimensions are approximately 45 m wide by 119 m long (fig. 23).

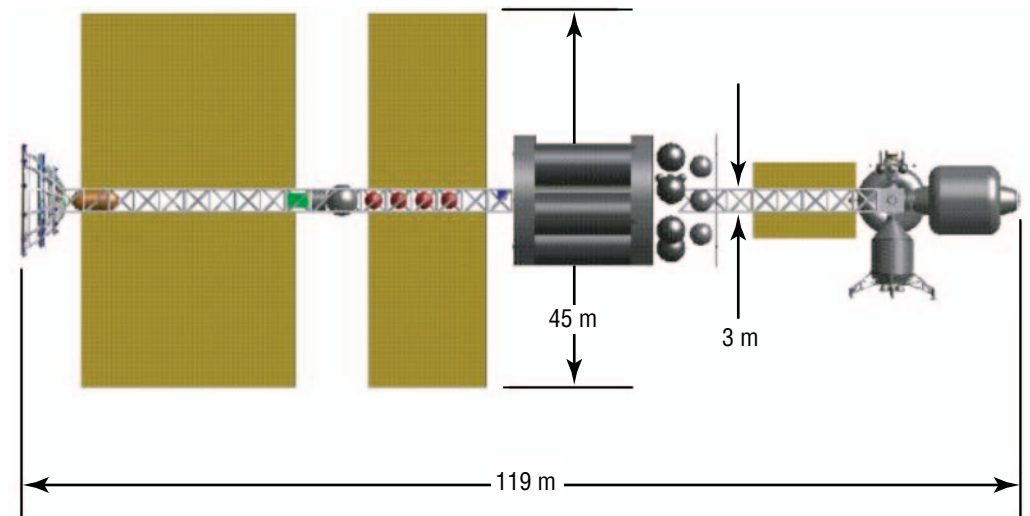


Figure 23. HOPE vehicle overall dimensions (side view).

The HOPE vehicle propulsion system components are located as close as possible to the MTF device so as to minimize weight and the routing complexity of the necessary propellant lines, coolant lines, and power system cables (fig. 24).

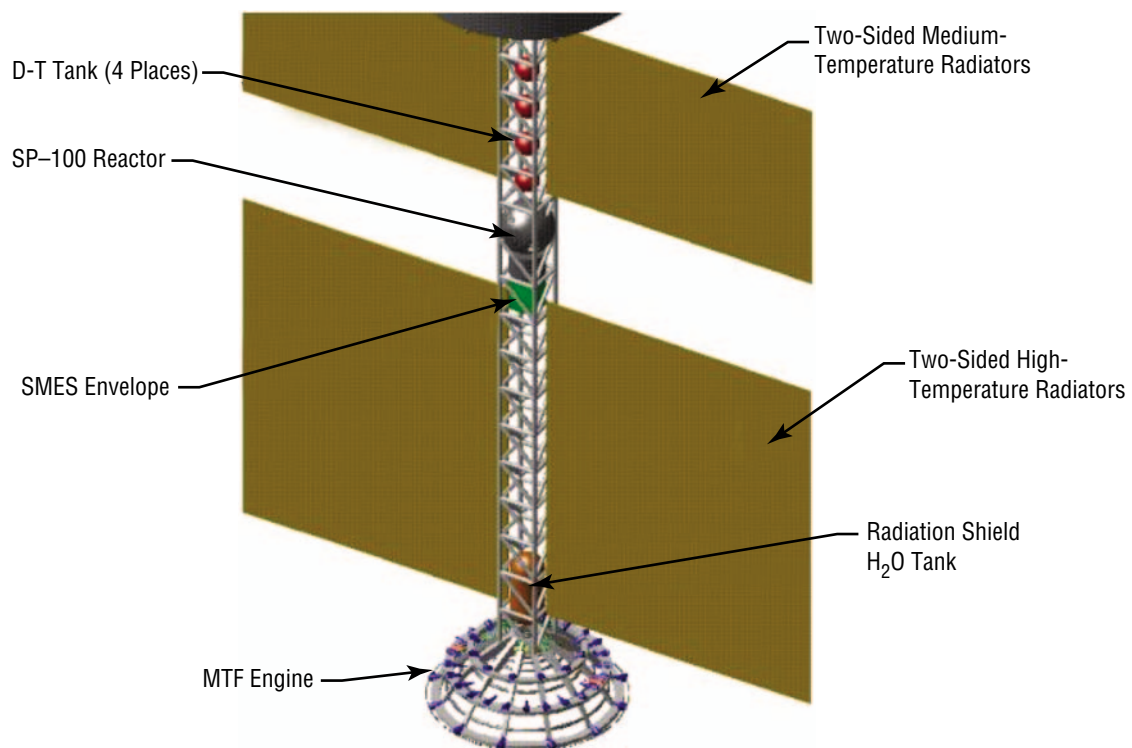


Figure 24. HOPE vehicle aft end detail.

The RCS is located close to the center of gravity of the vehicle. The distance from the propellant tanks to the thrusters is minimized in order to reduce the weight and complexity of the propellant lines. The crew and avionics radiators are located adjacent to the payload area to minimize the length of the required coolant lines (fig. 25).

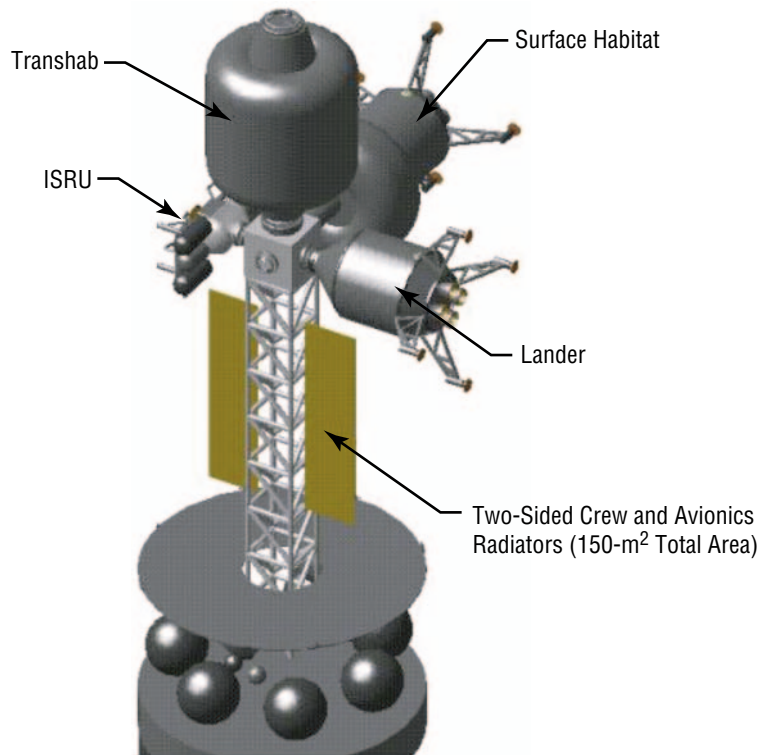


Figure 25. HOPE vehicle forward end detail.

In most respects, the designs of the MPD-propelled vehicles are similar to those of the MTF vehicles. However, the MPD vehicles required much longer trip times, necessitating continuous use of artificial gravity. To do so, a sufficient number of MPD thrusters were mounted on the side of the tank assembly to provide thrust across the longitudinal axis. The vehicle will rotate in a plane perpendicular to the axis of thrust. A typical MPD thruster configuration is shown in figure 26.

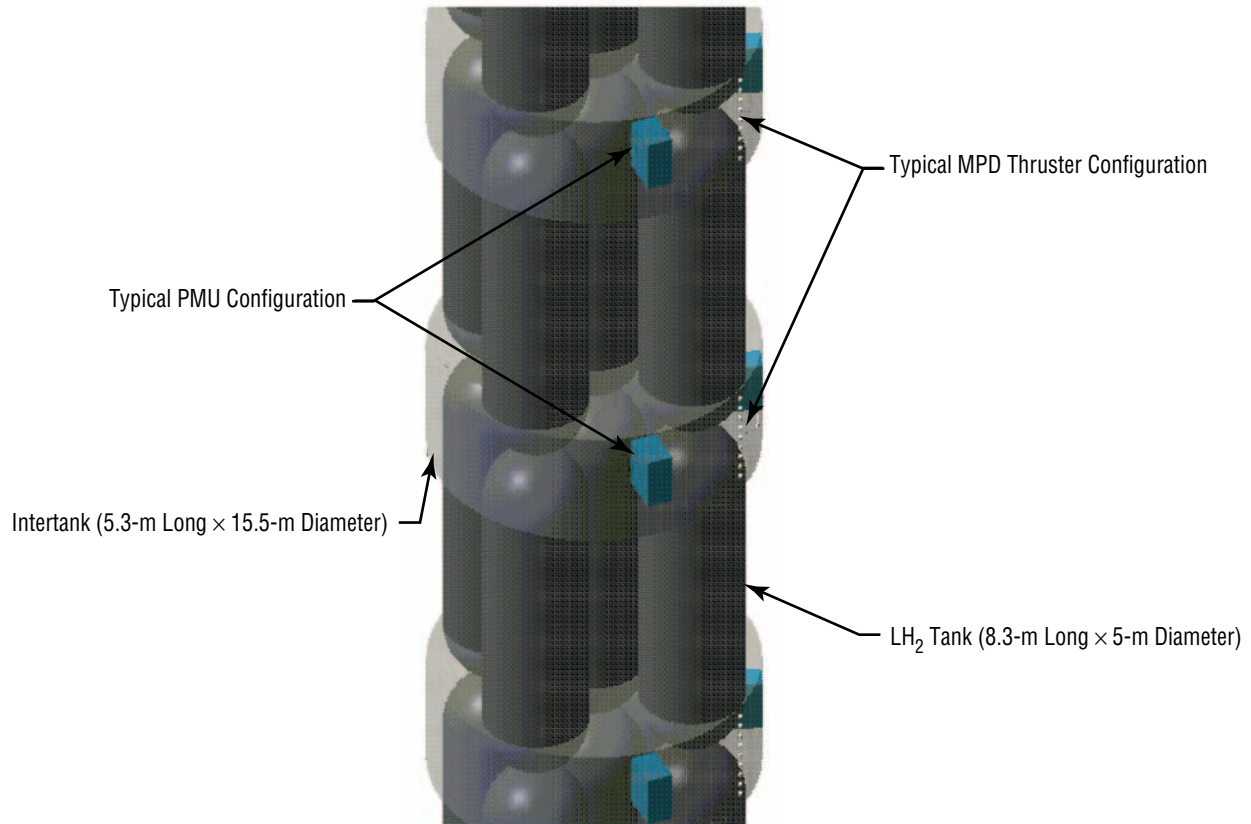


Figure 26. Typical location of MPD thrusters and PMU systems.

2.5 Magnetized Target Fusion Engine Development

This section commences with a short introduction to the process by which the plasma target is generated. The remainder of the section describes the major MTF components, as follows:

- Plasma guns.
- Magnetic field coils.
- Nozzle structure.
- Neutron protection system.
- Cooling system.
- Recharge system.
- Propellant storage and supply system.

2.5.1 Target Generation

In order to achieve a successful fusion burn, the D-T target plasma must be located at the precise focus of the MTF nozzle, the single point at which the entire array of plasma guns is aimed. To overcome the problems of both creating and accurately positioning the target plasma, the following process was adopted. A pair of conical theta pinches, located in diametrically opposite positions on either side of the

focus (fig. 27), is used to create and launch a pair of spheromak plasmoids towards the focus. The two spheromaks, which are identical in all respects except that their toroidal magnetic fields are oriented in opposite directions, collide and merge at the focus. It should be noted that, because of its minimum energy and self-generating magnetic field properties, the spheromak configuration has a relatively long life and will persist until the merging takes place. After merging is complete, the resulting plasma entity will be a field reverse configuration (FRC) plasmoid.

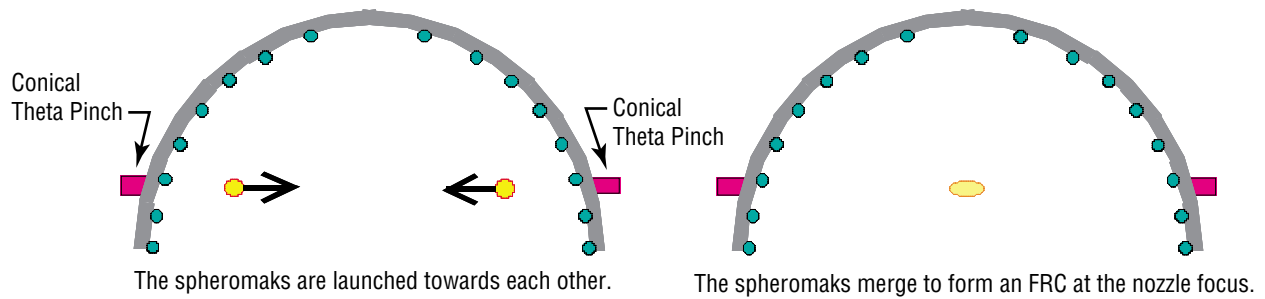


Figure 27. Conical theta pinches, spheromak creation and merging to form an FRC plasmoid.

Figure 28 shows a cross section of an individual spheromak plasmoid. Although there are both toroidal and poloidal magnetic fields, only the poloidal magnetic fields extend to the plasmoid surface.

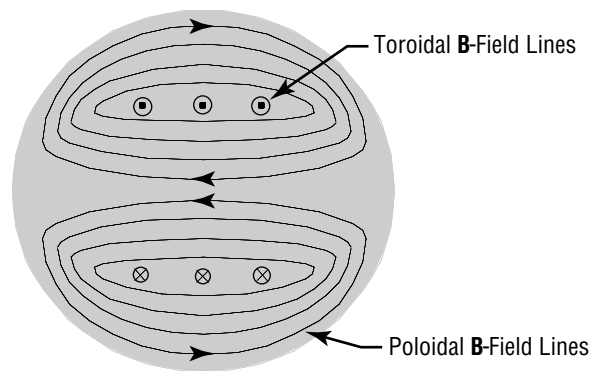


Figure 28. A spheromak plasmoid.

Figure 29 shows the two spheromaks approaching each other. They are identical in every way except that their toroidal magnetic fields are oriented opposite to each other.

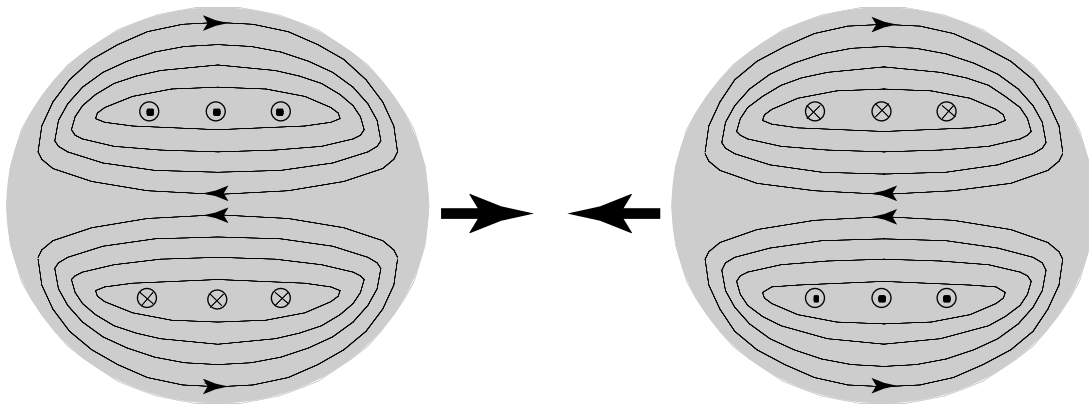


Figure 29. Two spheromaks about to merge—note opposing toroidal magnetic field directions.

Finally, figure 30 shows the single FRC plasmoid formed as a result of the two merging spheromaks. Note that the toroidal magnetic fields of the parent spheromaks cancel out, leaving a single plasmoid with solely poloidal field lines—an FRC.

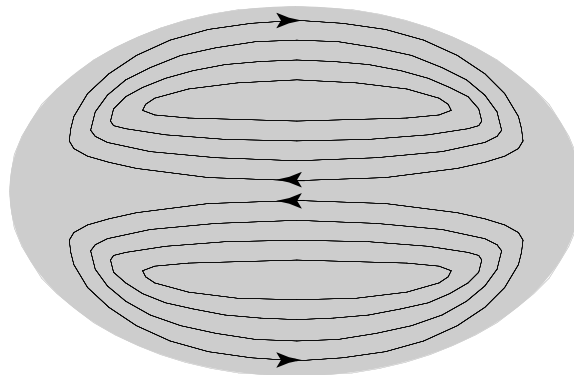


Figure 30. FRC plasmoid formed from two merged spheromaks.

2.5.2 Plasma Gun System

Shortly after FRC creation, the plasma jets arrive from the plasma guns, and compression commences. It is clearly not possible to compress the FRC isotropically. The obvious requirement for a nozzle exit (allowing the fusion products to exit the MTF device) precludes mounting plasma guns in this region. With no plasma jets incident from below, any incident from above would have the effect of prematurely pushing the FRC out through the nozzle exit. Since this is undesirable, there are no plasma guns located around the top of the nozzle. This leaves an available band that is centered around an imaginary equatorial region of the nozzle, illustrated in figure 31.

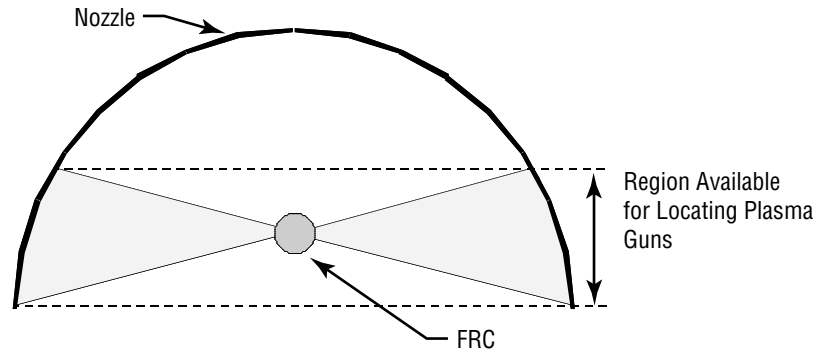


Figure 31. Region of MTF nozzle available for plasma gun location.

By locating the plasma guns within this band and ensuring that they are distributed symmetrically about the nozzle focus, which is the location of the target plasmoid at compression, the FRC will receive no net momentum.

By restricting plasma gun placement to within the allowable region, it is clear that the plasmoid will not be uniformly compressed over its entire surface by the converging plasma jets. Fortunately, this does not impede the compression dynamics. The FRC has the useful property that, when its periphery is compressed in one region, the resulting effect tends to shrink the magnetic field globally. Consequently, as the magnetic field is frozen into the highly conductive plasma, the entire FRC is compressed. Arranging the plasma jets to impact the FRC in the region shown in figure 31 will ensure that the entire FRC is compressed.

The plasma gun is illustrated conceptually in figure 32. The basic device consists of two concentric electrodes, which are connected to a high-energy capacitor. Gas is introduced into the annular gap between the electrodes, and the switch is closed. This allows the capacitor to establish a high potential difference between the inner and outer electrode. The potential gradient between the electrodes causes the breakdown and ionization of the gas, which completes the circuit and allows the capacitor to discharge.

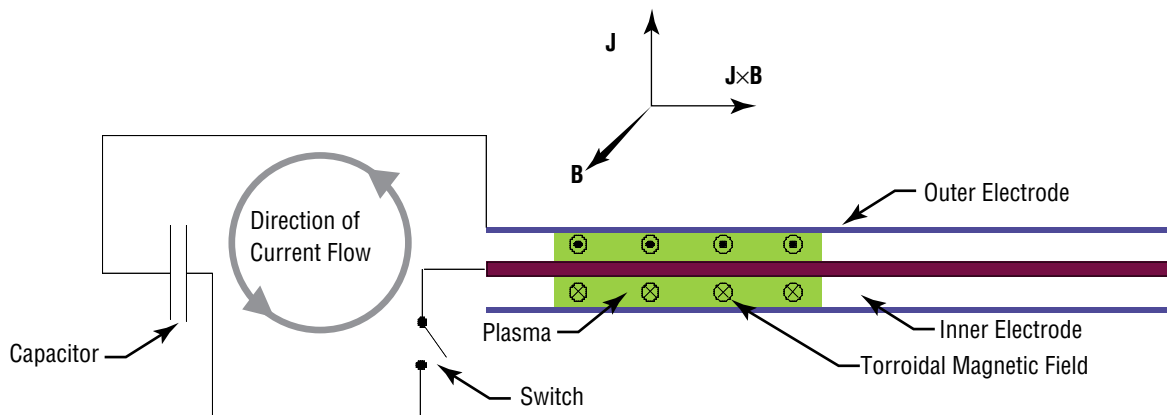


Figure 32. Plasma gun schematic design.

The direction of current flow through the completed circuit gives rise to a self-generated magnetic field, illustrated in figure 32. The field lines are oriented toroidally around the inner electrode. This self-generated field is perpendicular to the direction of current flow everywhere, which in this example, is shown passing in a radial manner outwards from the inner to the outer electrode. This gives rise to a $\mathbf{J} \times \mathbf{B}$ force on the plasma, where \mathbf{J} and \mathbf{B} denote current density and magnetic field strength, respectively (fig. 32), which forces it out of the device at very high speed. Note that as the primary element of the plasma current is due to electron motion, electrons are what first experience the major part of the electromagnetic acceleration force. However, the very strong electrostatic forces, which are generated within the plasma as soon as any charge separation begins to occur, ensure that the ions are accelerated along with the electrons. The fact that it is a quasineutral plasma that is accelerated out of the device is significant in that it reduces concerns over the effect of space-charge limitations on the subsequent behavior of the plasma jet.

The actual design of the plasma gun is rendered slightly more complex by the need to focus the plasma jet and counteract its natural tendency to diverge due to gas pressure. The solution to this problem is illustrated in figure 33, which shows the accelerator portion of the device in greater detail and with greater realism than figure 32. Each plasma gun is ≈ 1 m in length without the attached capacitor, 1.4 m with the capacitor, and has a maximum barrel diameter of 0.25 m. The barrel and capacitor are fitted together using a scyllac fitting to reduce impedance mismatch.

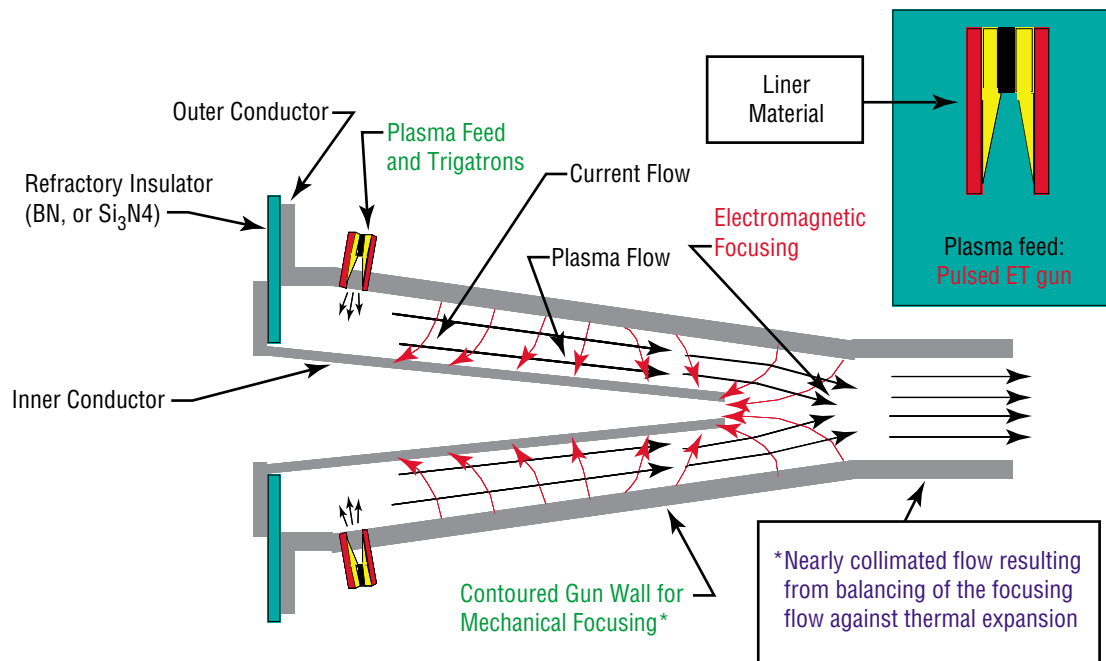


Figure 33. Plasma gun barrel design.

The converging two-barrel arrangement with each barrel contoured internally achieves the necessary focusing effect. Barrel shape must be such that the combination of electromagnetic and thermal expansion forces equal each other. This results in a nearly-collimated high-speed gas flow.

The MTF plasma gun system consists of a total of 48 plasma guns, all positioned around the magnetic nozzle and directed towards its focus (fig. 34).

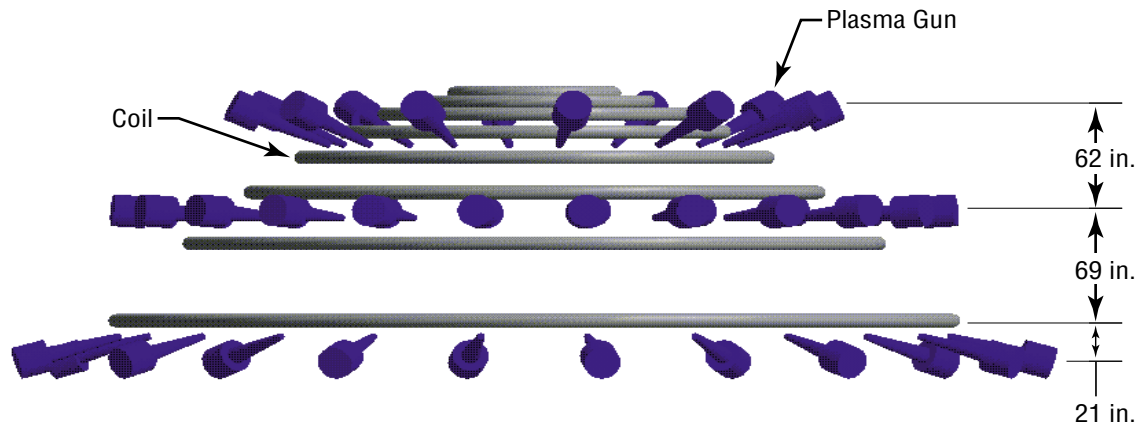


Figure 34. Location and orientation of plasma guns relative to the coils.

The 48 plasma guns are divided into three banks. The upper bank, 12 guns, is located above the nozzle focus. The middle bank, 24 guns, is level with the focus. The lowest bank, 12 guns, is located below the focus.

Each plasma gun has its own individual capacitor to provide electrical power during discharge. Each gun delivers a collimated plasma beam at a velocity of 125 km/s. As explained earlier, the small leading portion of each beam consists of deuterium plasma, and the remainder consists of hydrogen plasma.

Note that when the plasma guns are discharged to produce the converging plasma jets that are aimed at the target, the nozzle magnetic field is not present. Only after the plasma jets are near to the target is the nozzle field initiated. This prevents the magnetic field from interfering with the plasma jet trajectories.

2.5.3 Magnetic Field Coils

The nozzle magnetic field performs two essential functions. First, it acts as a shock absorber, taking the momentum of the expanding plasma cloud and transmitting it to the vehicle as a thrust force. Second, by slowing the expanding plasma cloud and then redirecting it back out of the nozzle, the magnetic field protects the structure and physical components of the nozzle from the extremely high temperatures and direct damage due to charged particle impacts. The current-carrying coils, responsible for producing the magnetic field, are the primary nozzle components.

Eight single-turn coils are placed in a parabolic arrangement around the nozzle (fig. 34). This configuration produces parabolic field lines whose focus coincides with the location of the fusion event. In order to close off the vertex of the magnetic field parabola and to prevent plasma from passing up along

the axis, a single reversed conical theta pinch is installed at the vertex of the nozzle. Each of the eight coils (and the reversed conical theta pinch) is actually composed of two separate coil assemblies; i.e., an inner seed field coil and an outer thrust coil.

An applied current in the seed coils immediately prior to the fusion event produces the initial seed magnetic field. As the plasma cloud expands, postfusion, it deflects and compresses the seed field—the highly conductive plasma closely approximates the frozen field-line model and thus resists incursion of the field. Plasma cloud expansion also induces very large currents in the outer thrust coils, also referred to as the main coils. These currents interact with the magnetic field, which strengthens as it is compressed by the expanding plasma cloud, to produce a very large $\mathbf{J} \times \mathbf{B}$ force on the main coils.

2.5.3.1 Seed Coils. Each seed field coil consists of a superconducting $\text{YBa}_2\text{Cu}_3\text{O}_7$ single-turn loop that is energized by the SMES via a coaxially arranged superconducting power bus (of which further details are given later). The seed field coil is cooled with cryogenic LN_2 , which flows through the conductor cable mesh. Superconducting coils are used to minimize the power loss due to ohmic heating. Once the seed field coils are energized, they produce the initial field within the nozzle.

2.5.3.2 Main Coils. Each main or thrust coil is laid coaxially over its associated seed field coil and, unlike the seed field coil, makes a continuous single turn loop. Because the main coil operates at high temperature, it is comprised of a thin layer of titanium diboride and molybdenum (TiB_2/Mo) metal matrix composite. This material has a conductivity comparable with that of copper, and a melting temperature in excess of 3,000 K. The thickness of the conductor is set in order that the relatively slowly changing magnetic flux of the seed field coil can pass through it, but the more rapidly changing compressed flux is completely absorbed. The main coil is responsible for transforming the compressed magnetic flux inside the nozzle to a thrust force. This is accomplished by the Lorentz forces generated from the large magnetic field inside the nozzle and the very large (mega-amp level) currents induced in the main coils by the compressed magnetic field.

2.5.3.3 Coil Structural Design. Between the large oscillatory impulses of the fusion events and the magnetic hoop stresses in the coils, the nozzle must withstand high-dynamic loading conditions. Most of these forces are coupled to the structure through the coils that, as a result, must be structurally robust. This requirement along with the dielectric and thermal requirements of the coils makes material selection difficult. To solve these issues, advanced composites and ceramics must be used; their superior strength, dielectric properties, and high melting temperatures allow for strong lightweight components. Also, because they can be laid up together, their use should reduce the need for complex machining.

Ceramics are, however, extremely brittle and cannot withstand significant dynamic loading. Although they show exceptional strength against compressive loads, they have very low tensile strength. For this reason, it is important to lay up these materials in such a manner that the loads can be transferred to an outer carbon-carbon composite that does have excellent tensile strength. A typical coil cross section is shown in figure 35, and its corresponding dimensions given in table 7.

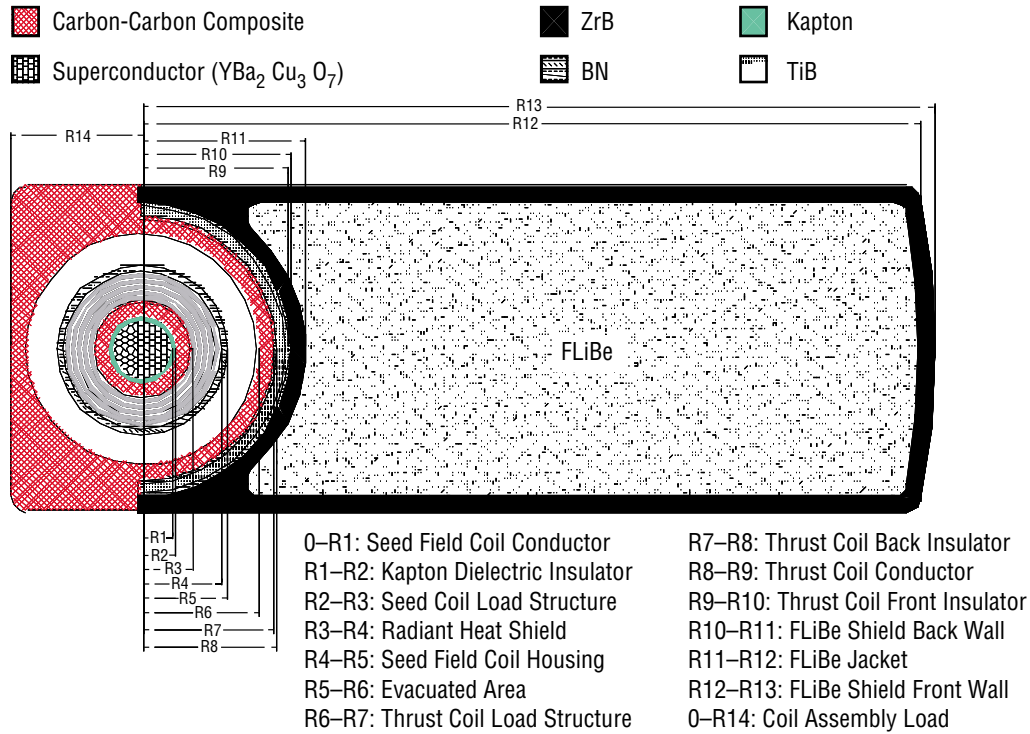


Figure 35. MTF nozzle coil assembly cross section.

Table 7. MTF nozzle coil assembly dimensions.

Coil No.	R1 (cm)	R2 (cm)	R3 (cm)	R4 (cm)	R5 (cm)	R6 (cm)	R7 (cm)	R8 (cm)	R9 (cm)	R10 (cm)	R11 (cm)	R12 (cm)	R13 (cm)	R14 (cm)
1	0.33	0.43	0.93	1.93	2.13	3.13	3.63	3.73	3.77	3.87	4.37	24.37	24.87	3.63
2	0.37	0.47	0.97	1.97	2.17	3.17	3.67	3.77	3.83	3.93	4.43	24.43	24.93	3.67
3	0.42	0.52	1.02	2.02	2.22	3.22	3.72	3.82	3.89	3.99	4.49	24.49	24.99	3.72
4	0.47	0.57	1.07	2.07	2.27	3.27	3.77	3.87	3.97	4.07	4.57	24.57	25.07	3.77
5	0.54	0.64	1.14	2.14	2.34	3.34	3.84	3.94	4.06	4.16	4.66	24.66	25.16	3.84
6	0.63	0.73	1.23	2.23	2.43	3.43	3.93	4.03	4.19	4.29	4.79	24.79	25.29	3.93
7	0.76	0.86	1.36	2.36	2.56	3.56	4.06	4.16	4.39	4.49	4.99	24.99	25.49	4.06
8	0.97	1.07	1.57	2.57	2.77	3.77	4.27	4.37	4.72	4.82	5.32	25.32	25.82	4.27

This paragraph describes a typical coil cross section (refer to fig. 35). At the center of the coil assembly is the seed field coil conductor, which consists of a mesh of superconducting material that uses a 3:1 conductor-to-coolant gap ratio. This allows adequate cryogenic coolant to flow along the conductor and still remain below its critical temperature. A layer of Kapton® dielectric material surrounds the conducting mesh. This material serves as an electrical insulator and prevents arcing within the coil. The current through

the seed field coil will cause it to undergo large hoop stresses due to the magnetic pressure within the loop. Because the current is pulsed, the seed coil will undergo a large number of stress cycles during operation. A layer of carbon-carbon composite is wrapped around the thin layer of Kapton to prevent strain on the seed field coil. Outside the carbon composite are five layers of low-emissivity polished aluminum, each is 1 mm in thickness and separated by 0.8-mm-thick evacuated regions. These alternating layers serve as a radiant-energy heat shield and prevent heat from the thrust coil from penetrating into the seed field coil. The coaxially layered aluminum layers are electrically continuous so that no net current can be induced in them by the varying seed field flux. This assembly is covered with a thin layer of boron nitride (BN) to serve as a lightweight high-temperature casing.

The thrust coil assembly surrounds the seed field assembly, and they are separated by an evacuated section, 0.5 cm thick. This further reduces heat conduction from the high-temperature thrust coil into the cryogenic-temperature seed field coil. Beyond this evacuated region is the structural carbon-carbon composite support for the thrust coil assembly. Loads from the thrust coil conductor are transferred into this support, and thus, into the nozzle as thrust. Both the thrust and seed field coils are structurally tied to the main support splines of the magnetic nozzle. The thrust coil conductor forms a C shape when viewed in cross section, and the convex part of the C points towards the central axis of the nozzle. Since there is no magnetic flux compression outside the MTF nozzle, there is no need for a conductor on the outer side of the coil assembly; i.e., furthest from the nozzle central axis. The high-temperature TiB_2/Mo thrust coil conductor is completely surrounded by a layer of BN. In addition to being a high-temperature ceramic, BN has excellent dielectric properties and can prevent arcing from within the coil.

To complete the thrust coil assembly, a molten salt coolant jacket is placed between the thrust coil conductor and the focus of the nozzle. This coolant jacket is made from zirconium diboride (ZrB_2), a high-temperature ceramic that is not prone to reaction with the molten salt coolant.

2.5.4 Magnetic Nozzle Structure

As shown in figure 36, the coil assemblies, target generators, and plasma guns are all mounted on a structural framework that serves to hold the various components in their correct location and also transmits the thrust force to the remainder of the vehicle. The structure consists of 12 equally spaced tapered splines, each of which extends from very near the apex of the device to some distance below the focus. In keeping with the nozzle profile, each spline has a near-parabolic profile. Four rings complete the structure (fig. 36). Both the splines and the rings are constructed of a carbon-carbon composite.

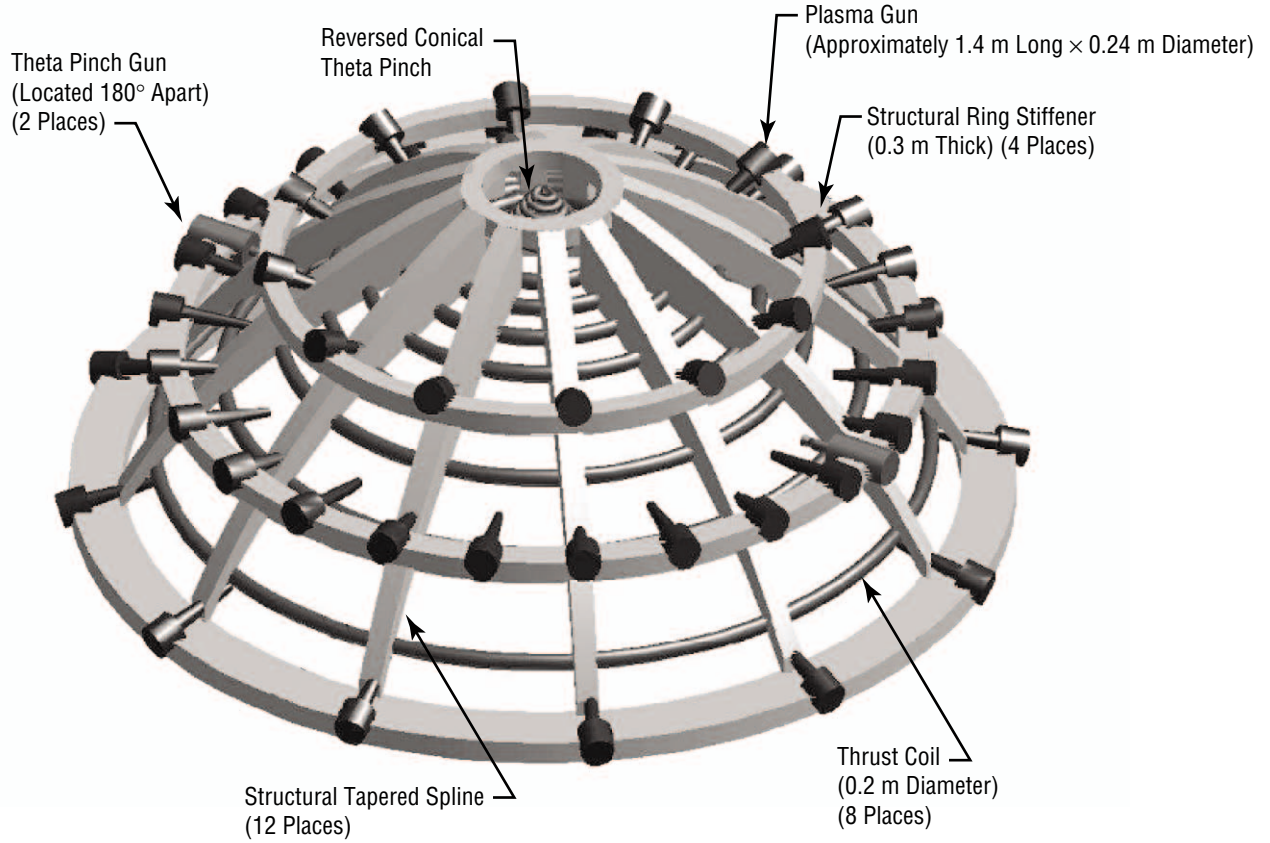


Figure 36. Location of major components.

2.5.5 Neutron Protection

The D-T fusion reaction, which takes place in the target plasmoid, can be written as follows:²²

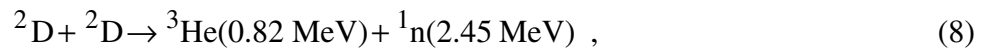


where ^2D , ^3T , and ^4He denote deuterium, tritium, and helium-4 nuclei, respectively, and ^1n denotes a neutron. The reaction product energies are indicated in parentheses.

The D-D fusion, which takes place in the inner portion of the plasma liner, can proceed according to two different reactions, which can be written as follows:²²



or



where ^1p and ^3He denote a proton and a helium-3 nucleus, respectively.

The charged particle products of both the central and liner reactions can be deflected by the nozzle magnetic field, imparting useful impulse to the vehicle without making physical contact. However, the neutrons, from both the core D-T and the liner D-D reactions, being electrically neutral, cannot be deflected. Despite the relatively open design of the nozzle lattice, which permits a significant proportion of the neutrons to escape, those that do impact present one of the principal design challenges for an MTF propulsion system.

This challenge manifests itself in several ways. First, it is necessary to protect the nozzle, including the structure, coils, plasma guns, and other components, from the physical damage that would otherwise result from high-energy neutron bombardment. Second, some radioactivity is induced in the MTF structure because slow neutrons striking the nozzle may be absorbed by the nuclei of those atoms that compose the structure, thus, rendering them radioactive. Third, as the neutrons, particularly those originating from the central D-T reactions, have very high energies, they impart a significant amount of thermal energy to the nozzle when they impact. Removing this very large heat flux and limiting the nozzle material temperatures in order to maintain mechanical properties are major challenges.

In mitigation, it is noted that a significant degree of neutron moderation is likely to take place in the outer regions of the plasmoid. Immediately following fusion, when the thermonuclear neutrons are traveling outwards from the central regions, the density of the surrounding layers of compressed hydrogen will be very great. It is likely that a significant amount of neutron moderation will take place within this region, partially due to the high density and partially due to the excellent moderating capabilities of the hydrogen nucleus, which is the most abundant nucleus present. A full analysis of this process has yet to be conducted. Accordingly, a somewhat pessimistic assumption of only 20 percent moderation has been made for the purposes of the HOPE design study. At some later stage when the necessary moderation analysis has been conducted, it should be possible to favorably revise the MTF design. Neutron shielding and thermal control system masses should decrease.

Neutrons can cause damage to materials in a variety of ways. Their total integrated flux—defined as the fluence—must be limited to prevent damage. High-energy neutrons normally pass through most materials without any atomic collisions, simply because of the relatively small size of the nucleus. However, where collisions do occur, they can result in atomic displacements, where the atom is effectively driven out of its location in the crystal matrix. This phenomenon is referred to as neutron embrittlement and can be thought of as a microscopic strain hardening mechanism. If a large enough number of these events occur, as is the case in high-radiation environments, the material will lose many of its structural, electrical, and heat conduction properties. Structural elements can fail, heat exchangers can lose performance, and electrical conductors can increase in resistivity. Without appropriate protective steps, all of these reactions would result in a decrease in the performance of the MTF propulsion system.

Low-energy neutrons can also produce adverse effects. Neutrons at low energies are more easily absorbed by atomic nuclei, usually resulting in the creation of a radioactive isotope. This too can change material properties and can cause problems with electronic circuitry. Fortunately, for most materials, there exists a range of energies at which the neutrons are too energetic to be absorbed yet low enough to pass through without interacting with the nuclei. Within this energy range, the material is effectively transparent to the neutrons.

Designing a neutron radiation shield capable of moderating neutrons with a range of initial energies would be a challenging task. It would probably necessitate the use of a composite shield, consisting of many different layers of materials, with the outer layers slowing down fast neutrons but allowing slower ones to pass to the next layer. Each successive layer would have to repeat this process until all the neutrons were moderated to the appropriate energy. Such a shield would act as a neutron filter and would require much less mass than conventional shielding. Unfortunately, the design of such a tailored shield was not possible within the scope of the HOPE study. With available techniques, at best, a large population of the high-energy neutrons can be reduced to a level of transparency. The fusion community is currently experimenting with the molten salt FLiBe (a mixture of lithium fluoride and beryllium fluoride, pronounced “FLiBe”).²³ FLiBe has a good atomic cross section for slowing neutrons, a high vaporization temperature, and an acceptable viscosity.

In addition to its shielding properties, liquid FLiBe can also serve as a primary cooling fluid. This yields a particularly efficient design solution, since the material into which the neutron thermal energy is first deposited (the FLiBe) is also the medium that carries it away from the nozzle. The neutron energy must be pumped out of the system so that a nozzle operating temperature no greater than 1,500 K is maintained. This is in keeping with the maximum operating temperature that the hottest portions of the nozzle can withstand. It also ensures that the FLiBe remains below its vaporization point.

For these reasons, FLiBe was selected as the neutron shield material and active cooling fluid for the MTF nozzle.

2.5.6 Main Cooling System

At the focus of the MTF nozzle, the fusion reactions can produce plasma temperatures as high as 300 million K (the approximate temperature at which D-D fusion occurs). Fortunately, cooling, which accompanies the plasma expansion process, and the magnetic fields within the nozzle both prevent material from coming in contact with the structure while at these high temperatures. However, these mechanisms do not prevent radiant electromagnetic (Bremsstrahlung) and neutronic radiation from reaching the nozzle structure. If left uncooled, the nozzle would quickly exceed its maximum allowable operating temperature and melt, primarily on account of the neutron energy; therefore, an active cooling system is needed to prevent the MMW heat input to the structure.

The resulting cooling system employs a complex network of coolant channels running throughout the MTF nozzle structure and the coils. A variety of high-temperature liquid metal and molten salt coolants flow within these channels, which ultimately transfer the heat away from the MTF device and out to a radiator array for radiative disposal into space.

As explained earlier, the coolant must serve two purposes: (1) It must carry away heat at a high temperature while remaining a liquid, and (2) it must also serve as a radiation shield for the nozzle structure. Gamma radiation, when absorbed by a material, simply produces an increase in temperature. Although the heat from the gamma rays must be removed, it causes little damage when compared to that of the neutrons.

FLiBe flows down each of the 12 structural splines (fig. 36) of the MTF nozzle along cooling channels below the surface facing the nozzle focus, and it returns along a manifold located on the outward-facing surface of the spline. FLiBe channels are also placed along the sides of each spline to serve as feed and return manifolds for the cooling channels that are located along the structural ring stiffeners and the magnetic coils between each spline. FLiBe flows down the feed manifold on the right side of a spline. This manifold feeds eight coil coolant channels and three ring-stiffener coolant channels. All of these feed into the return manifold located on the left side of the adjacent spline, which splits the MTF nozzle into 12 different main circuits. All of these circuits are combined into a common, structurally integrated feed and return manifold found at the interface of the MTF nozzle and vehicle.

High-temperature FLiBe leaves the MTF nozzle along the common return manifold and feeds into a heat exchanger, which is part of a Brayton power cycle that uses helium as its working fluid. The Brayton system converts some of the heat of the MTF nozzle to mechanical energy, using a gas turbine that drives the power cycle compressor, FLiBe pump, and the cryocooler used with the SMES system. The remaining waste heat is transferred to a radiator via a NaK working fluid heat exchanger. The cooled FLiBe is sent to the FLiBe pump and returned to the MTF nozzle along the common feed manifold.

The Brayton power cycle heat exchanger also serves an additional function. Since the MTF propulsion system must be shut down during various phases of the mission; e.g., while at the destination, the heat source that normally maintains the molten FLiBe's liquid state will be absent. From an operations perspective, it is undesirable to allow the FLiBe to solidify. The HOPE vehicle utilizes an SP-100 fission reactor to provide nonpropulsive power for mission operations. This is a 375-MW electrical (2-MW_{th}) output reactor that uses an LMR power cycle. Usually the waste heat from this power system is sent to a separate radiator array. When the MTF propulsion system is inactive, heat from the SP-100 can be sent to the Brayton cycle heat exchanger to keep enough heat in the FLiBe so that it will remain liquid. During these periods, the pump system operates at a lower duty cycle than when the MTF propulsion system is active. The thermal schematics for these systems and for the hotel waste heat rejection; i.e., heat rejected from the crew quarters and other elements of the payload, system are shown in figure 37.

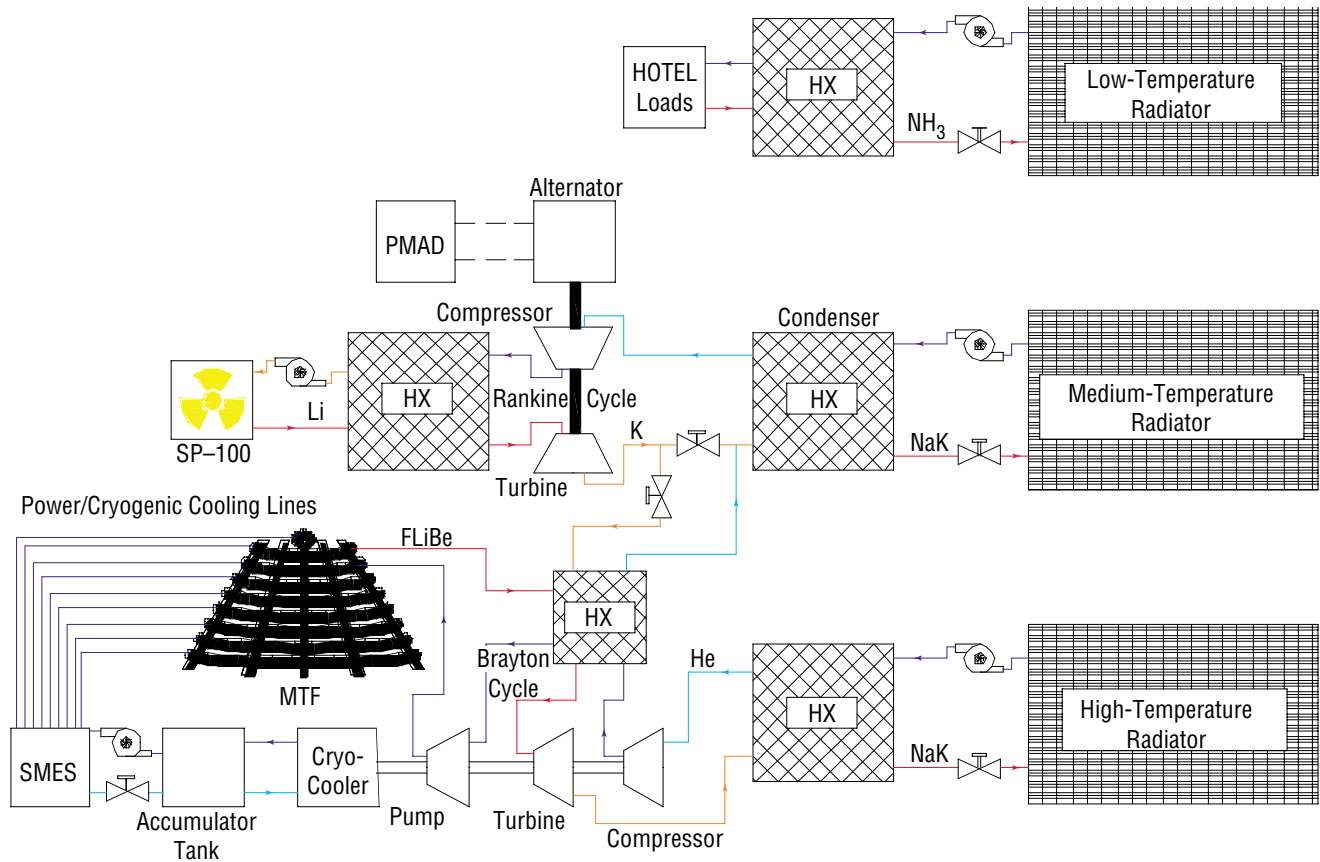


Figure 37. MTF thermal management schematic.

2.5.7 Recharge System

The recharge system is responsible for converting a small portion of the expanding plasma cloud's kinetic energy to usable electric power for the magnetic seed field coils and the plasma guns. The plasma expansion process induces large currents in the thrust coils, some of which can be commutated out of the coils and used for recharging the system. The circuit diagram for this system is shown in figure 38.

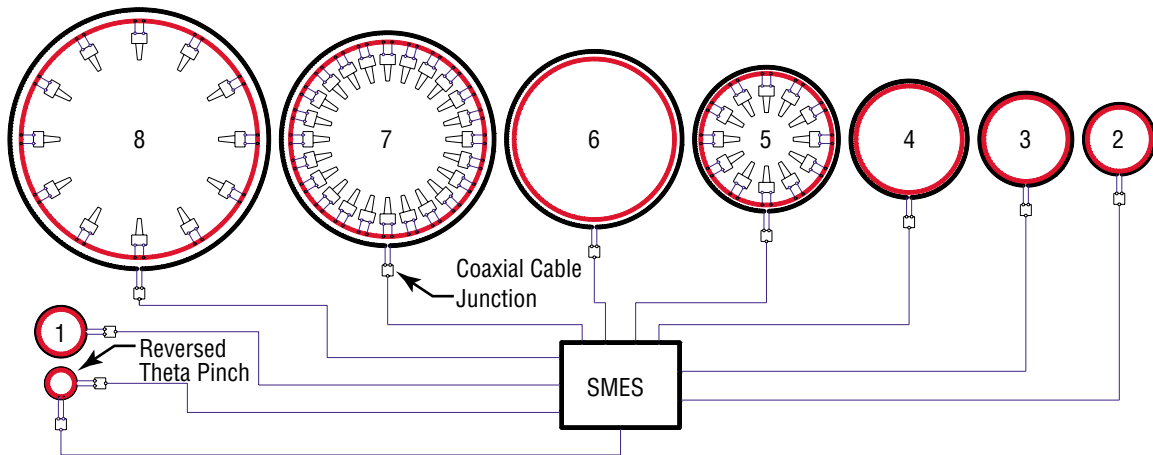


Figure 38. Recharge system schematic.

The three plasma gun banks are located along different coils; i.e., numbers 8, 7, and 5—where the coils are numbered in order of increasing size. Each individual coil is responsible for charging the bank of plasma guns that it supports. Each plasma gun has its own charging circuit that is connected to the thrust coil in such a way that the impedance value of the circuit lines, capacitor, and the section of the thrust coil isolated by the charging circuit terminals are equal. This ensures that only the amount of power needed to charge the capacitor can be tapped from the thrust coil. The charging circuit requires a high-duty switch to isolate the capacitor from the thrust coil. Although a spark gap system can provide the needed performance, life limitations would probably ultimately make an advanced switching system desirable.

As mentioned earlier, the seed field coils draw power from a SMES, which has the capability to accept and discharge large amounts of electrical energy in a very short period of time. The SMES is connected to and receives power from the thrust coil conductor of the reversed conical theta pinch, which is located at the vertex of the MTF nozzle. Electrical energy, generated inductively in the thrust coil conductor, is transmitted to the SMES. This energy is stored within the SMES in the form of a magnetic field and, at the appropriate time, transmitted to the seed field coils to produce the initial magnetic field lines inside the MTF nozzle prior to initiation of the next fusion event. This charging circuit is shown in figure 39.

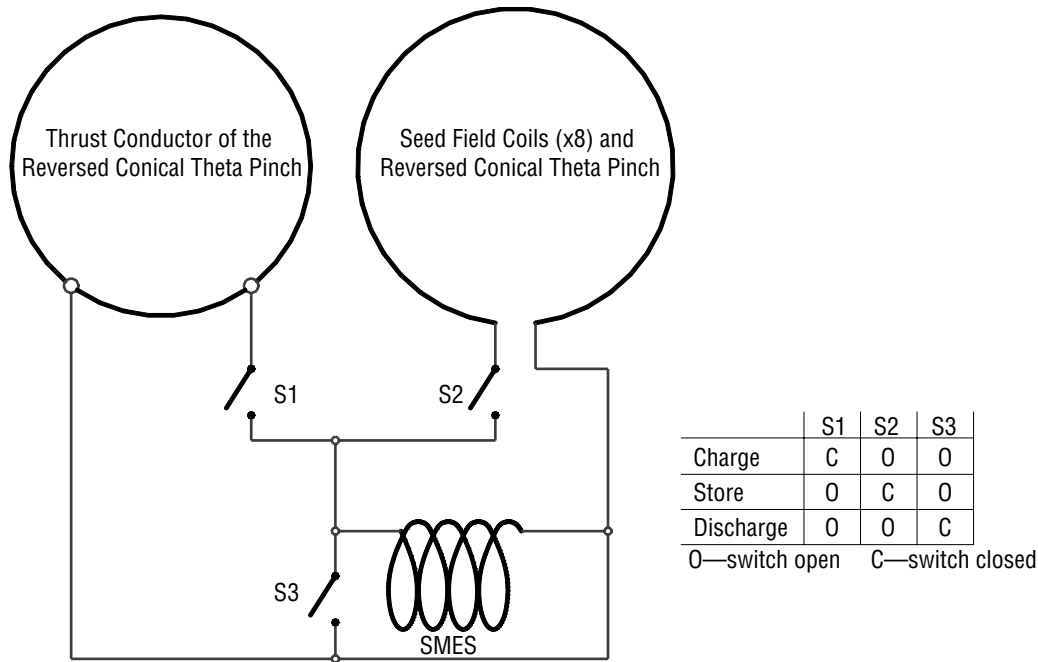


Figure 39. SMES charging circuit.

Power is transmitted to and from the SMES via superconducting coaxial transmission cables. Since the SMES, transmission lines, and seed field coils are all superconducting, they share a common cryogenic cooling system. LN_2 is cooled in an accumulator tank by a cryocooler and delivered to the SMES (fig. 39). It then travels down the transmission lines, flows around the seed field coils, and finally, back up the transmission lines to the SMES and accumulator tank for recooling.

Since the transmission lines must both carry and return the cryogen coolant, they require two coolant channels. Because the overall diameter of the transmission lines is not as critical as that of the coils, and in the interest of minimizing coolant flow frictional losses, a wet mesh arrangement is not used. This allows one coolant channel for each conductor in the cable. The transmission lines run along the MTF nozzle structure to the different coils in a nonsymmetrical fashion. This could affect the symmetry of the nozzle magnetic field; therefore, coaxially arranged conductors are used to reduce the magnetic field produced along the pulsed transmission lines. A radiant heat shield is also employed on the transmission lines. The resulting transmission line design is shown in figure 40 with dimensions given in table 8.

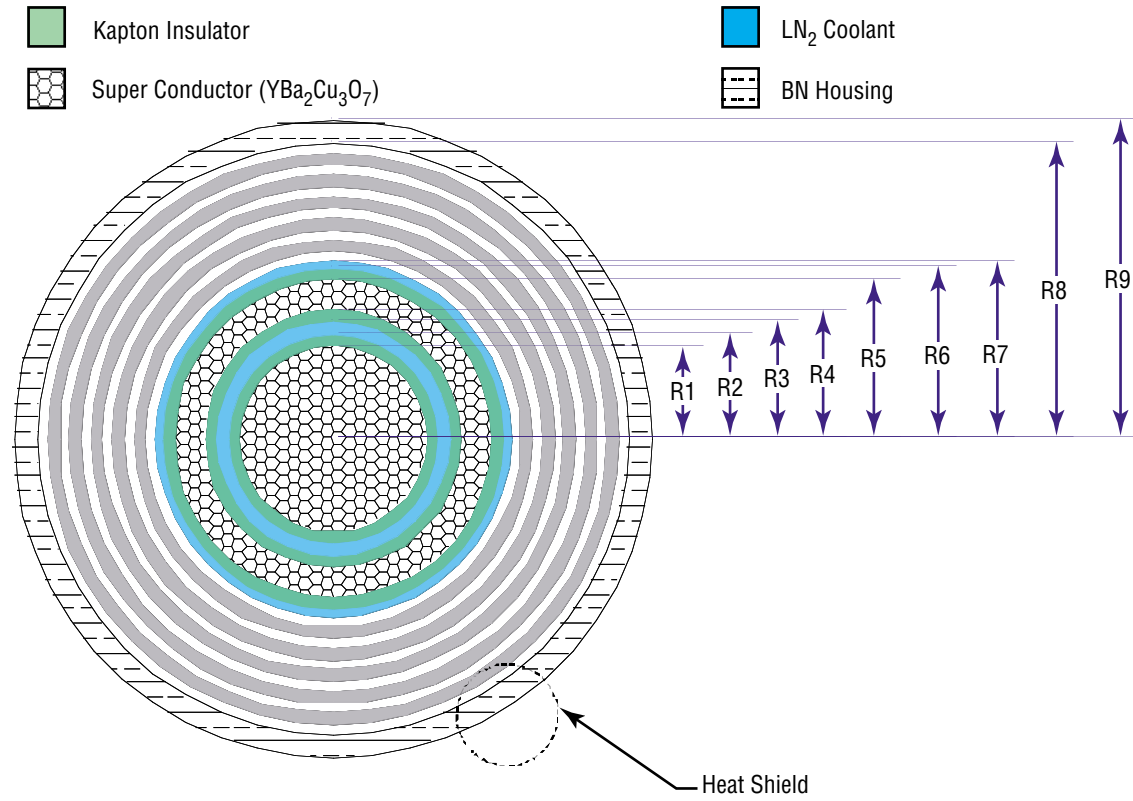


Figure 40. Transmission line cross section.

Table 8. Transmission line cross-section dimensions.

Coil No.	R1 (cm)	R2 (cm)	R3 (cm)	R4 (cm)	R5 (cm)	R6 (cm)	R7 (cm)	R8 (cm)	R9 (cm)
1	0.27	0.37	0.39	0.49	0.56	0.66	0.68	1.68	1.88
2	0.30	0.40	0.43	0.53	0.61	0.71	0.73	1.73	1.93
3	0.34	0.44	0.48	0.58	0.67	0.77	0.79	1.79	1.99
4	0.39	0.49	0.53	0.63	0.74	0.84	0.87	1.87	2.07
5	0.44	0.54	0.59	0.69	0.82	0.92	0.95	1.95	2.15
6	0.52	0.62	0.68	0.78	0.93	1.03	1.07	2.07	2.27
7	0.62	0.72	0.80	0.90	1.09	1.19	1.24	2.24	2.44
8	0.79	0.89	0.99	1.09	1.35	1.45	1.51	2.51	2.71

2.5.8 Propellant Storage and Supply

The MTF device requires three separate propellants, each with its own separate storage and supply system.

A 50–50 molar mixture of deuterium and tritium is stored as a high-pressure gas and, after suitable pressure regulation, fed to the two conical theta pinches to produce the spheromaks, which ultimately merge to create the FRC target plasma. The very small quantity of plasma required to create the target (≈ 1 mg/pulse), coupled with the need for a relatively precise mixture of the two isotopes, makes common storage attractive. Statistical mechanics naturally ensure a virtually perfect 50–50 molar mixture without any need for complex independent metering systems for the two gases.

The plasma gun system requires two separate propellant supply systems. One feeds deuterium, for use at the very front of the gun's discharge plasma jet. The second, which provides the bulk of the plasma, is for (normal isotope) hydrogen. For the hydrogen, which comprises the bulk of the total propellant load, volume constraints make liquid storage the only viable option. This does not pose significant problems provided that some care is taken over the thermal protection system for the tanks. Since the HOPE destination is in the outer solar system, maintaining low temperatures is less of a problem than in Earth orbit. High-efficiency cryocoolers can be used to balance the natural heat leakage to the hydrogen and maintain the liquid state. Storage of the relatively small quantity of deuterium in liquid form is actually somewhat easier than normal hydrogen because the boiling point is several degrees higher. For reference, note that the entire system of plasma guns, all 48 of them, consumes ≈ 50 mg of deuterium and 850 mg of hydrogen per fusion pulse.

The plasma guns can be designed to operate using gas, liquid, or even solid propellants. Given their location around the MTF nozzle, an area of elevated temperature, gaseous feed is clearly the favored option. An overall schematic of the storage and supply system is given in figure 41.

Note that the four D-T tanks are each shaded slightly differently in the diagram. This is to denote a slight variation in the proportions of the two gasses at loading. The tank intended for immediate use is loaded in a straight 50–50 molar mixture. The tanks intended for use later in the mission are loaded slightly tritium-rich. This is to offset the natural radioactive decay of tritium to helium-3; therefore, the later the tank's intended use, the more tritium-rich is its initial load.

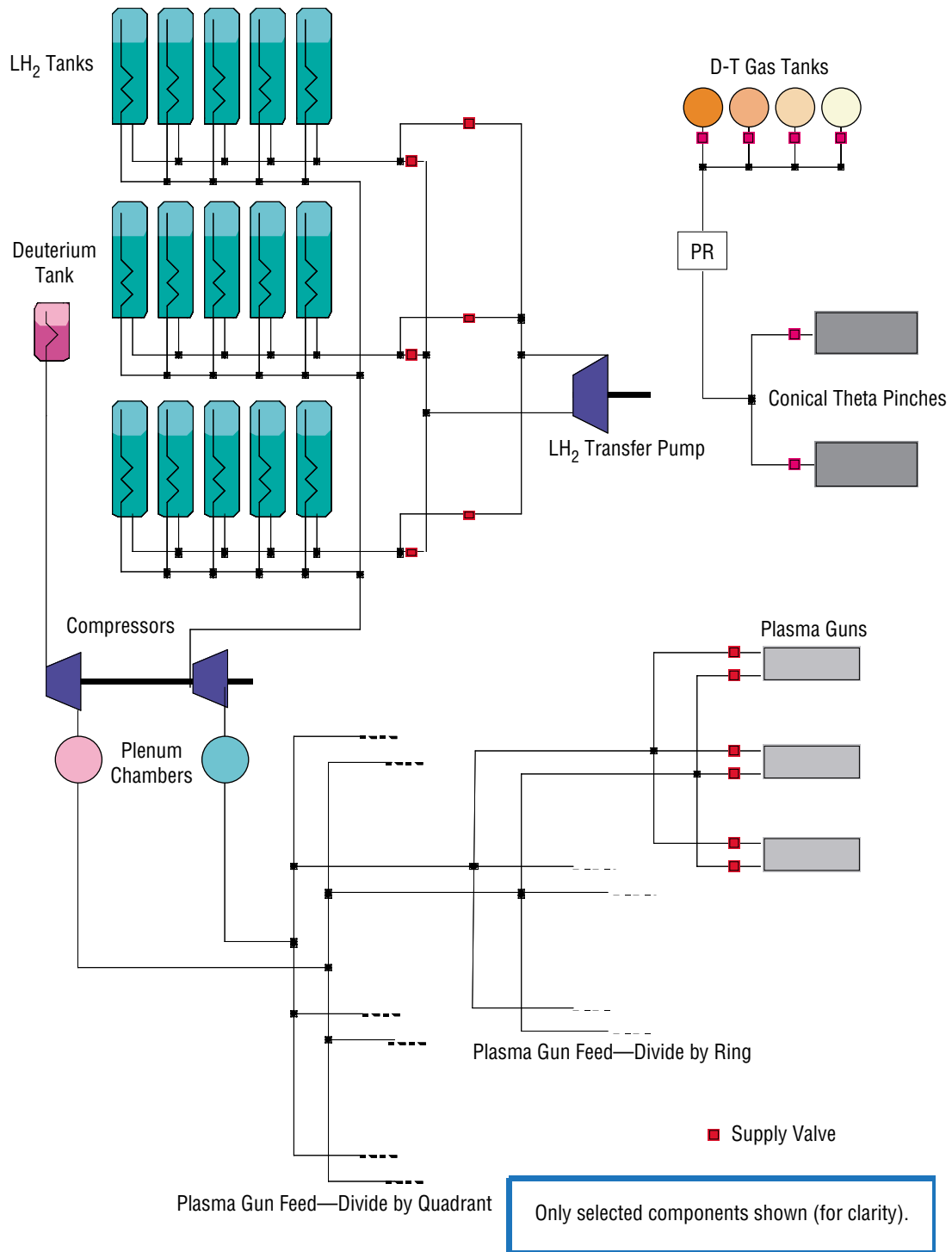


Figure 41. Propellant storage and supply system.

Also, note the use of gas compressors and plenum chambers. The compressors are needed to overcome line losses on the way to the plasma guns. The plenum chambers are to ensure reasonably constant gun inlet conditions.

Provision is also made for the transfer of LH₂ between the various storage tanks in order to enable the control of the vehicle's center of mass.

2.5.9 Magnetized Target Fusion Mass Estimate

A high-level mass breakdown for the MTF system, excluding the propellant storage and supply systems, is given in table 9.

Table 9. MTF device mass summary.

Component	Mass (kg)	Notes
Plasma guns	2,219	48 plasma guns
Capacitors	6,657	Provide power to the 48 plasma guns
Target generator system	666	Two conical theta pinches
Nozzle structure	20,576	Splines and rings
Nozzle structure neutron shield	16,036	Neutron shielding for the nozzle splines and rings
Nozzle coils and coil neutron shields	33,400	Seed and main coils, together with associated neutron shielding
SMES	3,000	Stores electrical energy (required to generate the seed magnetic field) between pulses of the MTF system
Recharging circuit	1,664	Circuit which routes power between the coils and the SMES
Vehicle neutron shield	37,000	Water tank located above nozzle apex to shield the vehicle from fusion neutrons
Power cables	115	
Total	121,333	

These mass values apply to a device pulsing at a frequency of 20 Hz and with a mean jet power of 2.038 GW.

2.5.10 Magnetized Target Fusion Performance Summary

A simple performance summary for the MTF system is given in table 10.

Table 10. MTF device performance summary.

Parameter	Nominal Value
MTF mean jet power	2.038 GW
MTF pulse repetition frequency	20 Hz
I_{sp}	70,485 s
Mean thrust	5,798 N
Total mean heat input rate to MTF device due to intercepted 14.1 MeV neutrons	317.7 MW
Total mean heat input rate to MTF device due to intercepted 2.45 MeV neutrons	44.4 MW
Assumed waste heat rate generated by secondaries per neutron capture	1 MeV
Heat transfer rate from plasma to structure (primarily Bremsstrahlung)	85 MW
Rate of heat generation due to nozzle components (plasma guns, target generators, ohmic heating of coils)	45.8 MW

2.5.11 Deuterium-Helium-3 Magnetized Target Fusion

Thus far, all discussion has centered on an MTF device using a D-T trigger to initiate fusion and an all-deuterium inner liner to provide the main fusion energy yield. There is an alternate and higher performing fusion fuel combination, which should be available in the future. The trigger plasma would still consist of a 50–50 molar D-T plasma, but the plasma in the inner portion of the liner would no longer be pure deuterium; instead, a 50–50 molar mixture of deuterium and helium-3 would be used. Although this combination requires a higher ignition temperature than the all-deuterium option, it is still achievable with the same D-T trigger. Once initiated, the D-He3 fusion reaction offers an improved level of energy release, compared to the D-D baseline, and a lower neutron flux. With an improved energy release and a larger proportion of the liberated energy appearing in the form of charged-particle kinetic energy, significant performance improvements will result. Charged-particle kinetic energy can be absorbed and redirected by the nozzle magnetic field, thus, adding useful impulse to the vehicle. By comparison, neutron kinetic energy places a significant mass burden on the vehicle due to the shielding requirement. Although the D-He3 reaction still does produce some neutrons, the number will be reduced compared with the all-deuterium inner-liner option.

The drawback of this advanced fuel option is the relative scarcity of helium-3. Although it can be produced by the decay of tritium, this technique is inherently limited by the scarcity of tritium, which must be produced by neutron bombardment within a nuclear reactor. Only trace amounts of helium-3 are available naturally on the Earth, but it is postulated that larger amounts might be available at significant depths below the surface. A plentiful supply exists in the lunar regolith, which accumulates helium-3 as a result of solar wind bombardment. Although, at present, this may seem a somewhat inaccessible deposit, it should be considered within the context of the cislunar infrastructure likely to be in place by

the time an MTF propulsion system is in operation. By that time, with MTF providing the means for human exploration of the outer solar system, thriving transport, manufacturing, and resource extraction infrastructure should be in place at the Earth's Lagrange points and on the lunar surface. The process of helium-3 extraction from lunar regolith has already been seriously studied with encouraging results.²⁴

Even more extensive sources of helium-3 are almost certainly available in the outer solar system. All of the gas giant planets appear to contain substantial quantities of the isotope. Although the ΔV 's associated with atmospheric flight within a gas giant are formidable, it is possible that mining operations may eventually be possible. The first MTF flights to the outer solar system might use deuterium; once appropriate infrastructure has been established, subsequent flights might be able to use helium-3.

2.5.12 Structural Members

From the start, a conflict between two opposing ground rules was apparent in the structural analysis. On one hand was the ubiquitous requirement of low mass, and on the other was the requirement for a high view factor for the fusion plasma. The high view factor required the structure to be widely spaced with thin cross sections aimed at the focus of the MTF. Conversely, the low mass criteria drove the design to a near continuous shell. In the end, the preference was given to the view factor. The chosen design met most of the view factor requirements, but incurred a mass penalty. It was clear that a substantial amount of further optimization on the design could be accomplished. The structural design presented here should be considered as a starting point with further refinements possible.

The structural design was analyzed using a spreadsheet comprised of equations from *Roark's Formulas for Stress and Strain* by Roark, Budynas, and Young and the *Aeronautics Structures Manual* from MSFC.^{25,26}

2.5.13 Additional Shielding

To obtain an approximate estimate of the shielding requirements for the MTF propulsion engine, the Monte Carlo transport code MCNP was used to size the neutron shield.²⁷ The magnitude and spectrum of the neutrons generated from the fusion process depended on the power level and the fuel type. MCNP has built in energy spectrums for D-T and D-D reactions. The base case was a 2.844-GW reactor fueled by D-T. For the D-T fuel mixture, the spectrum is a mixture of 55 percent D-T neutron reactions and 45 percent D-D reactions.

The MCNP representation of the neutron shield geometry is shown in figure 42.

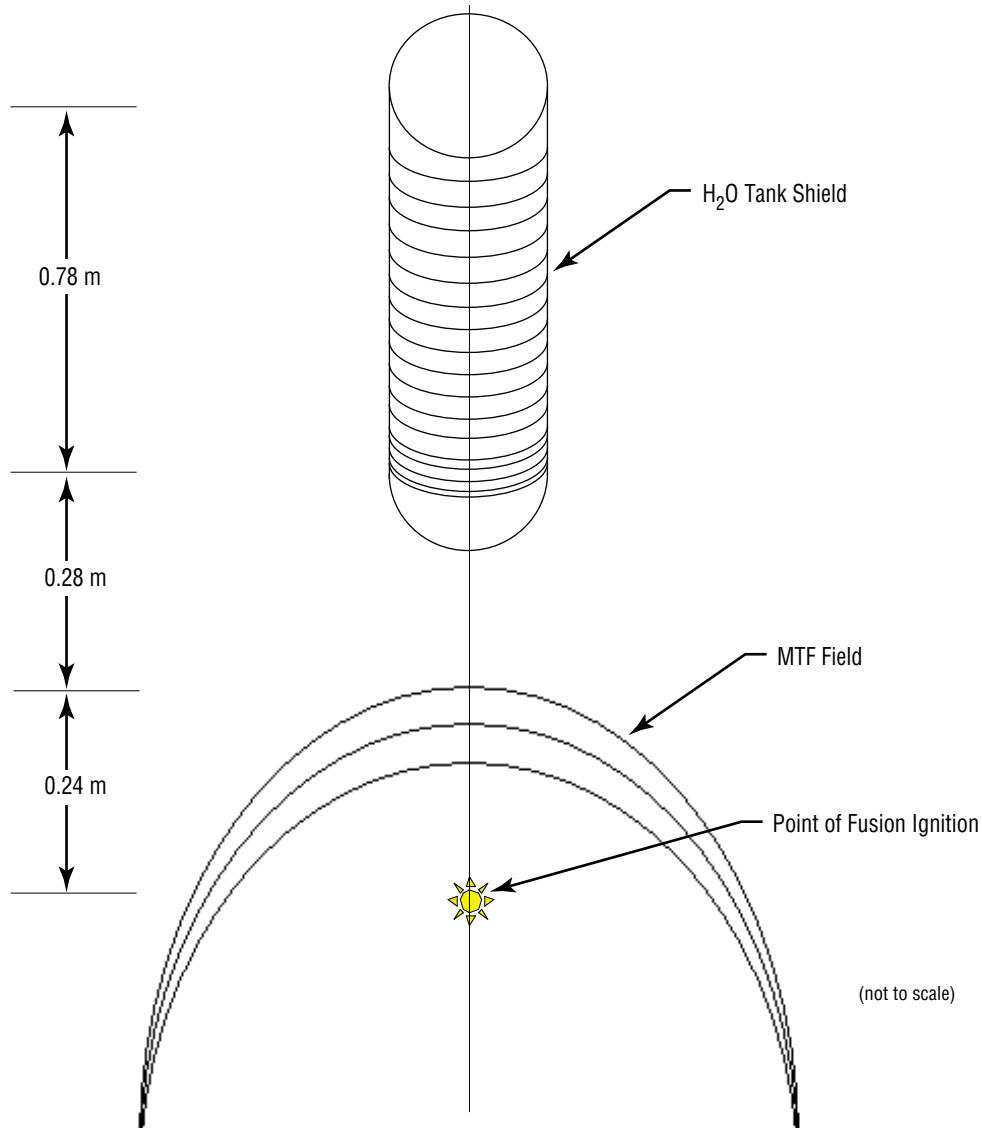


Figure 42. MCNP representation of neutron shield geometry.

Note that for these preliminary scoping calculations, only the shielding requirements for neutrons were calculated. The energy and magnitude of the photons are much less than for the neutrons, hence any additional shielding requirements would be very small. Additionally, gamma production from neutron capture in the structural materials will need further investigation. With appropriate material selections, this additional source of gamma radiation should be easily manageable.

The dimensions of the shield used for preliminary design purposes are given below. The shield was modeled as a cylindrical tank of water directly above the MTF nozzle. The thickness (height) of the tank was varied until the neutron dose to the crew from the MTF reactor was <5 rem/yr. The shape of the tank was modified to fit within the support truss of the vehicle.

2.5.14 Engine Layout

The major components of the MTF engine are the structural members, coils, plasma guns, coolant lines, power cables, and propellant lines. The location of the coils and plasma guns is determined by the physics of the engine, and the structure is designed to accommodate the locations. The propellant lines, power cables, and coolant lines are located on the outer side of the structural members so that the structure provides shielding. The physics of the engine require the structure to be as open as possible to maximize the view from within the engine to the outside (fig. 43).

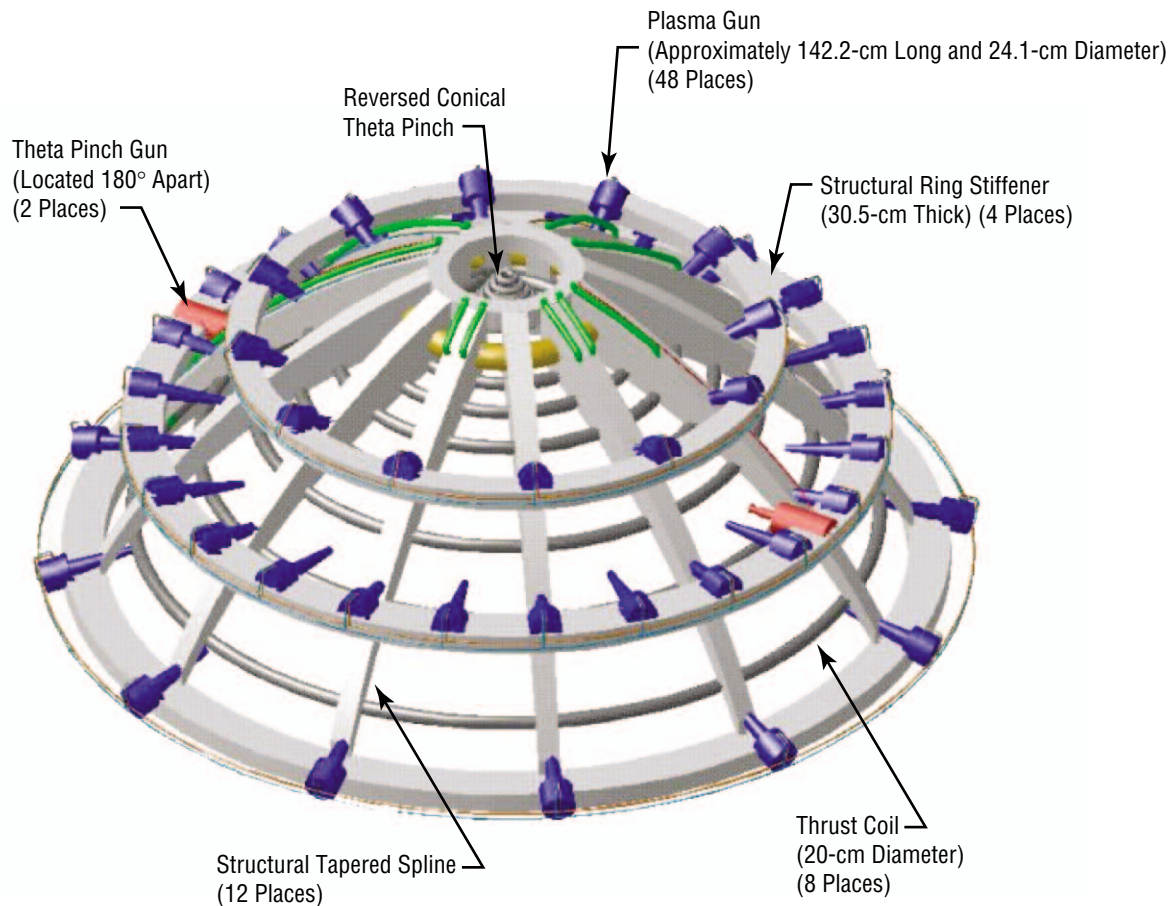


Figure 43. MTF engine configuration (iso view).

The size and shape of the MTF engine are determined by the layout of the coils and plasma guns, which can be seen in figures 44 and 45.

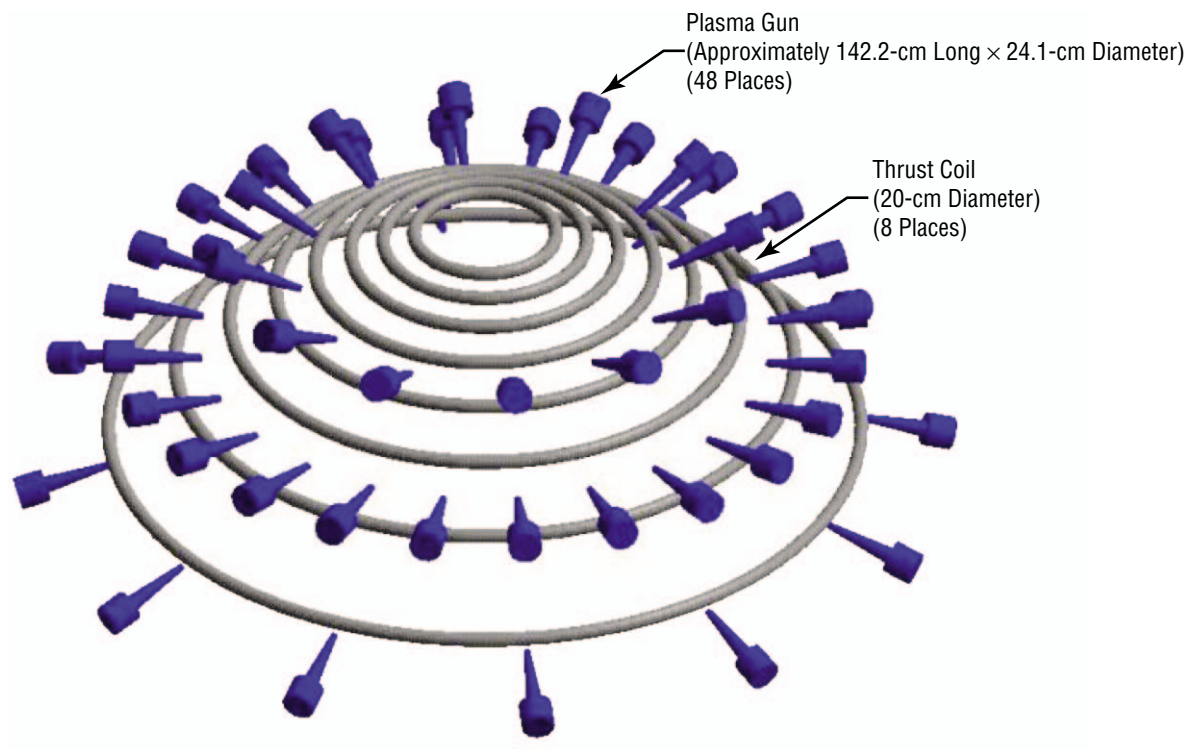


Figure 44. MTF engine coils and plasma guns (detail).

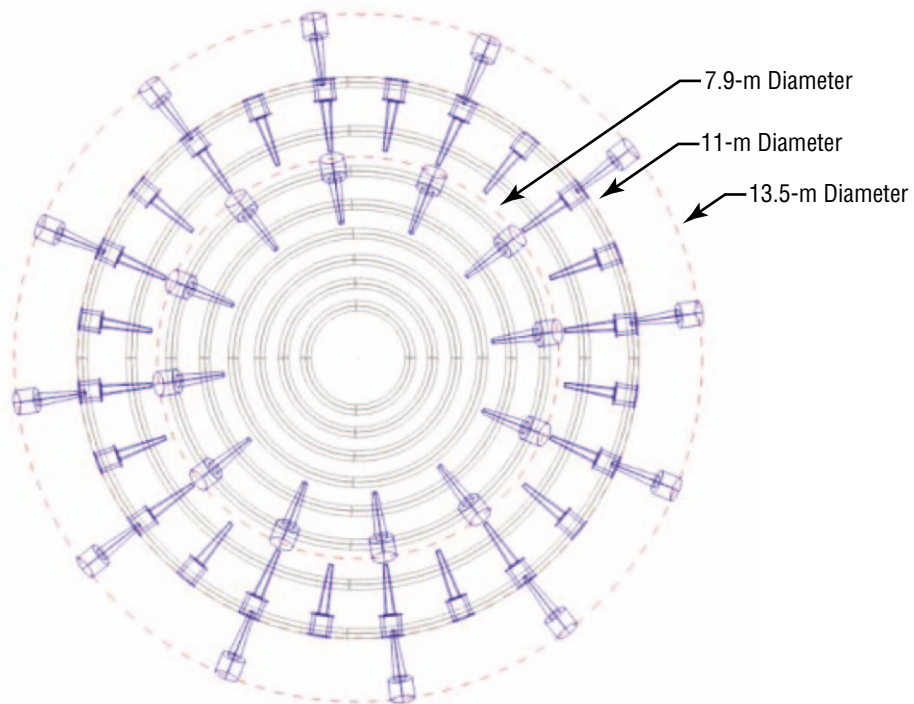


Figure 45. MTF engine coils and plasma guns locations (top view).

The MTF engine is ≈ 13 m in diameter and 5.2 m in height (fig. 46).

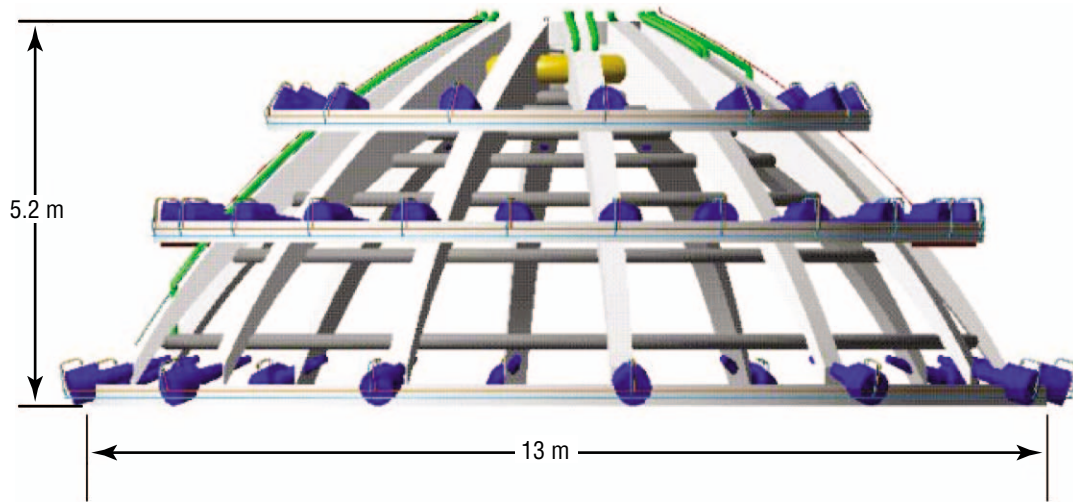


Figure 46. MTF engine overall dimensions (front view).

The top view of the MTF engine is shown in figure 47.

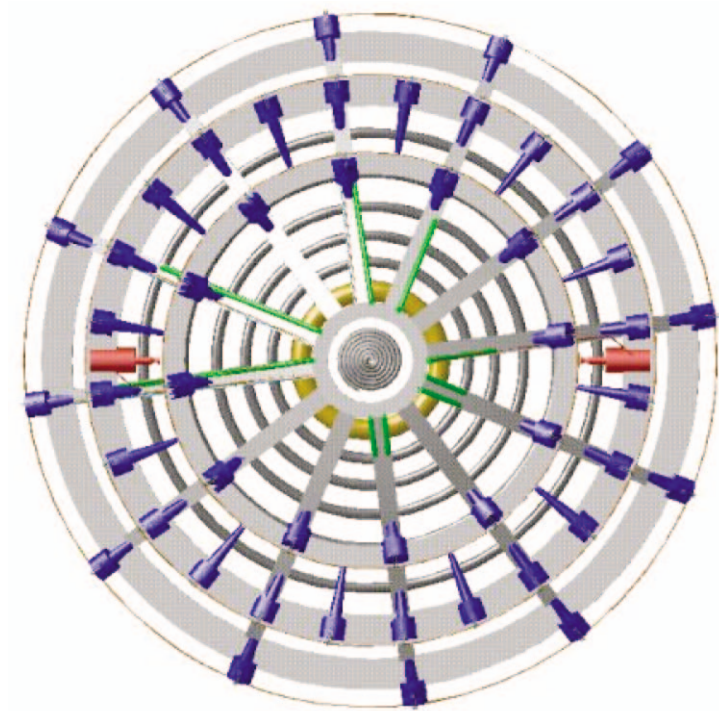


Figure 47. MTF engine configuration (top view).

2.6 Vehicle Design

2.6.1 Integration of Disciplines

A significant amount of interaction took place between the various disciplines during the design process. Therefore, vehicle design becomes an iterative process with substantial data transfer between the various disciplines. The vehicle design process is illustrated in figure 48. Engineers at LaRC defined vehicle payloads, such as the Transhab, lander, surface habitat, and ISRU plant. After a few initial iterations the mass and envelope volume remained relatively constant. Next, using results from previous iterations and total mission times as a guide, the project lead would estimate a total mission time and a total required initial mass at L1 (IML1) for the vehicle. The trajectory analyst would take those data and calculate optimal planetocentric and heliocentric trajectories that met the total mission requirement. In calculating these trajectories, the analyst assumed propulsion system performance parameters, such as jet power, I_{sp} , and specific power. These assumed values were passed to the propulsion analyst for verification. The two analysts iterated until convergence on the aforementioned performance parameters was achieved.

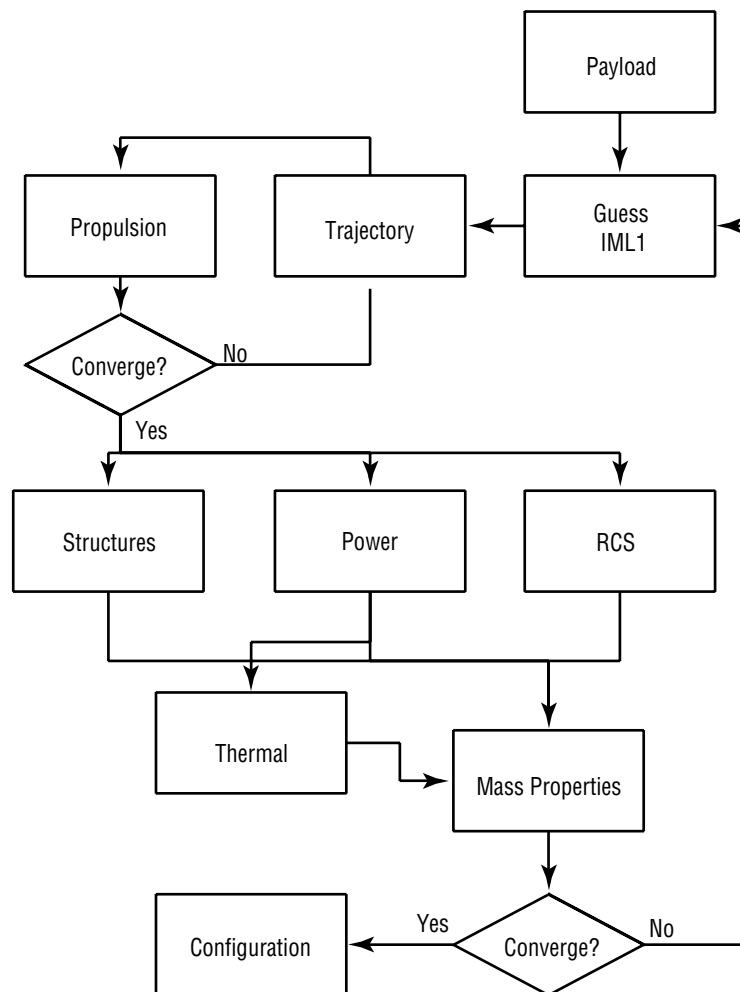


Figure 48. RASC HOPE design process data flow.

At this point, many of the required analyses were performed in parallel. The trajectory analyst provided the RCS analyst with a vehicle mass timeline for the duration of the mission. This ensured that the RCS system could be designed to meet pointing and docking requirements for the mission. The trajectory analyst was also required to provide propellant mass requirements to the structural analyst. The propulsion analyst also outlined major propulsive loads. The structural analyst then determined tank requirements and structural truss masses. The power analyst ensured that the power system was able to start the propulsion system and meet other power demands from the payloads and the other subsystems. The thermal analyst received inputs from the propulsion and power systems and from the payloads, which were used to determine radiator areas and masses. The thermal analyst also calculated cryocooler masses and areas based on the tankage requirements that were obtained from the structural analysis. Finally, the mass properties analyst received inputs concerning all of the subsystems and combined them to produce a resultant IML1 and mass schedule. If these values did not agree with the various assumptions, the project lead assumed another IML1 and another iteration was performed. If the values agreed within a reasonable error, all of the above data were given to the configuration analyst for layout and CAD rendering. This process is schematically illustrated in figure 48.

2.6.2 Options Considered

MSFC's original task was to consider only nuclear fusion propulsion techniques for the HOPE mission. The initial three techniques selected for study follow: (1) The Spherical Torus concept, developed by Williams et al.;²⁸ (2) the MTF concept, developed by Thio et al.;⁵ and (3) the vehicle for interplanetary space transport applications (VISTA) concept, developed by Orth et al.²⁹ These concepts cover the range of fusion techniques, from continuous magnetic confinement to pulsed inertial confinement. Fusion concepts employing antimatter were not considered since their level of development seemed too low to support a vehicle conceptual design.

One of the major ground rules for this study was that the crew could only be exposed to microgravity for a cumulative total time of 1 yr. In this context, microgravity was defined as being any acceleration less than one-eighth of standard Earth gravity. None of the candidate propulsion systems are capable of accelerating the vehicle sufficiently to provide this level of apparent gravity, so any missions lasting longer than 1 yr would automatically require a separate artificial gravity system. All of the fusion-propelled concepts were developed using a total mission time of 1 yr and a crew stay time on the target planet of 1 mo. Since the surface gravity on Callisto is one-eighth of standard Earth gravity, time spent on the surface did not contribute towards the 1-yr microgravity total. All of the concepts above are capable of performing such a mission, but in some cases, the initial vehicle mass was extremely high.

Unfortunately, although there is an excellent and well-documented design study on the Spherical Torus concept available in the literature,²⁸ information on scaling the device is not readily obtainable. For the VISTA concept, information in the literature is less abundant, and once again, there are no scaling data. The lack of scaling data for these two concepts meant that the MSFC design team had to use the point designs taken directly from the literature without any adjustments in order to complete preliminary vehicle designs to the selected destination. Unfortunately, these vehicle designs were noncompetitive, in part due to the fact that the engine designs used had been optimized for somewhat different missions. As a result, MTF emerged from this preliminary process as the most promising propulsion concept.

Several different options for MTF were considered. An MTF system based on the D-D reaction was adopted as the baseline, but an alternate system based on the D-He3 reaction was also retained as an advanced option. The fission concepts developed by the other Centers required a 180-day crew time on Callisto. The stay time was defined by the need to wait for Jupiter and Earth to come back into optimum alignment and reduce the total vehicle ΔV requirement. Therefore, the HOPE study lead requested that the MSFC team consider a fusion option with a 180-day stay time to facilitate comparison with results produced by the other (nonfusion) teams. A parametric analysis of total mission time showed that a time of 1.75 yr substantially reduced mission ΔV requirements. A 1-yr mission required the vehicle to fly retrograde on both outbound and inbound legs. In contrast, the 1.75-yr mission avoided this problem and, although nearly doubling trip time, reduced the acceleration requirements. Of course, the longer trip time necessitated incorporation of an artificial gravity system into the vehicle design, but the associated mass penalty was minor compared to the gains achieved.

From this wide range of cases, three following MTF options were selected for presentation: (1) MTF D-D 30-day stay, (2) MTF D-D 180-day stay, and (3) MTF D-He3 180-day stay. Results are given in table 11.

Table 11. Vehicle mass and power breakdown (MTF options).

		D-D 30-Day Stay		D-D 180-Day Stay		D-He3 180-Day Stay	
System	Subsystem	Mass (kg)	Power (kW)	Mass (kg)	Power (kW)	Mass (kg)	Power (kW)
Payload		163,933	30	163,933	30	163,933	30
	Crew quarters (Transhab)	40,000		40,000		40,000	
	Consumables	3,933		3,933		3,933	
	Small transport	40,000		40,000		40,000	
	Surface habitat	40,000		40,000		40,000	
	ISRU plant	40,000		40,000		40,000	
Structural		26,610		34,785		32,060	
	Structural boom	10,260		10,260		10,260	
	Forward truss	3,420	3,420	3,420		3,420	
	Aft truss	6,840	6,840	6,840		6,840	
	Main propellant tanks	16,350		24,525		21,800	
RCS		12,946	1.7	12,989	1.7	12,976	1.7
	Forward thruster pod	82		82		82	
	Aft thruster pod	82		82		82	
	Tanks	9,893	1.7	9,936	1.7	9,923	1.7
	Lox tank	1,847		1,847		1,847	
	Lox cryo	50	0.1	50	0.1	6,966	0.1
	LH ₂ tanks	6,966		6,966	1.6	50	1.6
	LH ₂ cryo	352	1.6	352		352	
	Resident propellant	678		721		708	
Miscellaneous hardware		2,889		2,889		2,889	
	Filters, sensors	2,202		2,202		2,202	
	Accumulator tanks	687		687		687	
Thermal		51,391	112.8	76,864	188.8	51,306	188.8
	Propellant cryocooler	7,224	53.2	10,836	129.2	9,632	129.2
	Radiator	3,180		4,770		4,240	
	Cooler	645	53.2	968	129.2	860	129.2
	Cooler controller	903		1,355		1,204	
	Insulation	2,496		3,744		3,328	
	ECLSS/avionics radiators	1,302		1,302		1,302	
	Radiator	1,302		1,302		1,302	
	Pumps	0		0		0	
	Piping	0		0		0	
Medium-temperature radiators		22,340	9.9	29,002	9.9	25,348	9.9
	Radiator	4,615		8,769		6,491	
	Pumps	1,020	9.9	1,938	9.9	1,434	9.9
	Tanks/HX	851		1,616		1,196	
	Fluid	916		1,741		1,289	
	Piping	14,938		14,938		14,938	

Table 11. Vehicle mass and power breakdown (MTF options) (Continued).

		D-D 30-Day Stay		D-D 180-Day Stay		D-He3 180-Day Stay	
System	Subsystem	Mass (kg)	Power (kW)	Mass (kg)	Power (kW)	Mass (kg)	Power (kW)
	High-temperature radiators	20,525	49.7	35,724	49.7	15,024	49.7
	Radiator	10,517		19,993		7,087	
	Pumps	2,324	49.7	4,418	49.7	1,566	49.7
	Tanks/HX	1,938		3,685		1,306	
	Fluid	2,088		3,970		1,407	
	Piping	3,658		3,658		3,658	
Power		17,370		17,370		17,370	
	Reactor	1,810		1,810		1,810	
	Power conversion	1,270		1,270		1,210	
	Shield	10,000		10,000		10,000	
	Turbine coolant loop	96		96		96	
	Electrical equipment	546		546		546	
	Primary loop	680		680		680	
	Main heat rejection loop	1,575		1,575		1,575	
	Alternator coolant loop	263		263		263	
	Electronics cooling loop	240		240		240	
	Structure	890		890		890	
Main propulsion		116,021		121,333		118,400	
	Capacitors	3,502		6,657		4,915	
	Plasma guns	1,167		2,219		1,638	
	Target generator	350		666		491	
	Magnetic nozzle	20,576		20,576		20,576	
	Seed coil and shielding	35,000		35,000		35,000	
	Power cables	2,000		2,000		2,000	
	Recharging circuit	875		1,664		1,229	
	Neutron shields	12,551		12,551		12,551	
	Energy storage	3,000		3,000		3,000	
	H ₂ O tanks	37,000		37,000		37,000	
Communications		275	0.2	275	0.2	275	0.2
Mass margin		116,564		128,265		118,896	
Total dry mass		505,110	144.7	555,814	220.7	515,216	220.7
	Main propulsion propellant	106,000		165,000		142,000	
	RCS propellant	34,063		35,348		34,676	
Gross IML1		645,173		756,162		691,892	

Near the end of the study, MSFC also conducted some analysis of nonfusion-propelled vehicle concepts. Several technologies that appear to increase performance of the nuclear-fission electric propulsion options were considered. The baseline nuclear electric option for these studies was a solid-core nuclear engine for rocket vehicle application-style reactor with a Brayton power conversion system and an MPD thruster assembly. MSFC investigated an alternate option in which the reactor and power conversion system were replaced by an MSR and LMR power conversion system. Additionally, MSFC investigated a system that replaced the Brayton cycle with an MHD power conversion system. Unlike the baseline MTF case, these concepts all required a 5-yr mission time and split mission profile; i.e., separate crew and cargo vehicles. The results are shown in tables 12 and 13.

Table 12. Vehicle mass and power breakdown (MSR–LMR–MPD option).

		Piloted Vehicle		Cargo Vehicle	
System	Subsystem	Mass (kg)	Power (kW)	Mass (kg)	Power (kW)
Payload		57,885	30	120,000	
	Crew quarters (Transhab)	40,000		0	
	Consumables	17,885		0	
	Small transport	0		40,000	
	Surface habitat	0		40,000	
	ISRU plant	0		40,000	
Structural		101,955		33,515	
	Structural boom	17,480		14,440	
	Forward truss	3,420		3,420	
	Aft truss	14,060		11,020	
	Main propellant tanks	84,475		19,075	
RCS		12,990	1.7	4,741	1.7
	Forward thruster pod	102		82	
	Aft thruster pod	102		82	
	Tanks	9,850	1.7	1,689	1.7
	Lox tank	1,847		402	
	Lox cryo	50	0.1	50	0.1
	LH ₂ tanks	6,966		797	1.6
	LH ₂ cryo	352	1.6	352	
	Resident propellant	722		88	
	Miscellaneous hardware	2,849		2,888	
	Filters, sensors	2,162		2,201	
	Accumulator tanks	687		687	
Thermal		49,966	494.7	15,180	110.5
	Propellant cryocooler	37,324	444	8,428	100
	Radiator	16,430		3,710	
	Cooler	3,333	444	753	100
	Cooler controller	4,666		1,054	
	Insulation	12,896		2,912	
	ECLSS/avionics radiators	1,302		1,302	
	Radiator	1,302		1,302	
	Pumps	0		0	
	Piping	0		0	
	Medium-temperature radiators	1,847	1	776	0.5
	Radiator	1,847		776	
	Pumps	0	1	0	0.5
	Tanks/HX	0		0	
	Fluid	0		0	
	Piping	0		0	

Table 12. Vehicle mass and power breakdown (MSR–LMR–MPD option) (Continued).

		Piloted Vehicle		Cargo Vehicle	
System	Subsystem	Mass (kg)	Power (kW)	Mass (kg)	Power (kW)
	High-temperature radiators	9,493	49.7	4,675	10
	Radiator	9,493		4,675	
	Pumps	0	49.7	0	10
	Tanks/HX	0		0	
	Fluid	0		0	
	Piping	0		0	
Power		72,149		37,157	
	Reactor	29,855		10,478	
	Power conversion	22,570		12,792	
	Shield	14,724		8,887	
	Turbine coolant loop	5,000		5,000	
Main propulsion		58,596		17,794	
	MPD Thrusters	12,346		2,627	
	PPUs	46,250		15,167	
Communications		275	0.2	275	0.2
Mass margin		106,145		68,599	
Total dry mass		459,961	526.6	297,260	112.4
	Main propulsion propellant	577,000		125,000	
	RCS propellant	35,375		4,322	
Gross IML1		1,072,336		426,582	

Table 13. Vehicle mass and power breakdown (SCR–MHD–MPD option).

		Piloted Vehicle		Cargo Vehicle	
System	Subsystem	Mass (kg)	Power (kW)	Mass (kg)	Power (kW)
Payload		57,843	30	120,000	
	Crew quarters (Transhab)	40,000		0	
	Consumables	17,843		0	
	Small transport	0		40,000	
	Surface habitat	0		40,000	
	ISRU plant	0		40,000	
Structural		85,605		30,790	
	Structural boom	17,480		14,440	
	Forward truss	3,420		3,420	
	Aft truss	14,060		11,020	
	Main propellant tanks	68,125		16,350	
RCS		13,031	1.7	12,903	1.7
	Forward thruster pod	102		102	
	Aft thruster pod	102		102	
	Tanks	9,978	1.7	1,990	1.7
	Lox tank	1,847		496	
	Lox cryo	50	0.1	50	0.1
	LH ₂ tanks	6,966		983	1.6
	LH ₂ cryo	352	1.6	352	
	Resident propellant	763		109	
	Miscellaneous hardware	2,849		2,848	
	Filters, sensors	2,202		2,202	
	Accumulator tanks	687		687	
Thermal		42,773	410.7	13,976	110.5
	Propellant cryocooler	30,100	360	7,224	100
	Radiator	13,250		3,180	
	Cooler	2,688	360	645	100
	Cooler controller	3,763		903	
	Insulation	10,400		2,496	
	ECLSS/avionics radiators	1,302		1,302	
	Radiator	1,302		1,302	
	Pumps	0		0	
	Piping	0		0	
	Medium-temperature radiators	1,698	1	776	0.5
	Radiator	1,698		776	
	Pumps	0	1	0	0.5
	Tanks/HX	0		0	
	Fluid	0		0	
	Piping	0		0	

Table 13. Vehicle mass and power breakdown (SCR–MHD–MPD option) (Continued).

		Piloted Vehicle		Cargo Vehicle	
System	Subsystem	Mass (kg)	Power (kW)	Mass (kg)	Power (kW)
	High-temperature radiators	9,673	49.7	4,674	10
	Radiator	9,673		4,674	
	Pumps	0	49.7	0	10
	Tanks/HX	0		0	
	Fluid	0		0	
	Piping	0		0	
Power		89,371		23,601	
	Reactor	23,088		6,190	
	Power conversion	3,152		845	
	Shield	42,726		11,095	
	Turbine coolant loop	2,227		597	
	Electrical equipment	18,178		4,874	
Main propulsion		13,134		2,627	
	MPD thrusters	3,502		2,627	
	PPUs	0		0	
Communications		275	0.2	275	0.2
Mass margin		90,610		58,893	
Total dry mass		392,643	144.7	255,204	112.4
	Main propulsion propellant	460,000		98,000	
	RCS propellant	37,409		5,330	
Gross IML1		890,052		358,354	

2.6.3 Fusion Mission Trajectories and Configurations

Each trajectory is optimized to give a maximum payload that is subject to a given set of constraints and independent variables. For the fusion-powered missions, the mission time was constrained to 650 days (excluding Earth escape and capture times). This time was selected though a series of compromises. The team wanted to analyze a short mission in order to demonstrate the capabilities of the MTF device; however, maximizing payload mass typically extends the trip time. Another important consideration was the spacecraft's distance from the Sun. Missions of 650 days or less generally maintained a distance of 1 AU or more from the Sun throughout the mission. Longer missions came closer to the Sun, resulting in greater radiation exposure for the crew. In an attempt to limit the harmful radiation dose from the Sun, shorten the duration, and maximize payload delivery, a 650-day mission was selected.

While the mission duration was fixed, the flight time for the outbound and return trajectory legs was not. The final optimized missions have return trajectory legs that are shorter than the outbound trajectories. This is to be expected because the vehicle thrust-to-weight ratio on return is much higher than at the start of the mission.

Note that VARITOP is allowed to select the power level and departure date that will optimize the mission performance. The final results for the three fusion-powered vehicles considered are given: D-D MTF 30-day stay—tables 14 and 15, figure 49; D-D MTF 180-day stay—tables 16 and 17, figures 50–52; and D-He3 MTF 180-day stay—tables 18 and 19, figures 53–55.

Table 14. D-D MTF 30-day stay summary information.

Activity	Specifics
Total mission duration	≈654 days
Outbound leg departs	4/22/2045
Flight to Callisto	≈331 days
Time in Callisto orbit	≈33 days
Total time thrusting	≈258 days
Returns without surface habitat, ISRU, and transport	120 t total
I_{sp}	70,400 s
Jet power	1.072 GW
Propulsion system specific mass	0.022 kg/kW
Initial acceleration	0.0005 g
Final acceleration	0.0007 g

Table 15. D-D MTF 30-day stay mission timeline.

Mission Timeline	Time (days)	Mass (t)
Depart L1 station	0	650
Thrust off	51	630
Thrust on	240	630
Arrive Callisto orbit	331	595
Depart Callisto orbit	365	475
Thrust off	440	445
Thrust on	614	445
Arrive L1 station	654	430

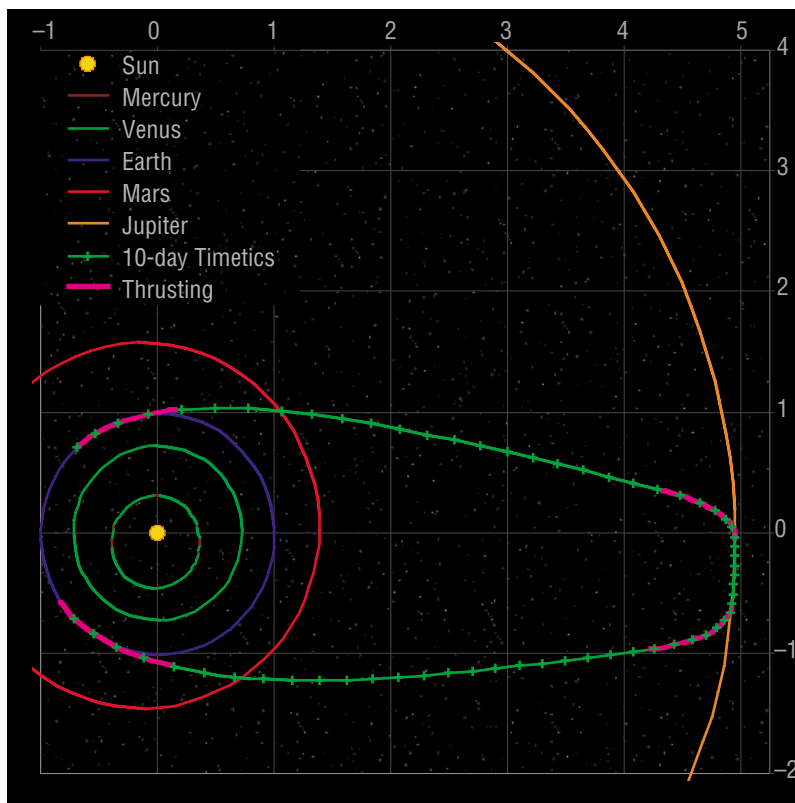


Figure 49. Trajectory graph for D-D MTF 30-day stay option.

Vehicle layouts for the 30-day stay option are shown in figures 22 and 23.

Table 16. D-D MTF 180-day stay summary information.

Activity	Specifics
Total mission duration	≈652 days
Outbound leg departs	4/26/2045
Flight to Callisto	≈249 days
Time in Callisto orbit	≈183 days
Total time thrusting	≈212 days
Returns without surface habitat, ISRU, and transport	120 t total
I_{sp}	70,400 s
Jet power	2.038 GW
Propulsion system specific mass	0.022 kg/kW
Initial acceleration	0.0008 g
Final acceleration	0.0013 g

Table 17. D-D MTF 180-day stay mission timeline.

Mission Timeline	Time (days)	Mass (t)
Depart L1 station	0	750
Thrust off	45	717
Thrust on	177	717
Arrive Callisto orbit	249	664
Depart Callisto orbit	432	544
Thrust off	492	499
Thrust on	617	499
Arrive L1 station	652	473

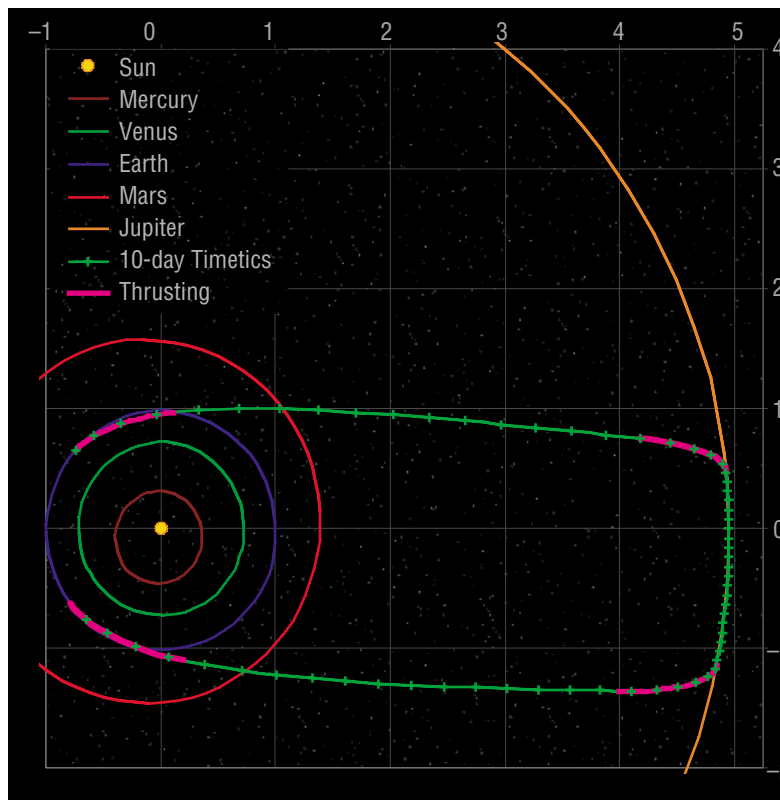


Figure 50. Trajectory graph for D-D MTF 180-day stay option.

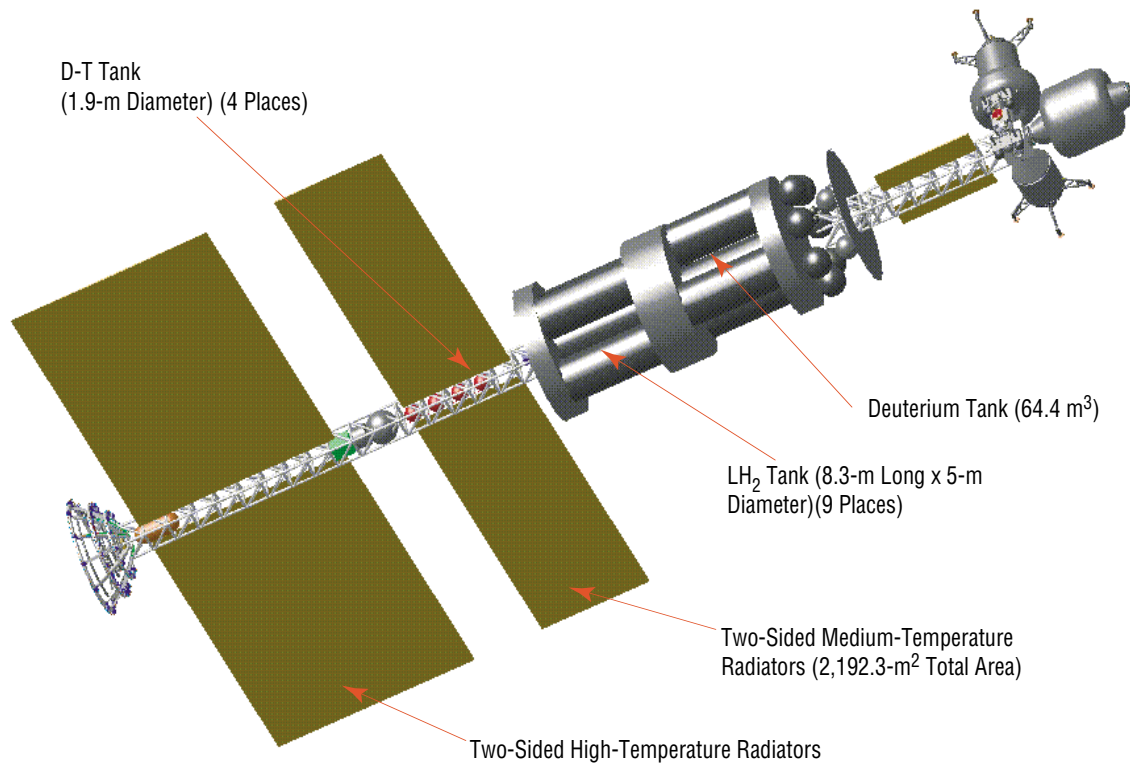


Figure 51. Vehicle layout for D-D MTF 180-day stay option.

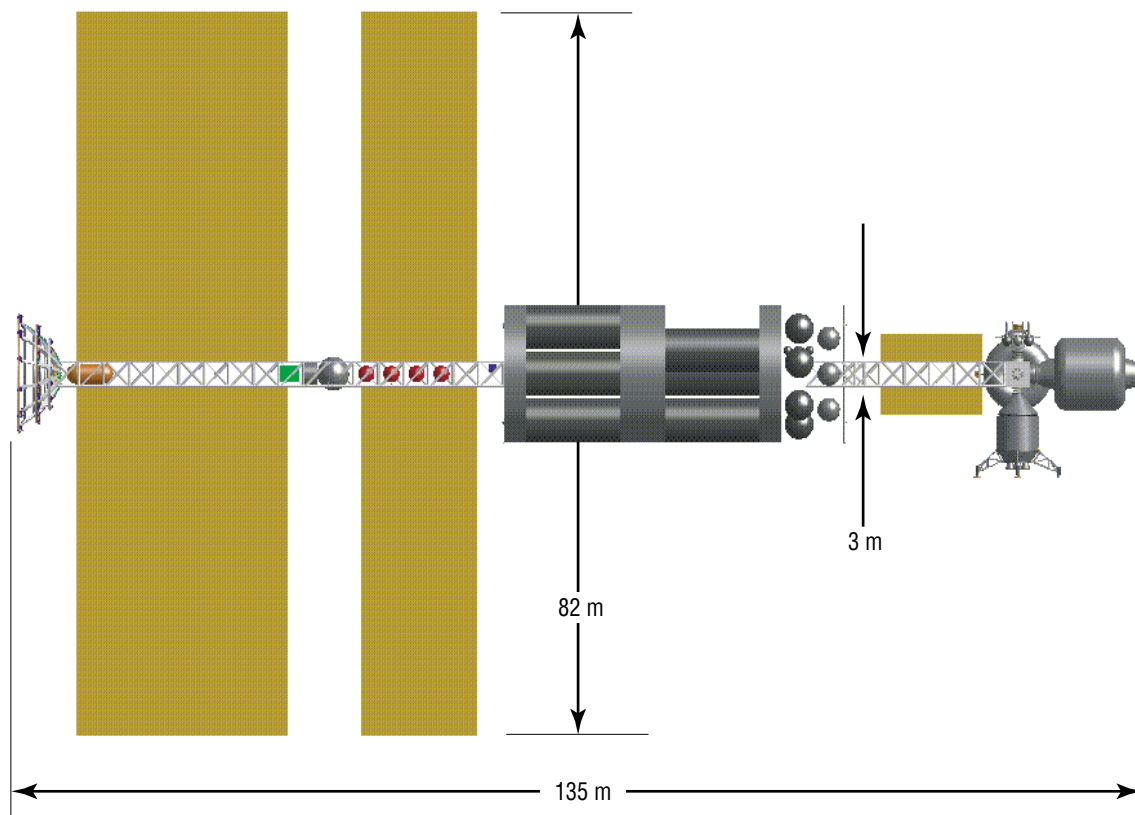


Figure 52. Vehicle dimensions for D-D MTF 180-day stay option.

Table 18. D-He3 MTF 180-day stay summary information.

Activity	Specifics
Total mission duration	≈652 days
Outbound leg departs	4/27/2045
Flight to Callisto	≈249 days
Time in Callisto orbit	≈183 days
Total time thrusting	≈215 days
Returns without surface habitat, ISRU, and transport	120 t total
I_{sp}	77,000 s
Jet power	2.071 GW
Propulsion system specific mass	0.0193 kg/kW
Initial acceleration	0.0008 g
Final acceleration	0.0013 g

Table 19. D-He3 MTF 180-day stay mission timeline.

Mission Timeline	Time (days)	Mass (t)
Depart L1 station	0	700
Thrust off	46	671
Thrust on	176	671
Arrive Callisto orbit	249	626
Depart Callisto orbit	432	506
Thrust off	493	468
Thrust on	616	468
Arrive L1 station	652	445

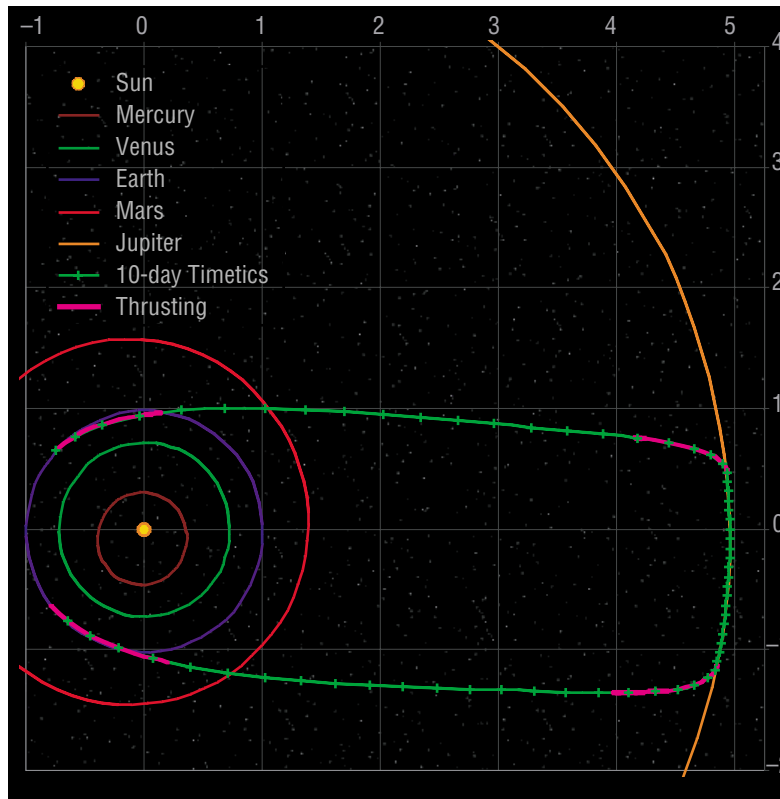


Figure 53. Trajectory graph for D-He3 MTF 180-day stay option.

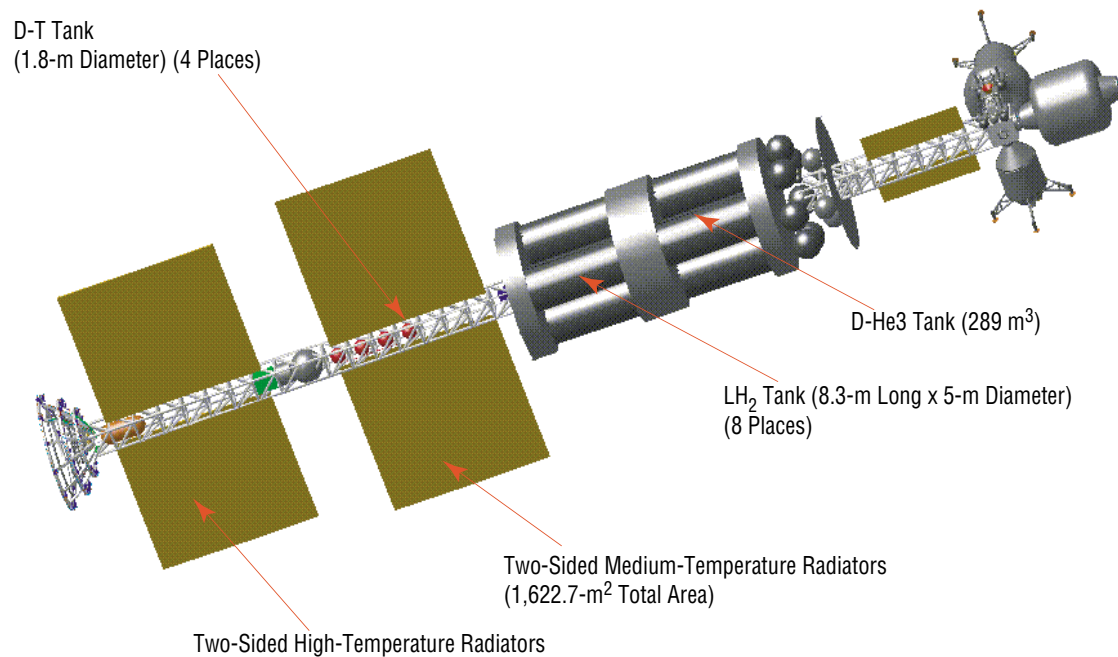


Figure 54. Vehicle layout for D-He3 MTF 180-day stay option.

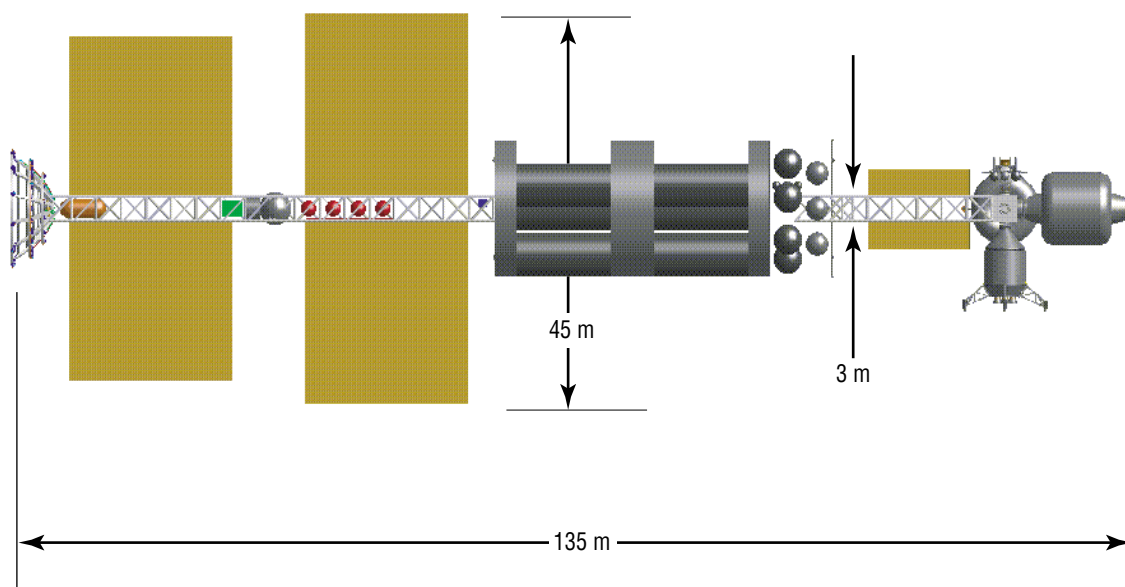


Figure 55. Vehicle dimensions for D-He3 MTF 180-day stay option.

2.6.4 Magnetoplasmadynamic Mission Trajectories and Configurations

MPD mission optimization is similar to that for the fusion missions. The time constraint in this case was modeled after the GRC MPD mission. This was done so that the effects of technology differences between the cases could be assessed. For these trajectories, VARITOP was able to approximate the Jupiter capture and escape spirals while the Earth and Callisto capture and escape spirals had to be approximated separately; i.e., external to the program. Both the altitude of the L1 point above the Earth and the vehicle thrust-to-weight ratio make VARITOP's approximation technique inappropriate for analysis of the Earth spiral maneuvers. In addition, VARITOP can only model spiral trajectories about the primary attractor in a system, which means that in the Jovian system, only spiral trajectories about Jupiter and not Callisto can be modeled. The final results for the two MPD vehicles considered are given in tables 20 and 21 and figures 56–60 for the MSR–LMR–MPD 120-day stay, and in tables 22 and 23 and figures 61–65 for the SCR–MHD–MPD 120-day stay.

Table 20. MSR–LMR–MPD 120-day stay summary information.

Activity	Specifics
Cargo mission:	
Total mission duration	≈1,120 days
Departs	9/2/2041
Payload delivered	120 t
Total power	11 MW
Jet power	7 MW
Propulsion system specific mass	5.36 kg/kW
I_{sp}	8,000 s
Piloted mission:	
Total mission duration	≈1,661 days
Outbound leg departs	11/19/2044
Flight to Callisto	≈832 days
Time in Callisto orbit	≈120 days
Total time thrusting	≈812 days
Returns with 13 t less consumables	
I_{sp}	8,000 s
Total power	37 MW
Jet power	24 MW
Propulsion system specific mass	5.36 kg/kW
Initial acceleration	0.0001 g
Final acceleration	0.0001 g

Table 21. MSR–LMR–MPD 120-day stay mission timeline.

Activity	Time (days)	Mass (t)
Cargo mission:		
Depart L1 station	0	456
Thrust off	329	390
Thrust on	861	390
Arrive Callisto orbit	1,120	337
Piloted mission:		
Depart L1 station	0	1,072
Thrust off	34	1,049
Thrust on	60	1,049
Thrust off	284	897
Thrust on	593	897
Arrive Callisto orbit	832	735
Depart Callisto orbit	952	722
Thrust off	1,145	591
Thrust on	1,540	591
Arrive L1 station	1,661	509

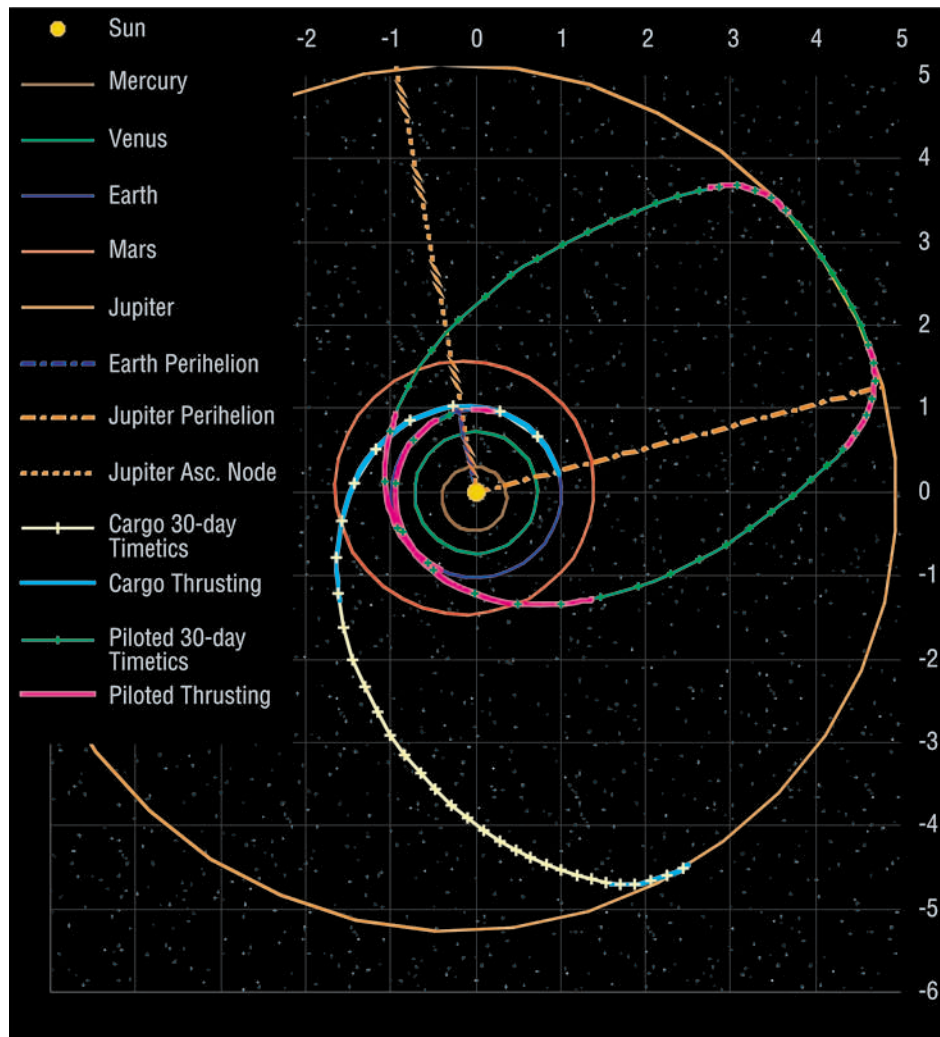


Figure 56. Trajectory graph for MSR-LMR-MPD 120-day stay option.

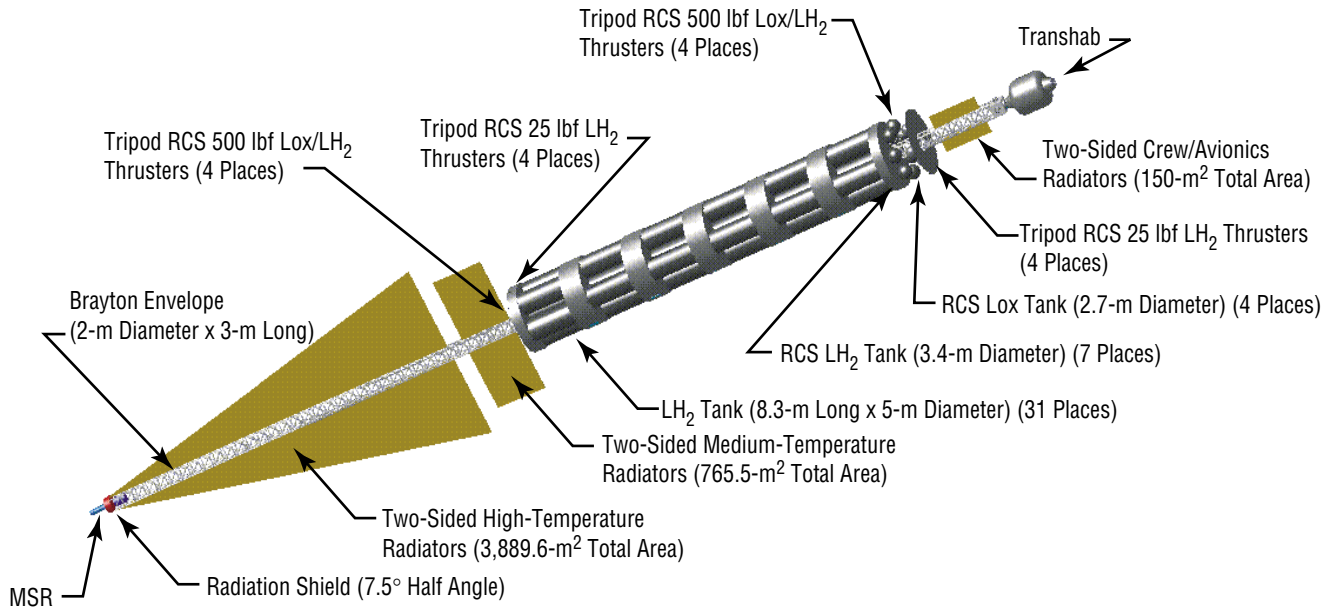


Figure 57. Piloted vehicle layout for MSR-LMR-MPD 120-day stay option.

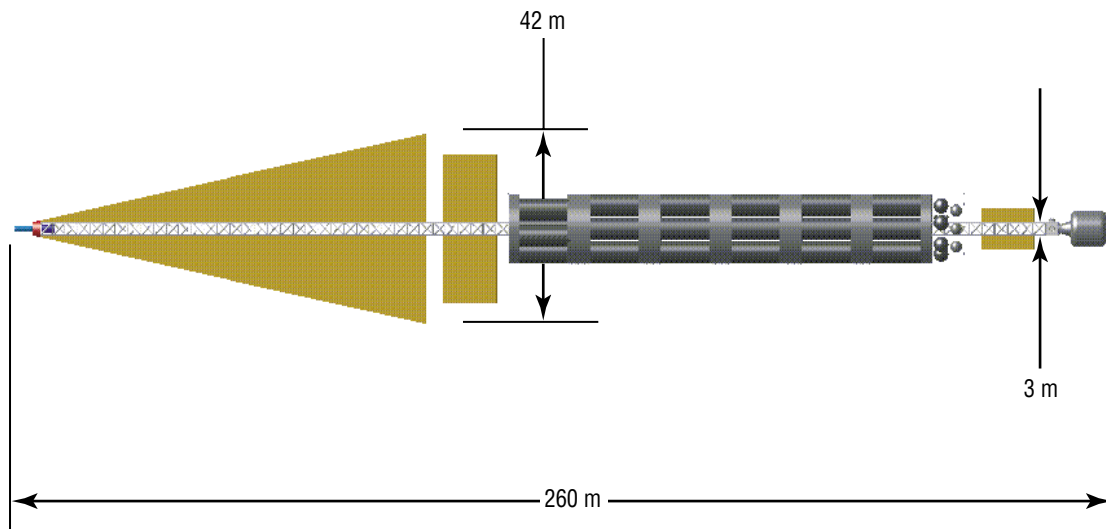


Figure 58. Piloted vehicle dimensions for MSR-LMR-MPD 120-day stay option (side view).

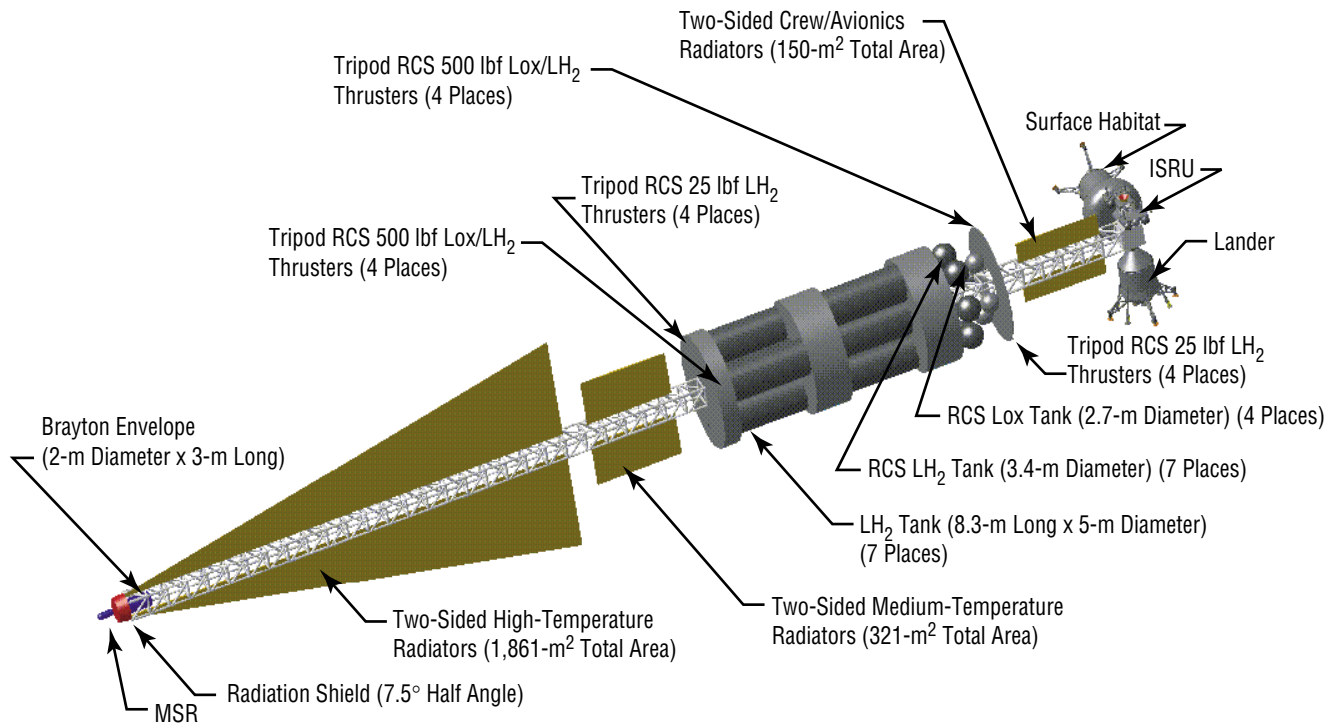


Figure 59. Cargo vehicle layout for MSR-LMR-MPD 120-day stay option.

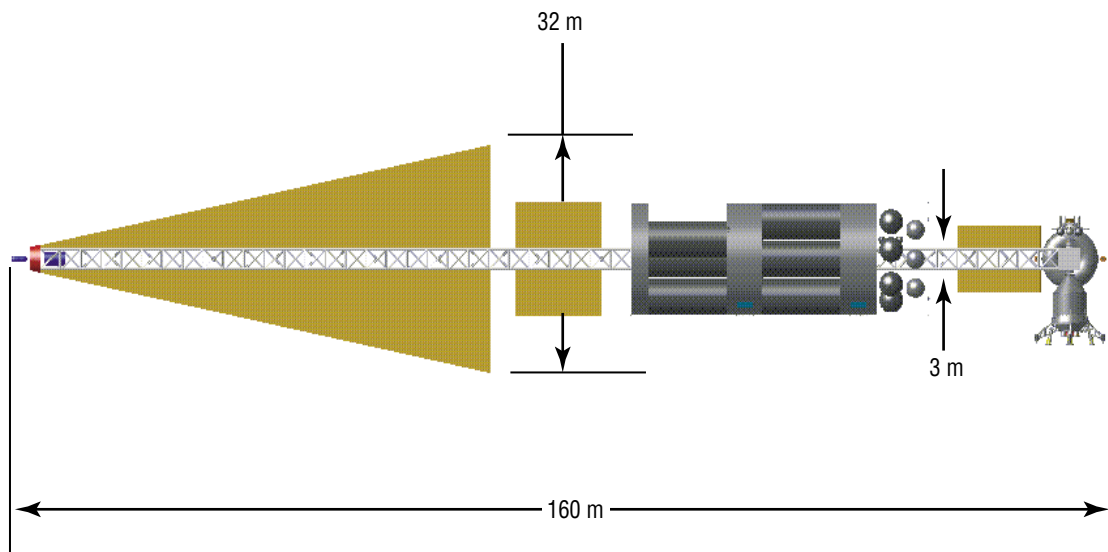


Figure 60. Cargo vehicle dimensions for MSR-LMR-MPD 120-day stay option (side view).

Table 22. SCR–MHD–MPD 120-day stay summary information.

Activity	Specifics
Cargo mission:	
Total mission duration	≈1,114 days
Departs	9/10/2041
Payload delivered	120 t
Total power	10 MW
Jet power	6 MW
Propulsion system specific mass	4.02 kg/kW
I_{sp}	8,000 s
Piloted mission:	
Total mission duration	≈1,658 days
Outbound leg departs	12/06/2044
Flight to Callisto	≈833 days
Time in Callisto orbit	≈122 days
Total time thrusting	≈693 days
Returns with 13 mt less consumables	
I_{sp}	8,000 s
Total power	34 MW
Jet power	22 MW
Propulsion system specific mass	4.02 kg/kW
Initial acceleration	0.0001 g
Final acceleration	0.0001 g

Table 23. SCR–MHD–MPD 120-day stay mission timeline.

Activity	Time (days)	Mass (t)
Cargo mission:		
Depart L1 station	0	380
Thrust off	300	328
Thrust on	878	328
Arrive Callisto orbit	1,114	283
Piloted mission:		
Depart L1 station	0	882
Thrust off	7	866
Thrust on	60	866
Thrust off	253	747
Thrust on	603	747
Arrive Callisto orbit	780	619
Depart Callisto orbit	955	604
Thrust off	1,126	498
Thrust on	1,548	498
Arrive L1 station	1,658	430

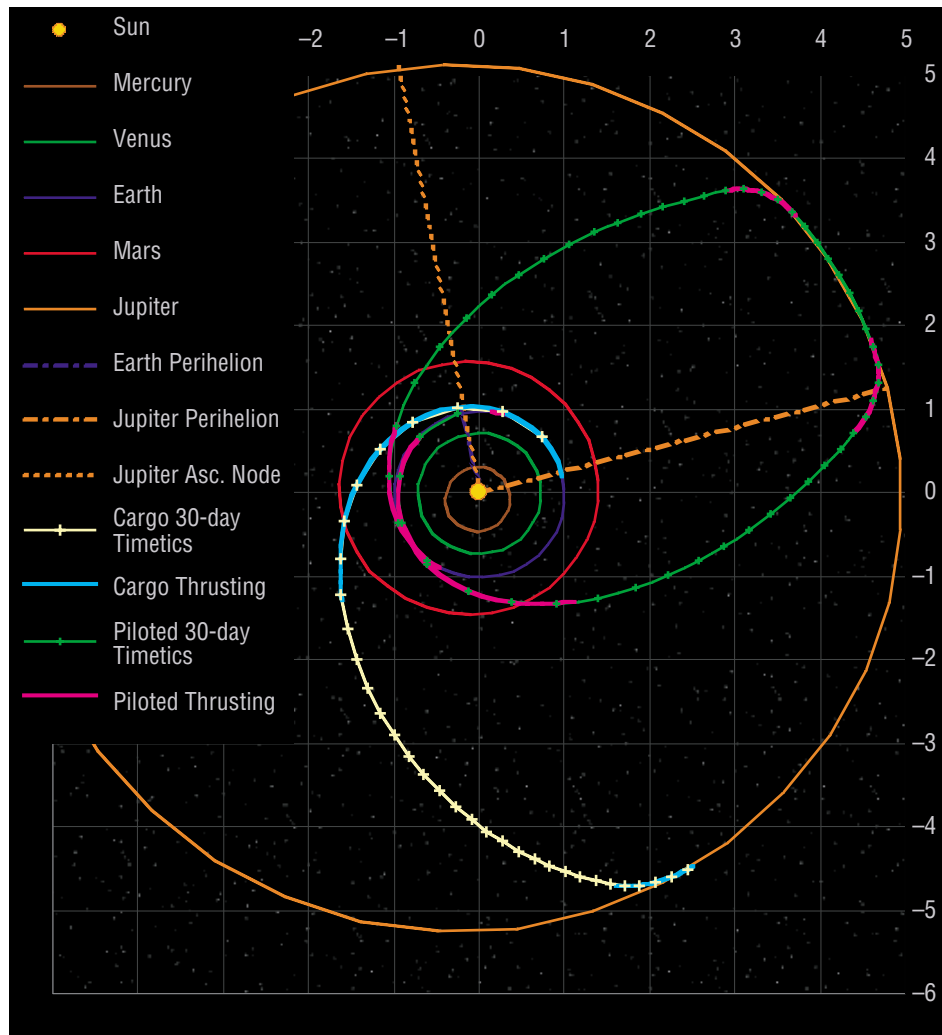


Figure 61. Trajectory graph for SCR-MHD-MPD 120-day stay option.

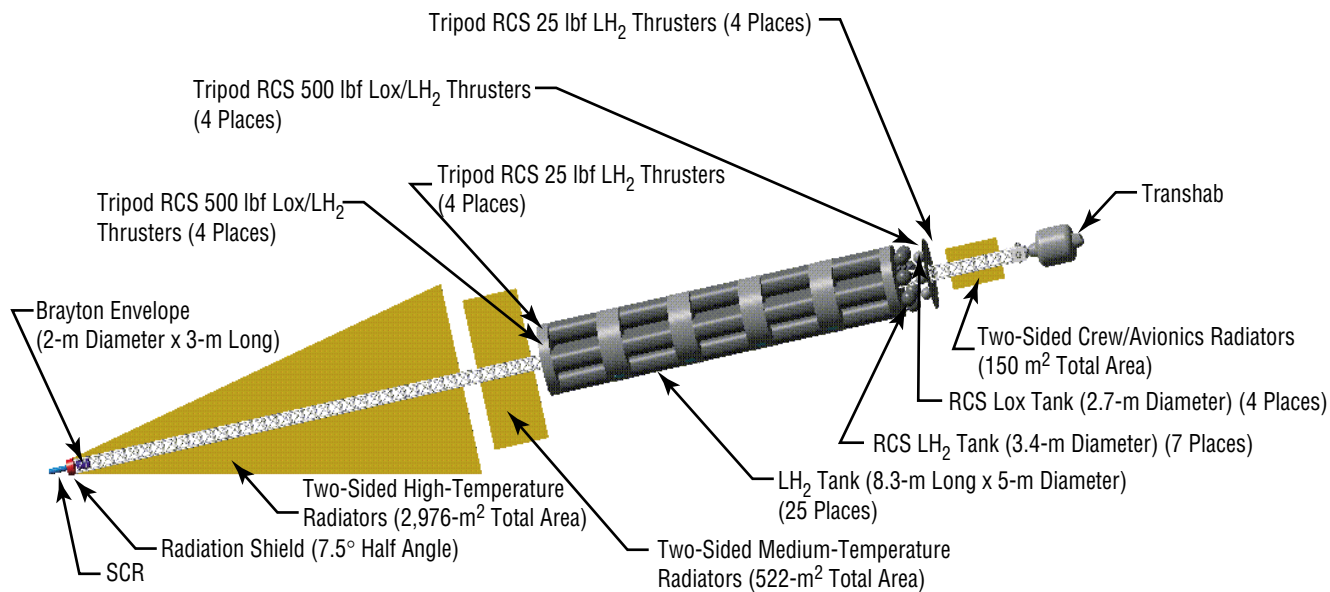


Figure 62. Piloted vehicle layout for SCR-MHD-MPD 120-day stay option.

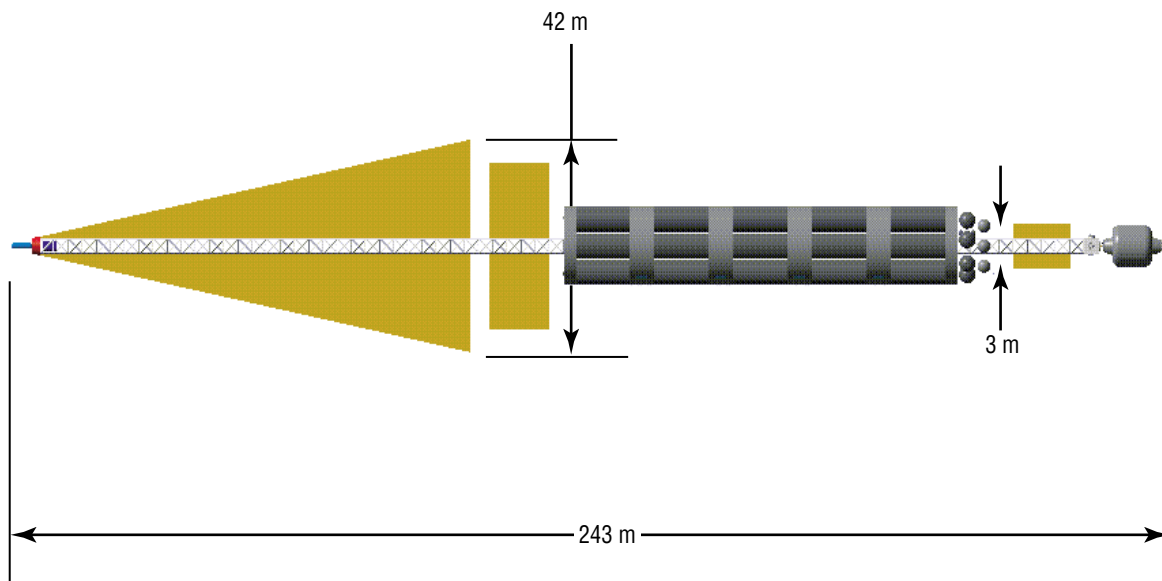


Figure 63. Piloted vehicle dimensions for SCR-MHD-MPD 120-day stay option (side view).

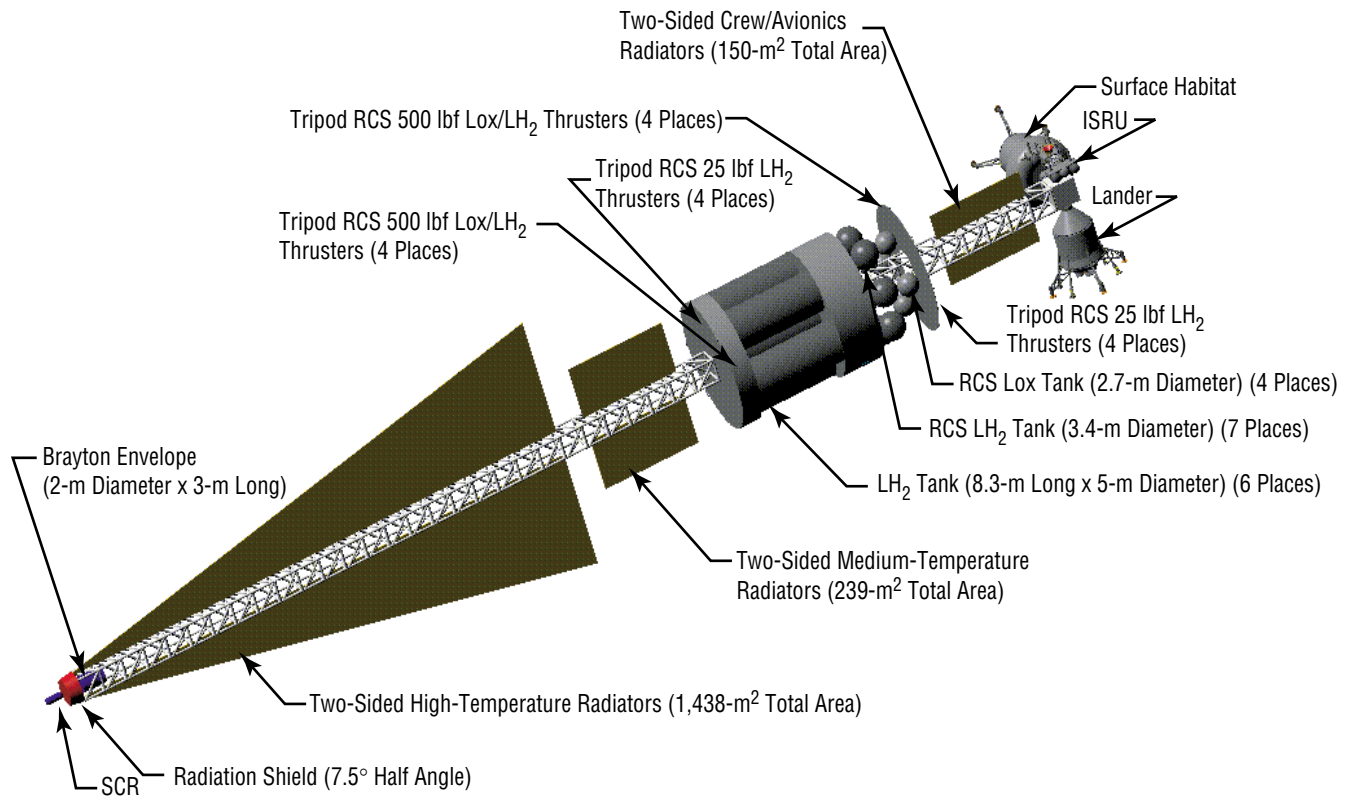


Figure 64. Cargo vehicle layout for SCR-MHD-MPD 120-day stay option.

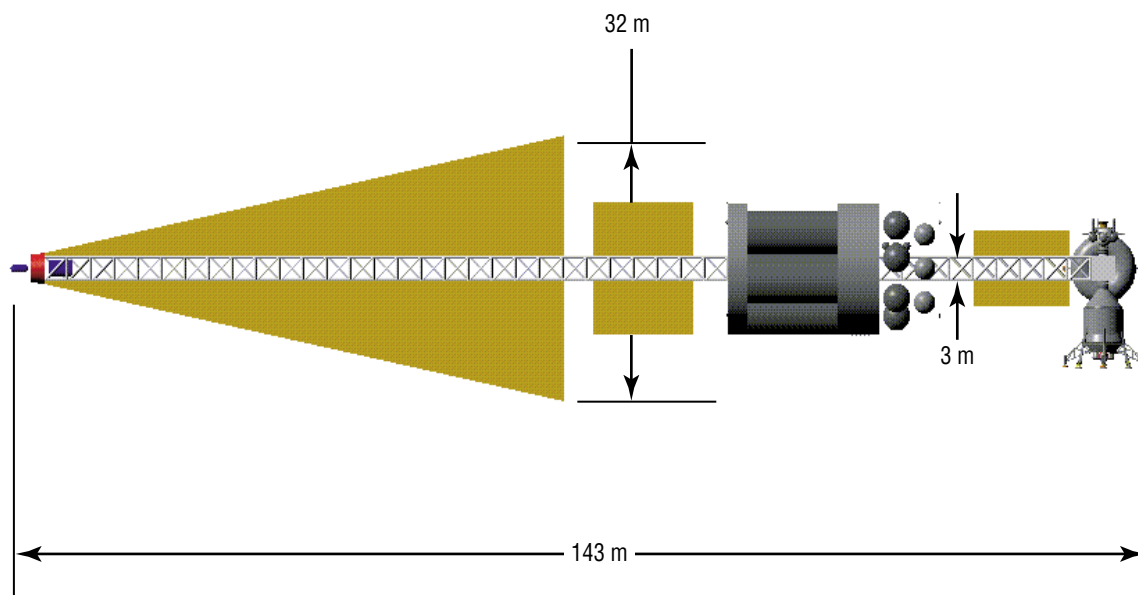


Figure 65. Cargo vehicle dimensions for SCR-MHD-MPD 120-day stay option (side view).

3. CONCLUSIONS AND RECOMMENDATIONS

The HOPE design study provided a valuable learning experience for the entire MSFC team. The two major design drivers were found to be the total time allowable for the mission and the hostile radiation environment at the target. Crew exposure to radiation is a very significant issue that was not fully addressed in the study. In a number of important areas of the design, the need for advanced technologies became very clear.

All missions to the outer solar system have high ΔV requirements and, consequently, tend to have low payload mass fractions. The high performance of the MTF propulsion system alleviates this problem for the HOPE mission; however, although propellant fractions are not inordinately high, the propulsion system has a fairly high dry mass.

Early studies demonstrated that a judicious selection of mission trip time could improve payload mass. For instance, an earlier trajectory option—not presented in this TP—assumed a total mission time of 1 yr. The result was a vehicle that traveled in a retrograde direction for most of the outbound and the inbound legs. Our final MTF designs, using a mission time of 1.75 yr, avoided any retrograde trajectories. Our MPD options used a 5.5-yr total mission time. With mission times of $n+0.5$ yr, where n is an integer, trajectories depart Earth on one side of the Sun and return to Earth on the other side, thus, taking advantage of the Earth's natural rotation around the Sun.

Although not considered a part of this MSFC study, it was determined that the crew living space is a major design consideration. Even the relatively short mission durations of the MTF options may be too long for a crew of six to survive in a single Transhab module. Future studies should consider adding a second Transhab module to increase the available living and working space.

Shorter mission times greatly alleviate problems posed by both consumable mass and crew exposure to radiation. Figure 66 illustrates the total exposure expected for the MTF vehicle crew assuming 1.75-yr mission. The dashed lines indicate the total allowable exposure for a crewmember in low-Earth orbit. The MTF vehicle would maintain exposure below lifetime limits for males as young as 35 yr and females of age 45 or more if a simple aluminum shield of 4 gm/cm² is provided. A somewhat thicker shield, with an areal density of 20 gm/cm² of aluminum, will almost permit females of age 35 and above, and males of age 25 and above, to make the journey. Results for several advanced shielding materials are also plotted on the graph.

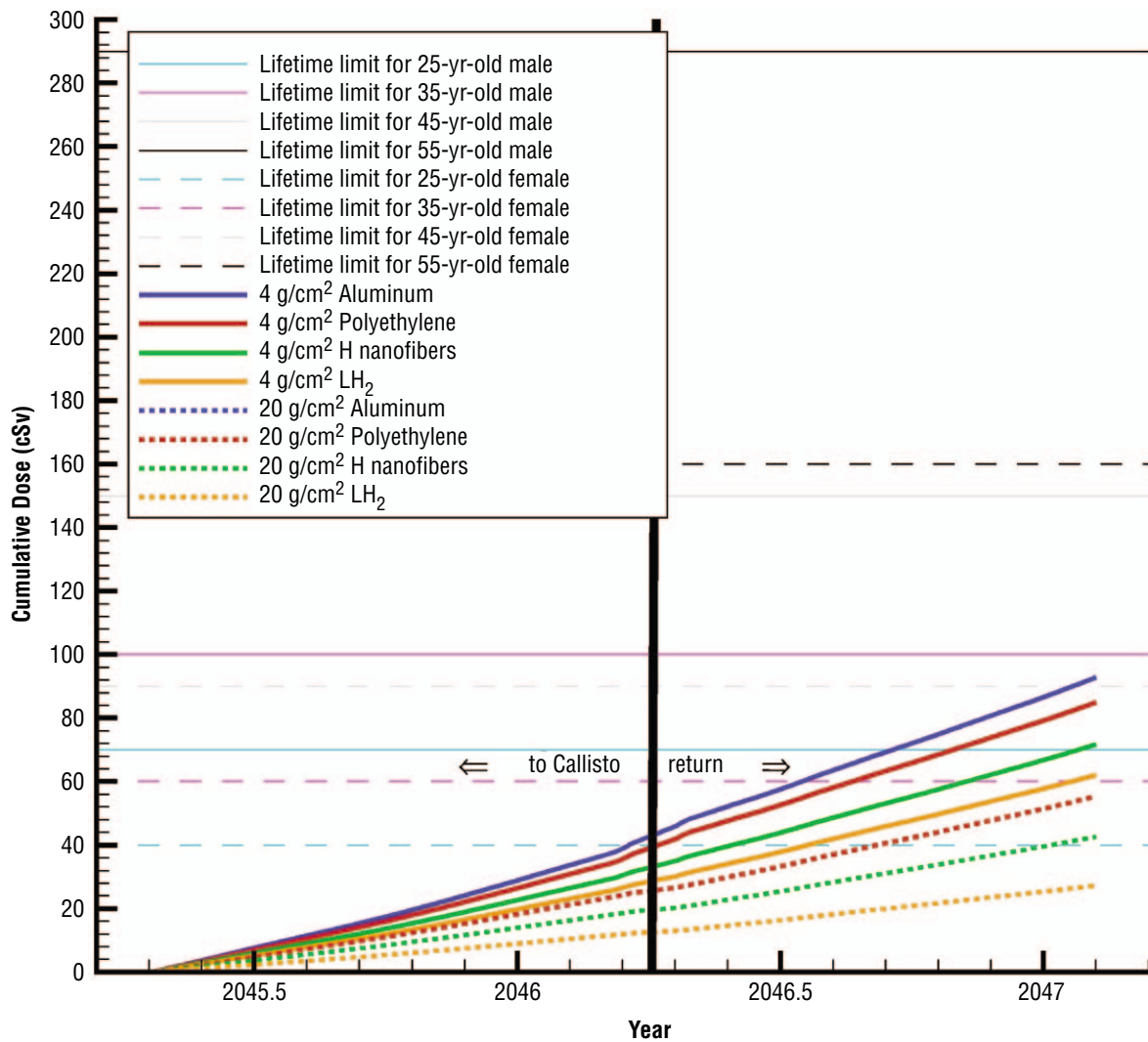


Figure 66. Cumulative dose for the MTF 30-day D-D mission to Callisto.

For comparison, figure 67 illustrates the results for a vehicle designed by LaRC and GRC under the RASC HOPE activity. This vehicle requires 5.5 yr to make the round trip to Callisto and uses the variable specific impulse magnetoplasma rocket (VASIMR) propulsion system. Note that for this vehicle, the propellant tanks are located around the Transhab to provide additional radiation shielding for the crew. For this configuration, the total exposure is represented by the 4 g/cm² LH₂ line. Even with the extra shielding provided by the tanks, the exposure exceeds recommended limits for all males except those age 55 and older.

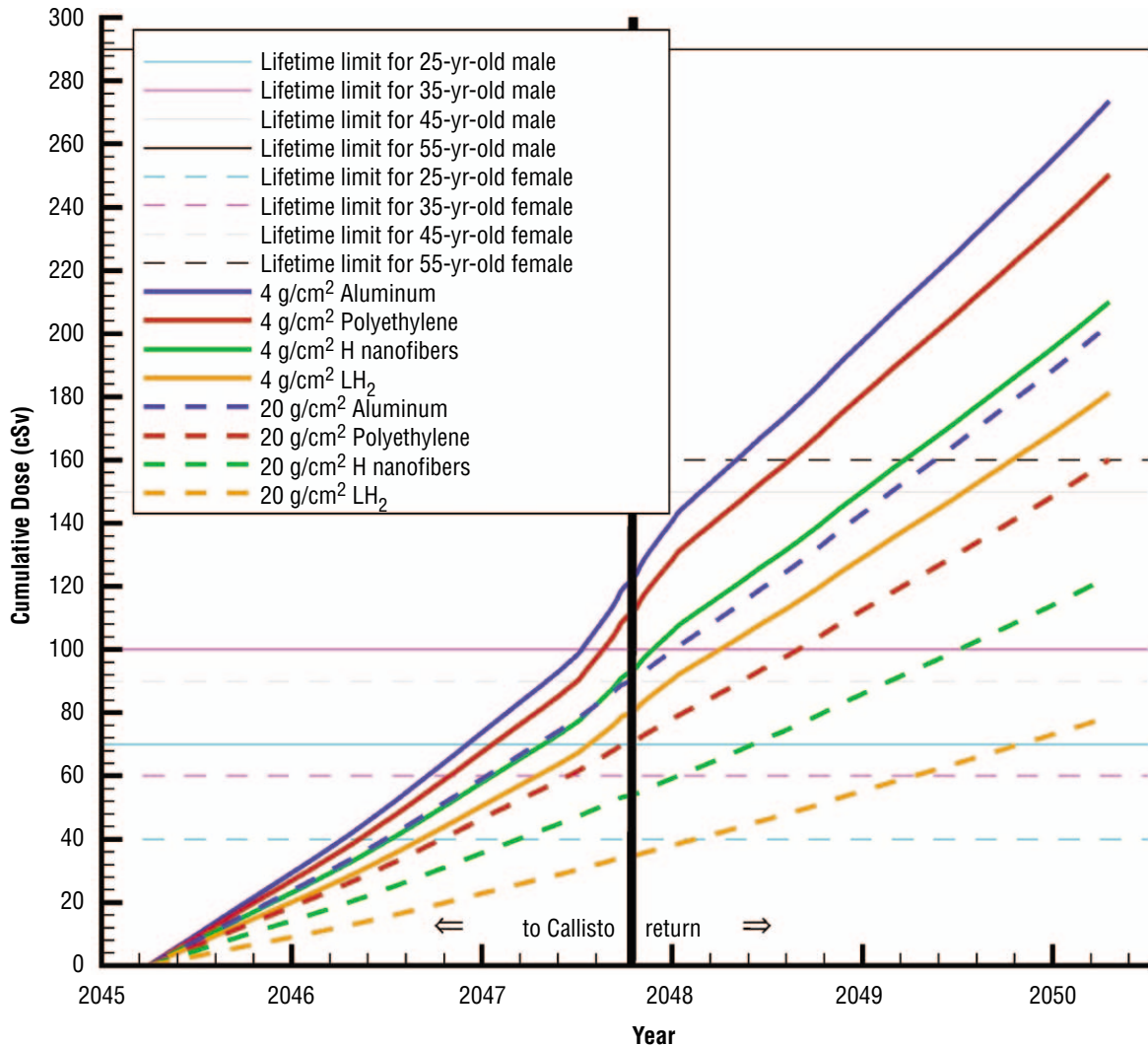


Figure 67. Cumulative dose for the LaRC and GRC VASIMR mission to Callisto.

Calculations of nominal radiation exposure as a function of mission elapsed time were performed by the radiation research group directed by Dr. J.W. Wilson at LaRC. Practically all of the total incurred dose was a result of galactic cosmic radiation exposure, and computations were carried out for the various materials (fig. 66) using the HZETRN heavy ion transport code.³⁰ The slight increase of slope near the midmission time period is due to the added contribution from Jovian trapped electrons for which the transport and incurred dose was computed with the electron code of “Transport of Space Environment Electrons: A Simplified Rapid-Analysis Computational Procedure” by J.E. Neal et al.³¹

In developing a detailed design for the MTF propulsion system, the MSFC team encountered a number of technical challenges in addition to the well-known challenges arising from the physics of the fusion event itself. Most of these challenges were overcome, but several still remain to be fully resolved.

The structure of the MTF device is exposed to very demanding thermal and nucleonic environments that will probably necessitate the use of advanced materials. The final design uses a 40-cm-deep layer of FLiBE to shield all exposed components. While this may be enough to handle the thermal environment, it may not be sufficient to satisfactorily attenuate the neutron flux from the fusion pulses. Uncertainty over this issue is due to the fact that it is unclear how much neutron moderation will take place in the hydrogen plasma that surrounds the central or fusing region of the plasmoid. In the absence of a detailed analysis, which is beyond the scope of these HOPE activities, it is conservatively estimated that only 20 percent of the neutron energy is moderated by the plasma. A full analysis of the moderation mechanism is required. If, as anticipated, the results do show that our 20-percent estimate was excessively conservative, then the current MTF structural design will contain ample design margin. However, if the results indicate that moderation is not significant, then it may be necessary to consider a more complex and advanced form of neutron shielding to protect the MTF structure and components. A composite neutron shield, comprised of different materials that are selected and combined in such a way as to absorb and scatter neutrons at different energies, might be the solution. Also note that the shielding calculations did not account for escape paths, such as those through the plasma guns. Such issues should also be addressed in a future study.

There is also a need to fund additional computational studies of plasmoid compression, fusion, and subsequent expansion. Work in this area was conducted at the Fusion Technology Institute, part of the University of Wisconsin-Madison, under the auspices of the HOPE program. This task attempted to model MTF implosion dynamics and investigate potential plasma instabilities using a discrete simulation Monte Carlo computer program, named Icarus, developed at Sandia National Laboratory. Unfortunately, this work proceeded in parallel with the MSFC mission studies, so there was no opportunity to make use of its findings; however, initial indications are that there are no fundamental problems with the processes.³²

Successful design and operation of the plasma guns are clearly vital if the MTF concept is to succeed. Since these guns are required to pulse 20 times/s for about one-third of the total mission duration, it is possible that some of these guns will fail. Mentioned earlier, the MTF concept appears to be very resilient in this regard; satisfactory compression and fusion are still possible with several nonfunctional guns. However, this needs to be confirmed by analysis, and some corresponding reliability analysis needs to be conducted on the guns themselves.

Aside from specific technical issues relating to the vehicle, the HOPE program also uncovered some limitations in our study methodology. A significant portion of the available time was spent setting up the process by which design iterations were to be conducted. The sequence in which various systems and subsystems were to be analyzed and the way in which information was to be passed between the various discipline experts had to be established before the iteration process could commence. The design process was further slowed by the inability to directly cross-connect the various design tools. Considerable effort was expended on issues relating to data reduction and transfer between engineers. As a result of this experience, the MSFC team has identified a pressing need for a high-fidelity suite of both interacting and integrated computer programs to support interplanetary mission design activities in the future.

Regarding the various propulsion techniques that were studied, it is the MSFC team's opinion that MTF offers the greatest prospects for the type of ambitious, crewed missions considered during the HOPE activity. Although a fusion-based propulsion system may appear ambitious, the alternate vehicles studied

within the HOPE program all required development of multiple elements of advanced technology, such as advanced MPD thrusters, low-area-density radiators, high neutron shielding, ISRU plants, and advanced structural materials. Even with these advances, the resulting mission times were substantially higher than for MTF. To further complicate matters, most of these alternate propulsion techniques required a split mission architecture with separate cargo and piloted vehicles. Additionally, the mass margins assumed on some of the alternate vehicles were very optimistic; they were sometimes of the order of those used in the design of expendable launch vehicles, which use well-established, 40-yr-old technology. Wherever possible, the MTF vehicles used current levels of technology so that the MTF engine is the only major development required. The authors feel that development of the MTF system will result in equal or lower cost and programmatic risk than the alternate strategy of developing the extensive range technologies required by the other vehicles. For these reasons, further investment in MTF development is strongly merited.

APPENDIX A—ELEMENTARY MAGNETIZED TARGET FUSION MAGNETIC NOZZLE THEORY

In this appendix, a simple model is developed to allow the determination of the plasma trajectory and estimate the resulting thrust force on each coil. The model is based on an expanding-shell treatment of the plasma after fusion has taken place. The plasma is treated as a collection of particles that, at least initially, are expanding in a radial manner away from the nozzle focus; i.e., location of the fusion event.

The situation at the moment of fusion is shown in figure 68. The seed magnetic field lines are shown, as are the coils. Note that, as no plasma expansion has yet taken place, the seed field is still undeformed.

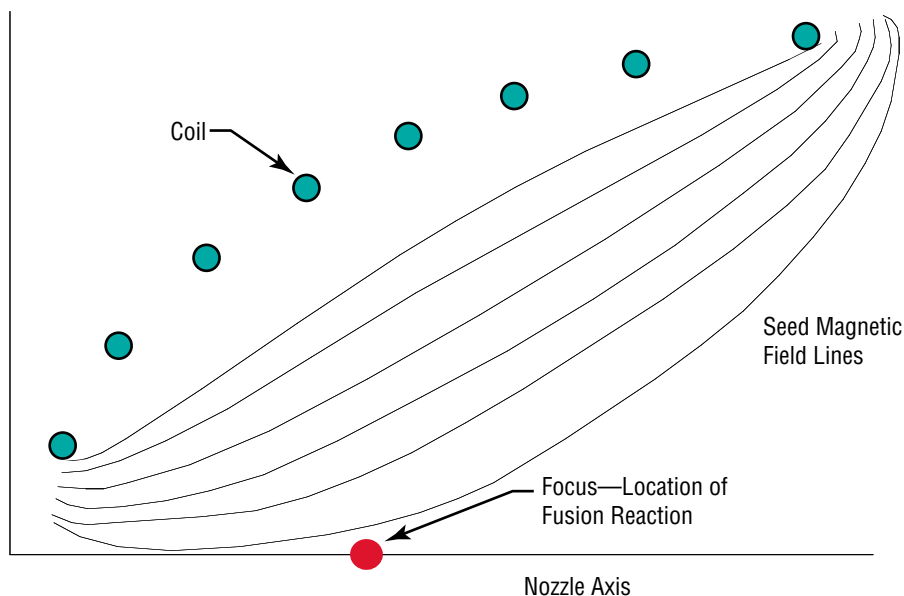


Figure 68. Nozzle magnetic field at fusion burn.

The situation shortly after fusion is shown in figure 69. The plasma is now shown as a shell (dark ring), which is expanding in a radial manner away from the focus. Note that, as the expansion is relatively small so far, the magnetic field has not been disturbed significantly and consequently the shell is still essentially spherical.

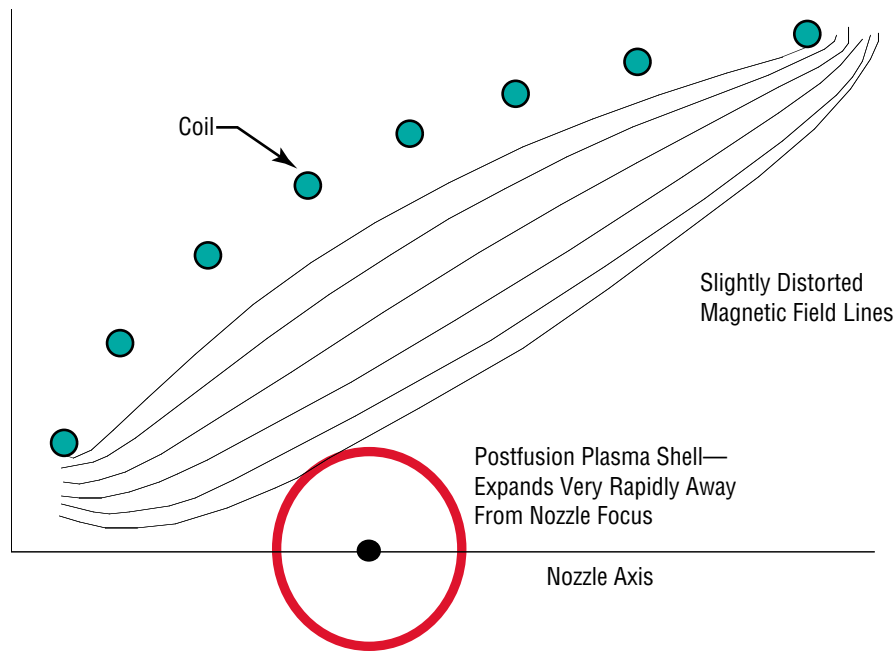


Figure 69. Nozzle magnetic field shortly after fusion burn.

Further expansion of the plasma shell is increasingly anisotropic due to the presence of the magnetic field. Figure 70 shows the situation later, near or at the point of maximum expansion. Note that the outer curve represents a section through the limiting parabolic surface—the theoretical maximum possible extent of plasma expansion. (Further expansion would physically impinge on the coils.) As explained in section 2.3.1, while the plasma cloud expands, it effectively pushes the magnetic flux ahead of it, compressing it into the ever-diminishing region between it and the limiting parabolic surface. The plasma particles are still spread out within a thin shell that is now closely configured to the parabola of the magnetic nozzle.

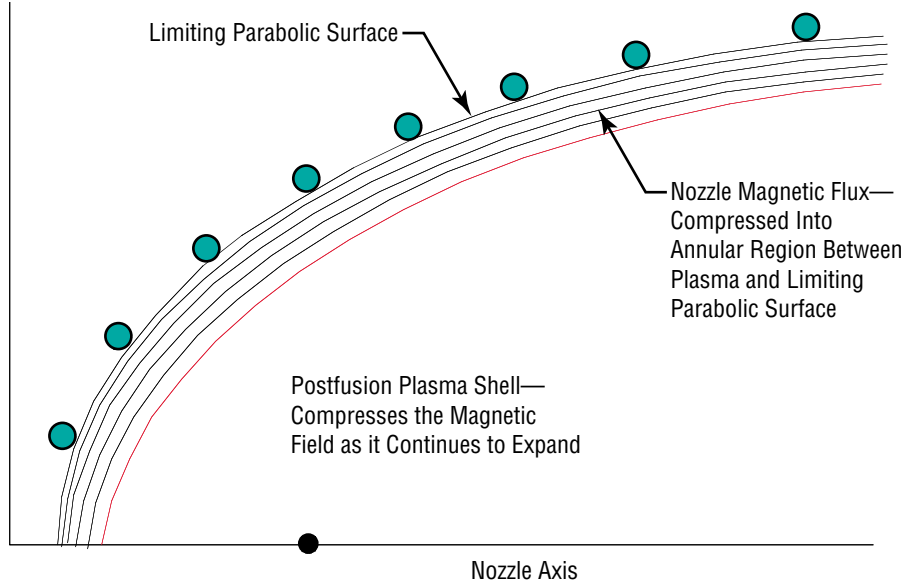


Figure 70. Nozzle magnetic field at maximum plasma expansion.

For the purposes of this first-order analysis, the plasma cloud boundary will always be treated as a parabola with focus coinciding with that of the limiting parabolic surface. Consider a point relatively late in the plasma expansion, when the region between the plasma shell and the limiting parabolic surface is small. Within this region, the magnetic field magnitude can be taken to be spatially constant and the field lines, parallel to the two bounding surfaces (fig. 70). Although the analysis applies to the last stages of plasma expansion and the first stages of rebound, the consequent loss of overall accuracy should be limited since it is only during these stages, with significant field compression, that the force acting on the plasma becomes large. Hence, the most critical phase of nozzle operation is being analyzed here.

Denoting the total magnetic flux by Φ and referring to figure 71, one can see that

$$\Phi = A_{\text{con}} B \cos\left(\frac{\theta}{2}\right), \quad (9)$$

where A_{con} is the total area of the conical annulus formed by rotating the line PQ through one revolution about the nozzle main axis and B is the magnitude of the magnetic field.

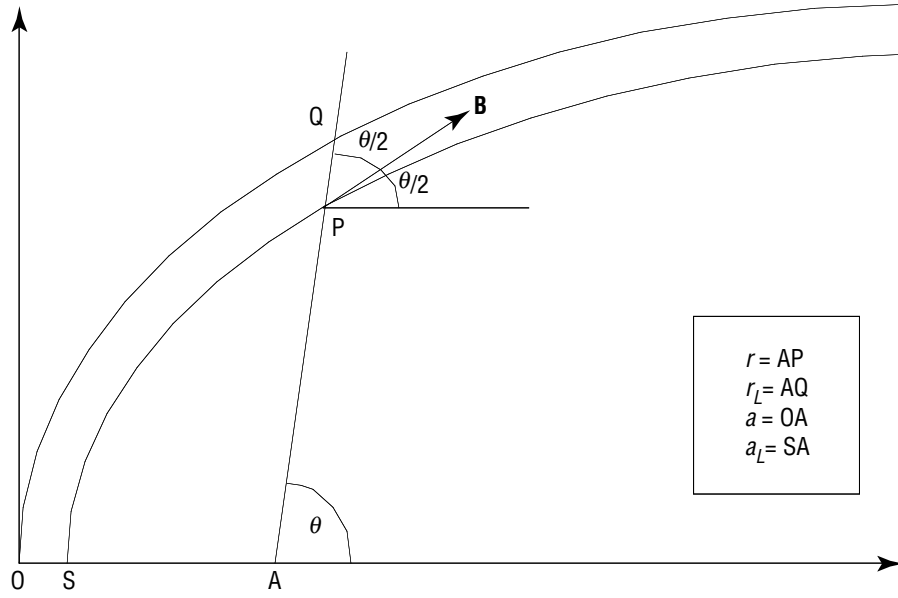


Figure 71. Nozzle magnetic field geometry.

The area, A_{con} , is derived as follows. The derivation is a little clearer if one uses a diagram focused purely on a cone, as shown in figure 72.

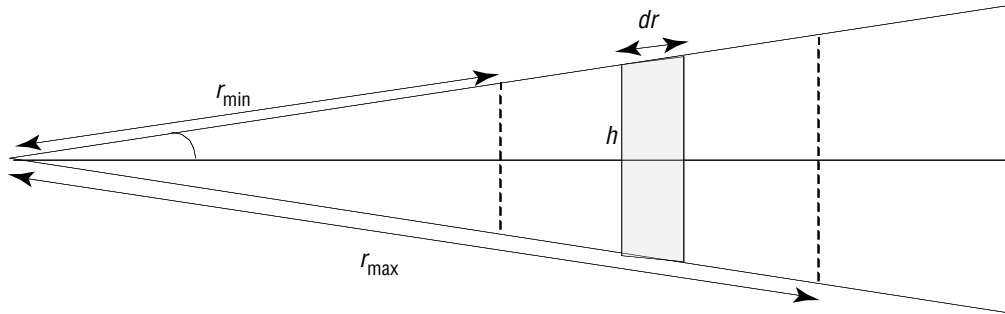


Figure 72. Diagram illustrating cone surface area.

In figure 72, the area of the small shaded conical annulus is given by

$$dA_{\text{con}} = 2\pi h dr \quad , \quad (10)$$

and because

$$h = r \sin \theta \quad , \quad (11)$$

integration gives

$$A_{\text{con}} = \pi \sin \theta (r_{\text{max}}^2 - r_{\text{min}}^2) \quad . \quad (12)$$

Noting that the equations of the two parabolas can be written as

$$r = \frac{2a}{1 - \cos \theta} \quad (13)$$

and

$$r_L = \frac{2a_L}{1 - \cos \theta} , \quad (14)$$

where a and a_L are defined in figure 73, gives the following expression for the area of the conical annulus in figure 71:

$$A_{\text{con}} = 4\pi \sin \theta \frac{a_L^2 - a^2}{(1 - \cos \theta)^2} . \quad (15)$$

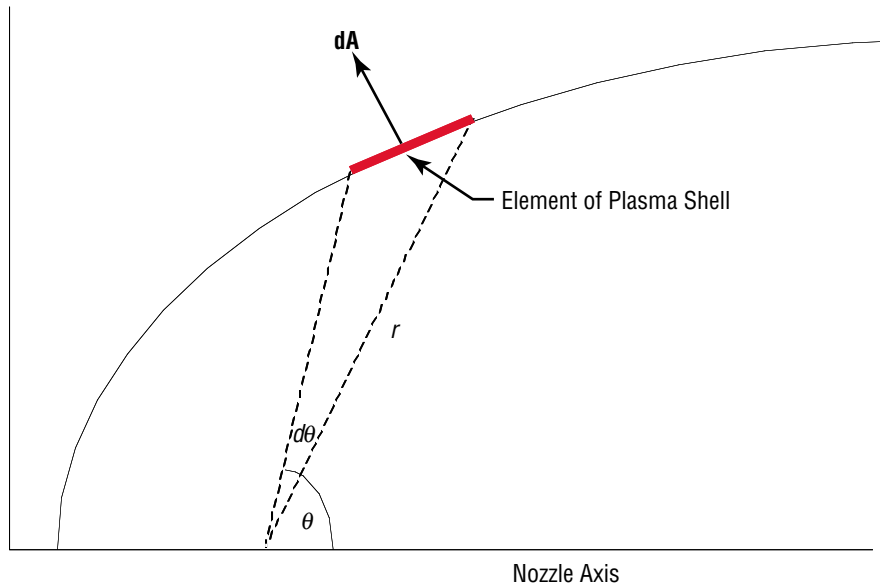


Figure 73. Diagram illustrating an element of a plasma shell.

Combining equations (5) and (15) gives

$$B = \frac{\Phi \sin^2\left(\frac{\theta}{2}\right)}{2\pi(a_L^2 - a^2) \cos\left(\frac{\theta}{2}\right)} . \quad (16)$$

Now the expulsive force acting on the plasma can be represented as an integral of the magnetic pressure (p_B) over the surface of the plasma cloud, where

$$p_B = \frac{B^2}{\mu} , \quad (17)$$

where μ is the magnetic permeability.

To determine the force, an appropriate small element of the plasma shell and its associated surface area on which the magnetic pressure acts needs to be determined. The element is shown in cross section (in bold) in figure 73. The vector surface area ($d\mathbf{A}$), shown in fig. 73 edge on, is exposed to and experiences the pressure due to the compressed magnetic flux.

The nozzle is symmetric about the main axis and the element extends through an angle $d\varphi$ about this axis (φ being the azimuthal angle that completes the coordinate system). To first order, the only force acting upon it is that due to magnetic pressure, acting across the vector surface area ($d\mathbf{A}$).

The $d\mathbf{A}$ of this element can be decomposed as shown in figure 74, which—to assist visualization—has the two following views of the element: (1) An oblique (fig. 74(a)) (showing the φ dimension) and (2) a cross section (fig. 74(b)):

$$d\mathbf{A} = dA_\theta \mathbf{e}_\theta + dA_r \mathbf{e}_r , \quad (18)$$

where \mathbf{e}_θ , \mathbf{e}_r , and \mathbf{e}_φ are respectively unit vectors in the θ , r , and φ directions.

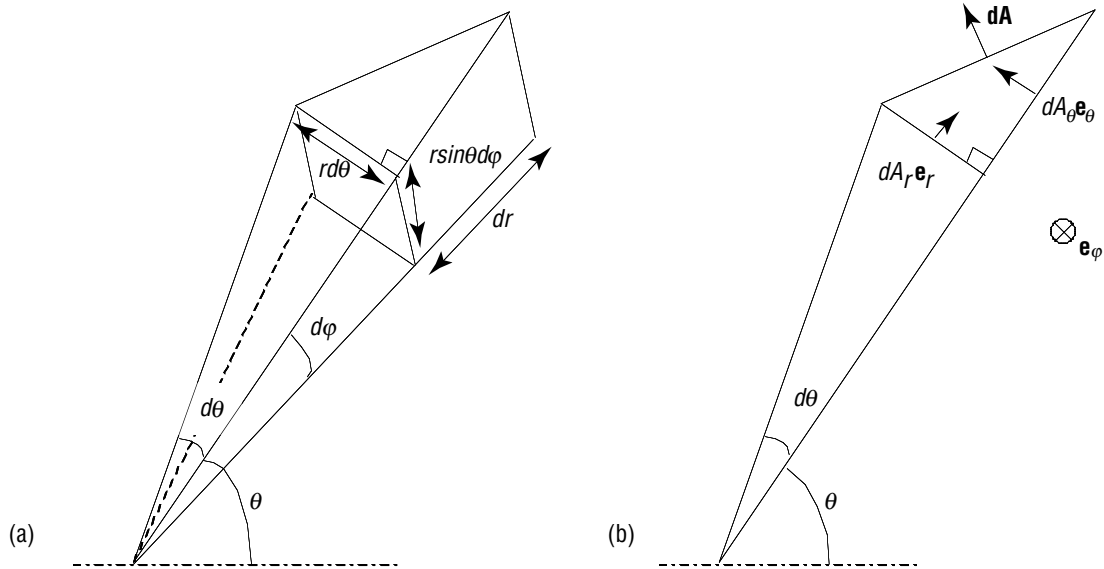


Figure 74. Geometry of a plasma element shown in (a) the φ dimension and (b) a cross-sectional view.

From figure 74, one can see that

$$dA_r = rd\theta r \times \sin\theta d\varphi \quad (19)$$

and

$$dA_\theta = dr \times r \sin\theta d\varphi ; \quad (20)$$

therefore,

$$\mathbf{dA} = r \sin\theta dr d\varphi \mathbf{e}_\theta + r^2 \sin\theta d\theta d\varphi \mathbf{e}_r . \quad (21)$$

The immediate objective of this analysis is to derive a simple equation of motion for the plasma element. The solid angle subtended by the element at the focus $d\Omega$ is given by

$$d\Omega = \sin\theta dr d\varphi . \quad (22)$$

Using equation (12), equation (23) may be rewritten as

$$\mathbf{dA} = r^2 \sin\theta d\theta d\varphi \left(\mathbf{e}_\theta \frac{\sin\theta}{1 - \cos\theta} + \mathbf{e}_r \right) , \quad (23)$$

which can be simplified to

$$\mathbf{dA} = r^2 d\Omega \left(\mathbf{e}_\theta \cot\left(\frac{\theta}{2}\right) + \mathbf{e}_r \right) . \quad (24)$$

Now the pressure force acting on the element is given by

$$\mathbf{dF} = -p_B \mathbf{dA} , \quad (25)$$

and thus,

$$\mathbf{dF} = -p_B r^2 d\Omega \left(\mathbf{e}_\theta \cot\left(\frac{\theta}{2}\right) + \mathbf{e}_r \right) . \quad (26)$$

To derive an equation of motion for the element, an expression is needed for its mass. Since the plasma shell expansion is initially isotropic, it is reasonable to suppose that the mass of plasma per unit solid angle is constant for all directions; i.e., for all values of θ and φ . This means that if two plasma elements with the same solid angle—but at different angles—are considered, they will both contain the same mass of plasma. This is illustrated in figure 75.

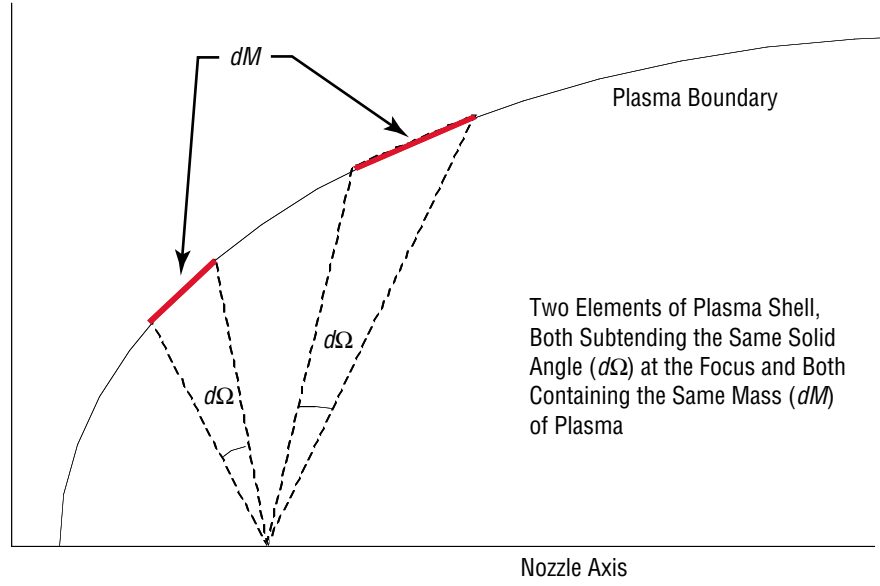


Figure 75. Isotropy of plasma expansion.

Note that this assumption will only hold while the plasma motion is predominantly in the radial direction, away from the nozzle focus, and the magnetic field compression is increasing. Once the compression reverses; i.e., the field expands again, and the plasma starts to be expelled from the nozzle, the motion will no longer be radial and our assumption will rapidly break down. However, as was stated at the outset, this analysis concentrates on the last stages of magnetic field compression and the first stages of expansion, when the forces are at their maximum.

Under these circumstances, the mass of plasma in an element can be written as

$$dM = M \frac{d\Omega}{4\pi} , \quad (27)$$

where M is the total mass of plasma, and thus, equation (18) can be written as

$$\mathbf{dF} = -4\pi p_B r^2 \frac{dM}{M} \left(\mathbf{e}_\theta \cot\left(\frac{\theta}{2}\right) + \mathbf{e}_r \right) . \quad (28)$$

Now the equation of motion for the plasma element can also be written as

$$\mathbf{dF} = dM \frac{d\mathbf{v}}{dt} , \quad (29)$$

where \mathbf{v} is the element velocity; hence,

$$\frac{d\mathbf{v}}{dt} = -\frac{4\pi p_B r^2}{M} \left(\mathbf{e}_\theta \cot\left(\frac{\theta}{2}\right) + \mathbf{e}_r \right) . \quad (30)$$

Equation (26) can be integrated numerically to give the time-evolution of r for a given value of θ , bearing in mind that p_B is a time-dependent quantity.

The force acting on the nozzle is a reaction to the force acting on the plasma. If one considers an element of plasma defined by the following angular intervals:

$$\theta = \theta_i \rightarrow \theta_{i+1} \quad (31)$$

and

$$\varphi = \varphi_j \rightarrow \varphi_{j+1} \quad (32)$$

The thrust force due to this element of plasma, denoted by $\mathbf{F}(\theta_i \rightarrow \theta_{i+1}, \varphi_j \rightarrow \varphi_{j+1})$, is given by

$$\mathbf{F}(\theta_i \rightarrow \theta_{i+1}, \varphi_j \rightarrow \varphi_{j+1}) = - \int_{\varphi_j}^{\varphi_{j+1}} \int_{\theta_i}^{\theta_{i+1}} \frac{M}{4} \frac{d\mathbf{v}}{dt} \sin \theta d\theta d\varphi, \quad (33)$$

which, given that there is symmetry about the nozzle main axis, can be simplified by completing the azimuthal angle integral to give

$$\mathbf{F}(\theta_i \rightarrow \theta_{i+1}, \varphi_j \rightarrow \varphi_{j+1}) = -(\varphi_{j+1} - \varphi_j) \int_{\theta_i}^{\theta_{i+1}} \frac{M}{4} \frac{d\mathbf{v}}{dt} \sin \theta d\theta. \quad (34)$$

This expression can be used to estimate the thrust force experienced by each individual coil. To do this, assume that each coil experiences the reaction force due to that portion of the plasma that has a polar angle closer to it than to any other coil. If coils $i-1$, i , and $i+1$ have polar angles of θ_{i-1} , θ_i , and θ_{i+1} , respectively, then the portion of plasma with polar angle between $(\theta_{i-1} + \theta_i)/2$ and $(\theta_{i+1} + \theta_i)/2$ is associated with coil i , illustrated in figure 76.

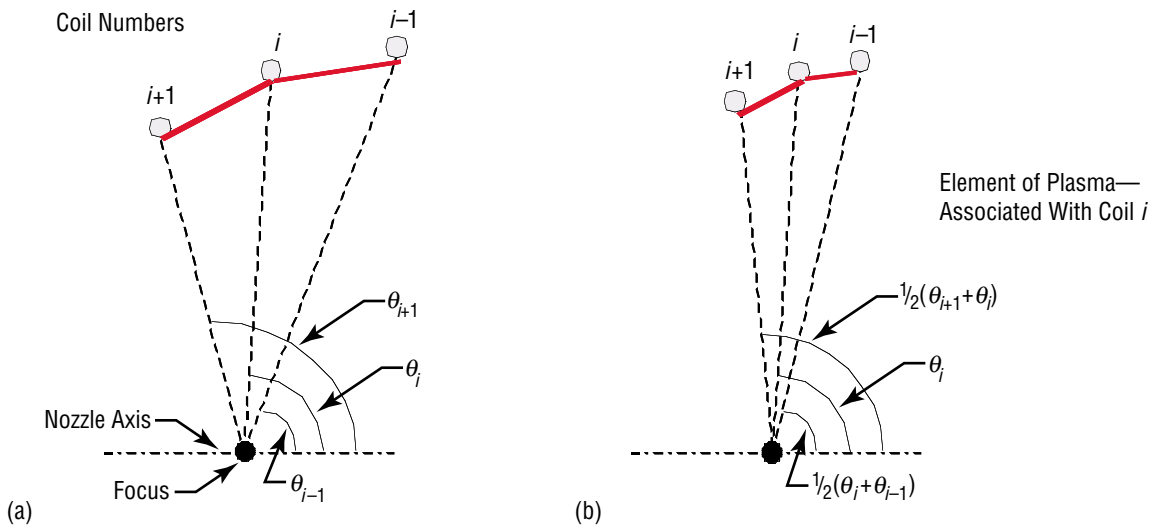


Figure 76. Plasma element for numerical analysis: (a) Coil and polar angle numbering system and (b) element of plasma associated with the i th coil.

Using this simple model and assuming that the force is not a strong function of the polar angle, the total force experienced by coil i , denoted by \mathbf{F}_i , is given by

$$\mathbf{F}_i \approx -2\pi \frac{M}{4} \frac{d\mathbf{v}}{dt} \bigg|_{\theta_i} \int_{\frac{\theta_i + \theta_{i-1}}{2}}^{\frac{\theta_{i+1} + \theta_i}{2}} \sin \theta d\theta , \quad (35)$$

where $\frac{d\mathbf{v}}{dt} \bigg|_{\theta_i}$ denotes the value of $d\mathbf{v}/dt$ at polar angle θ_i .

This gives

$$\mathbf{F}_i \approx \frac{M}{2} \frac{d\mathbf{v}}{dt} \bigg|_{\theta_i} \left[\cos\left(\frac{\theta_{i+1} + \theta_i}{2}\right) - \cos\left(\frac{\theta_i + \theta_{i-1}}{2}\right) \right] . \quad (36)$$

For design and performance analysis purposes, the axial and radial components of this force are required, as shown in figure 77.

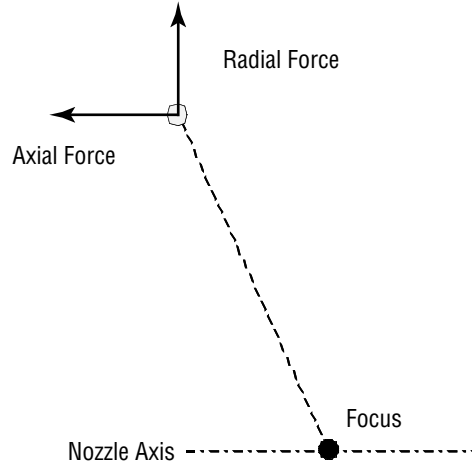


Figure 77. Axial and radial directions.

The radial and axial unit vectors are given respectively by

$$\mathbf{e}_{\text{radial}} = \mathbf{e}_{\theta} \cos \theta + \mathbf{e}_r \sin \theta \quad (37)$$

and

$$\mathbf{e}_{\text{axial}} = -\mathbf{e}_{\theta} \sin \theta + \mathbf{e}_r \cos \theta . \quad (38)$$

To complete this first-order model, derive an expression for the magnetic field, \mathbf{B} , which is done using the following simple model. For the j th coil, define the following:

- $L_{s,j}$ =initial inductance, when only the seed magnetic field is present; i.e., before the fusion event has occurred.
- $L_{c,j}$ =inductance at peak magnetic compression; i.e., when the plasma cloud has expanded to its greatest extent.
- $I_{s,j}$ =initial current, which produces the seed magnetic field.
- $I_{c,j}$ =maximum current, peak magnetic compression.

The assumption that the flux linking a given coil does not change during compression and the assumption that the flux linking all coils is the same, which is a plausible assumption (fig. 78), enables the arrival at the expressions

$$L_{s,j}I_{s,j} = \Phi \quad (39)$$

and

$$L_{c,j}I_{c,j} = \Phi \quad (40)$$

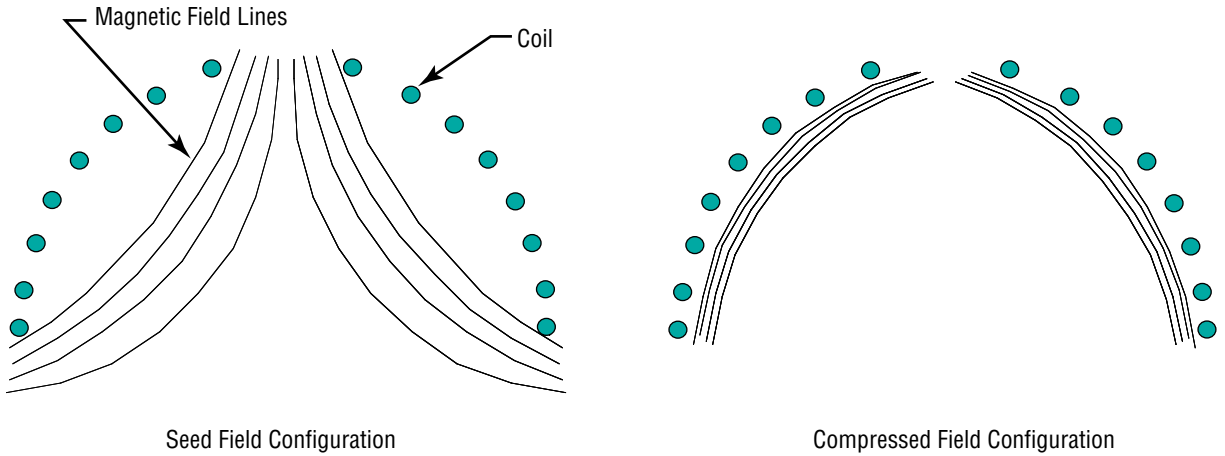


Figure 78. Magnetic field configuration (a) before and (b) after compression.

The total magnetic field energy of all coils before compression, $E_{B,s}$, is given by

$$E_{B,s} = \frac{1}{2} \sum L_{s,j} I_{s,j}^2 \quad (41)$$

where the summation is over j , here and in all subsequent uses of the Σ symbol, and that at maximum compression, $E_{B,c}$ is given by

$$E_{B,c} = \frac{1}{2} \sum L_{c,j} I_{c,j}^2 . \quad (42)$$

Finally, assume that the current amplification factor; i.e., the ratio of a coil's current at maximum compression to that during seed conditions, is the same for all coils. Denoting this quantity by A , this assumption can be expressed as

$$A = \frac{I_{c,j}}{I_{s,j}} . \quad (43)$$

Equations (39) and (40) can be used to eliminate $I_{c,j}$ from equations (42) and (43) to give

$$A L_{c,j} I_{s,j} = \Phi \quad (44)$$

and

$$E_{B,c} = \frac{A^2}{2} \sum L_{c,j} I_{s,j}^2 . \quad (45)$$

Next, $L_{c,j}$ can be eliminated between equations (43) and (44) to give

$$E_{B,c} = \frac{A}{2} \sum \Phi I_{s,j} . \quad (46)$$

Finally, $I_{s,j}$ can be eliminated from equation (45) by using equations (37) and (38) to give

$$E_{B,c} = \frac{A \Phi^2}{2} \sum \frac{1}{L_{s,j}} . \quad (47)$$

Equations (37) and (38) can also be used to eliminate $I_{s,j}$ from equation (40) to give

$$E_{B,s} = \frac{\Phi^2}{2} \sum \frac{1}{L_{s,j}} . \quad (48)$$

Equations (46) and (47) show that

$$E_{B,c} = A E_{B,s} , \quad (49)$$

and hence, that the current amplification factor is also the energy multiplication factor.

Now the energy input to the magnetic field due to plasma expansion is denoted by ΔE_B and is clearly given by

$$\Delta E_B = E_{B,c} - E_{B,s} , \quad (50)$$

and hence,

$$\Delta E_B = (A - 1) \frac{\Phi^2}{2} \sum \frac{1}{L_{s,j}} . \quad (51)$$

Note that $L_{s,j}$ can be calculated from the basic coil design details using

$$L_{s,j} = \mu R_j \left[\ln \left(\frac{4\pi R_j}{a_j} \right) - 2.45 \right] , \quad (52)$$

where μ is the magnetic permeability, R_j is the major radius of coil j , and a_j is its cross-sectional radius.

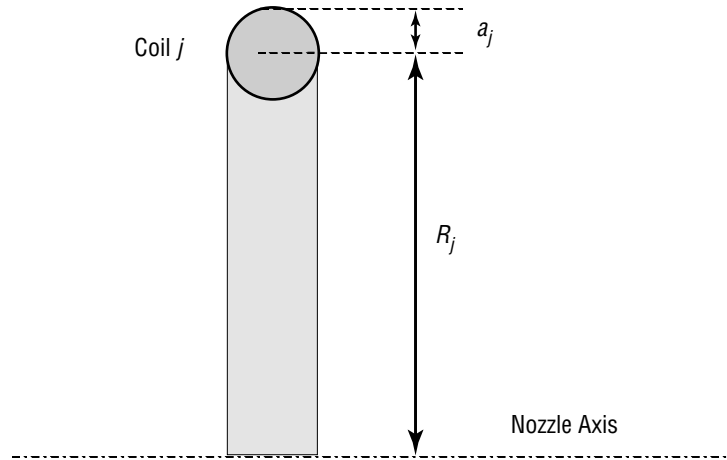


Figure 79. Coil dimensions.

Now the value of ΔE_B is derived from the fusion analysis, which leaves only A and Φ as unknowns. Selection of A is a design decision, leaving Φ as the sole variable, which can be derived, using equation (47):

$$\Phi = \frac{2\Delta E_B}{(A - 1) \sum \frac{1}{L_{s,j}}} . \quad (53)$$

Note that the choice of amplification factor, A , does impact the flux required, Φ . A high amplification factor requires less flux.

The magnetic field will increase as the plasma cloud expands and the flux, Φ , is confined to a progressively smaller region. This is illustrated below in figure 80, which shows a cross section through the nozzle at various stages of the plasma expansion.

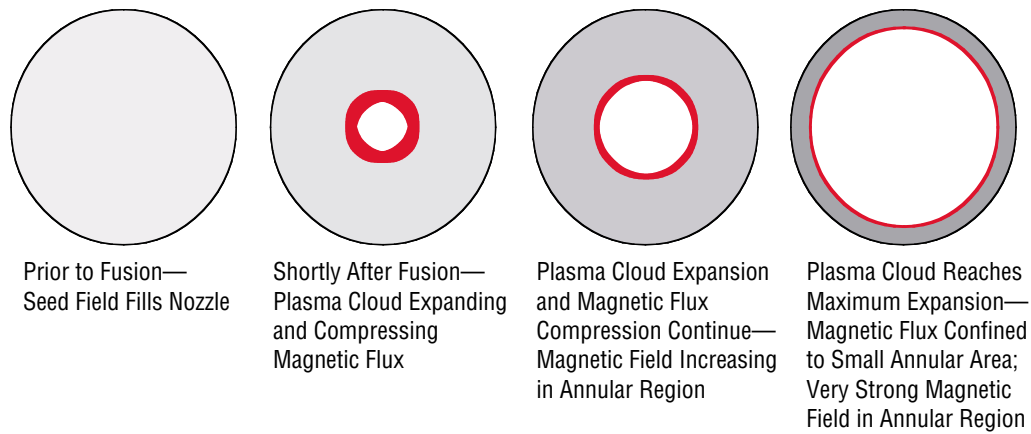


Figure 80. Stages of magnetic field compression.

The means by which this set of equations can be used to model the plasma trajectories is outlined as follows.

First the plasma shell is divided into N discrete segments as shown below in figure 81.

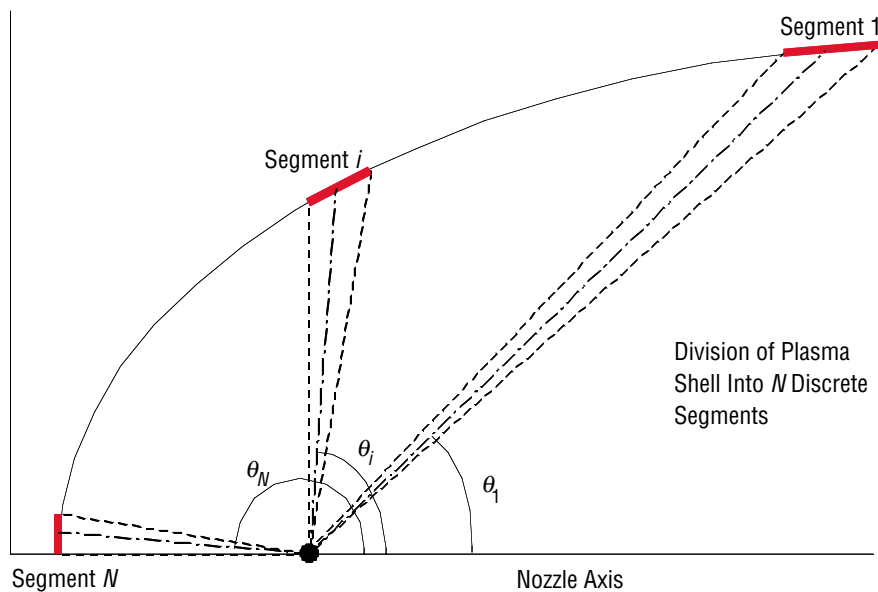


Figure 81. Division of plasma shell into discrete segments.

For each segment, the plasma is assumed to be concentrated at the midpoint; e.g., the i th segment is treated as being entirely located at the point (r_i, θ_i) .

The main objective of this analysis is to determine the trajectory of each segment, as represented by $r_i(t)$ and $\theta_i(t)$, where t denotes the time.

A.1 Initial Plasma Shell Conditions

At the start of the analysis ($t=0$), the plasma shell is assumed to be of paraboloid shape and conforming to

$$r_i(0) = \frac{2a_0}{1 - \cos\theta_i(0)} , \quad (54)$$

where the parameter a_0 , distance from the parabola focus to its vertex, defines the initial parabola.

The effects of any magnetic field compression that has taken place between the fusion event itself and the plasma shell reaching this starting configuration are neglected. This means that the plasma shell is expanding outwards with the full charged-particle kinetic energy from fusion. (Note that the neutron kinetic energy is not included; also, a subtraction must be made to allow for radiation losses from the charged particles as they expand.)

Clearly, not all of this kinetic energy will eventually be absorbed by the magnetic field because the nozzle is open at one side, which allows the plasma on this side to escape unimpeded. Fortunately, the charged-particle kinetic energy lost in this manner can be derived from simple geometric considerations, as shown in figure 82.

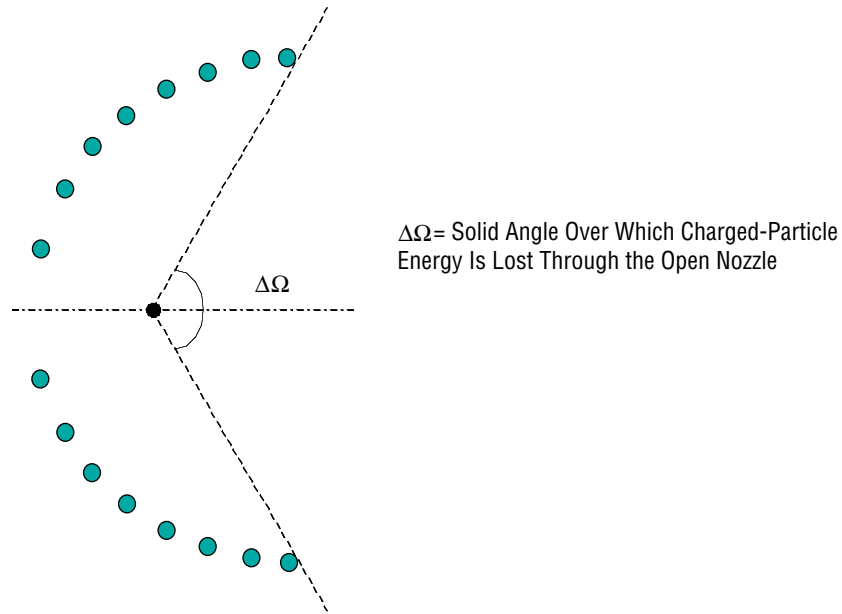


Figure 82. Open portion of nozzle.

The useful charged-particle kinetic energy (E_{cpu}) is related to the total charged-particle kinetic energy (E_{cpT}) via

$$E_{\text{cpu}} = \frac{\Delta W}{4\pi} E_{\text{cpT}} , \quad (55)$$

where E_{cpT} is determined from analysis of the fusion event itself.

The assumption is that all of the useful charged-particle kinetic energy ultimately goes into deforming the magnetic field, and thus,

$$E_{\text{cpu}} = \Delta E_B . \quad (56)$$

It follows that the initial plasma speed, in a radial manner away from the focus, v_{ri} , is given by

$$v_{ri}(0) = \sqrt{\frac{2\Delta E_B}{M}} \quad (57)$$

and is the same for all values of i . Since the plasma is assumed to be moving entirely in the radial direction, the transverse speeds are zero; therefore,

$$v_{\theta i}(0) = 0 \quad (58)$$

for all values of i .

Together, equations (53), (56), and (57) establish the initial position and speed of the plasma shell.

A.2 Initial Magnetic Flux Derivation

The flux equation is solved at the start of the evolution analysis. The required inputs are ΔE_B and the current amplification factor (A). This equation does not need to be solved again because Φ is constant under the assumptions of this treatment:

$$\Phi = \frac{2\Delta E_B}{(A-1) \sum \frac{1}{L_{s,j}}} . \quad (59)$$

A.2.1 General Time Step Calculation

Equations for the t to $t+\delta t$ time step are given below. The treatment begins with the position and speed of each segment known at time (t), having been derived from the earlier steps in the time-evolution analysis.

The magnetic field for the i th plasma segment at time (t) denoted by $B_i(t)$ is calculated using equation (11):

$$B_i(t) = \frac{\Phi \sin^2 \left[\frac{\theta_i(t)}{2} \right]}{2\pi [a_L^2 - a_i(t)^2] \cos \left[\frac{\theta_i(t)}{2} \right]}, \quad (60)$$

where $a_i(t)$ denotes the parabola constant for the i th segment. Note that, except for the $t=0$ point, when all of the plasma shell is assumed to fall on the same parabola, each segment will have its own unique parameter because, as the plasma shell evolves, it is uncertain if all the segments will continue to fall on the same parabola. The parabola constant is derived from the segment position at time (t) using

$$a_i(t) = r_i(t) \frac{1 - \cos \theta_i(t)}{2}. \quad (61)$$

The magnetic pressure at segment i , denoted $p_{Bi}(t)$, is derived using

$$p_{Bi}(0) = \frac{B_i(0)^2}{\mu}. \quad (62)$$

Next, the acceleration of segment i , denoted by $d\mathbf{v}_i/dt(t)$, is derived using

$$\frac{dv_i}{dt}(t) = -\frac{4\pi p_{Bi}(t)r_i(t)^2}{M} \left(e_\theta \cot \left(\frac{\theta_i(t)}{2} \right) + e_r \right). \quad (63)$$

If the plasma segments have been selected so that each one is centered on a coil (in which case $N=8$), then using equation (35), the force on coil i , denoted by $\mathbf{F}_i(t)$, can be written as

$$F_i(t) \approx \frac{M}{2} \frac{dv_i}{dt}(t) \left\{ \cos \frac{\theta_{i+1}(t) + \theta_i(t)}{2} - \cos \frac{\theta_i(t) + \theta_{i-1}(t)}{2} \right\}. \quad (64)$$

The position and speed of segment i at the next time step; i.e., at $t=t+\delta t$ are given approximately as follows:

$$r_i(t + \delta t) \approx r_i(t) + v_{ri}(t)\delta t, \quad (65)$$

$$\theta_i(t + \delta t) \approx \theta_i(t) + \frac{v_{\theta i}(t)}{r_i(t)} \delta t, \quad (66)$$

and

$$\mathbf{v}_i(t + \delta t) \approx \mathbf{v}_i(t) + \frac{d\mathbf{v}_i}{dt}(t)\delta t. \quad (67)$$

APPENDIX B—MAGNETOHYDRODYNAMIC POWER SYSTEM MODEL

Appendix B contains details of a simple model for the key components of an MHD power system. The three items addressed are (1) the MHD generator, which is itself comprised of two principal components, the structure and the magnetic coils; (2) the thermal regenerator; and (3) the compressor. For the purposes of analysis, mass per unit power values, commonly referred to as alphas (α) are required as follows:

- α_{struc} —MHD generator structural mass per unit net power generated.
- α_{coil} —MHD generator coil mass per unit net power generated.
- α_{regen} —thermal regenerator mass per unit heat transferred across the regenerator.
- α_{comp} —compressor mass per unit power required by to operate the compressors.

The analysis that follows is based on the alphas given in “Prospects for Nuclear Electric Propulsion Using Closed-Cycle Magnetohydrodynamic Energy Conversion”:³³

- For the MHD generator structure,

$$\alpha_{\text{struc}} = \frac{B^2}{2\mu_0 P_{\text{gen}} \left(\frac{s_t}{\rho} \right)} , \quad (68)$$

where μ_0 is the permeability of free space, P_{gen} is the generator power density; i.e. total electrical power generated per unit volume, s_t is the structural material working stress, and ρ is its mass density.

- For a disk-type MHD generator, the coil alpha (α_{coil}) is given by

$$\alpha_{\text{coil}} = \frac{\sqrt{2}\pi\rho_c B}{\mu_0 j_c W_{\text{gen}}} \left(\frac{80W_{\text{gen}}}{\pi P_{\text{gen}}} \right)^{\frac{2}{3}} , \quad (69)$$

where j_c is the current density, ρ_c is the mass density of the coil material, W_{gen} is the total electrical power generated, s_t is the structural material working stress, and ρ is its mass density.

- For the thermal regenerator,

$$\alpha_{\text{regen}} = \frac{\beta_{\text{regen}}}{U_{\text{regen}}} \Delta T_{\text{LMD}} , \quad (70)$$

where β_{regen} is the mass per unit area; U_{regen} is the overall heat transfer coefficient, which is assumed to be constant; and ΔT_{LMD} is the log-mean temperature difference for the heat exchanger, and, referring to the various numbered temperature stations in figure 11, is defined as

$$\Delta T_{\text{LMD}} = \frac{(T_{10} - T_6) - (T_9 - T_7)}{\ln\left(\frac{T_{10} - T_6}{T_9 - T_7}\right)} , \quad (71)$$

where it is noted that, in the limit, as $|(T_{10} - T_6) / (T_9 - T_7)| \rightarrow 1$:

$$\Delta T_{\text{LMD}} = \frac{(T_{10} - T_6) + (T_9 - T_7)}{2} . \quad (72)$$

- For the compressor, the following expression is recommended:

$$\alpha_{\text{comp}} = 2 \times 10^{-5} \frac{\text{kg}}{\text{W}} . \quad (73)$$

Masses for the generator structure, M_{struc} ; generator coil, M_{coil} ; regenerator, M_{regen} ; and compressors, M_{comp} , can then be written as

$$M_{\text{struc}} = \alpha_{\text{struc}} W_{\text{gen}} , \quad (74)$$

$$M_{\text{coil}} = \alpha_{\text{coil}} W_{\text{gen}} , \quad (75)$$

$$M_{\text{regen}} = \alpha_{\text{regen}} Q_{\text{regen}} , \quad (76)$$

and

$$M_{\text{comp}} = \alpha_{\text{comp}} W_{\text{comp}} , \quad (77)$$

where W_{gen} is the total electrical power generated, Q_{regen} is the heat transferred by the regenerator, and W_{comp} is the electrical power required to run the compressors.

Each of these quantities can be expressed in terms of the mass flowrate of working fluid (m) its specific heat at constant pressure (c_p) and various other parameters:

$$W_{\text{gen}} = \eta_N T_{\text{max}} m c_p , \quad (78)$$

where η_N is the enthalpy extraction ratio and T_{\max} is the maximum temperature that the working fluid reaches in the reactor:

$$Q_{\text{regen}} = \varepsilon_{\text{regen}} \left[(1 - \eta_N) T_{\max} - \left(1 + \frac{1}{\eta_{s,c}} \left(R^{\frac{\gamma-1}{N_c \gamma}} - 1 \right) \right) \right] mc_p, \quad (79)$$

where $\varepsilon_{\text{regen}}$ is the regenerator effectiveness, defined as $[h_7 - h_6] / [h_9 - h_6]$, (see fig. 11 for details of the numbered stations), $\eta_{s,c}$ is the isentropic efficiency of a compressor stage, R is the overall pressure ratio, N_c is the number of compressor stages, and γ is the specific heats ratio for the working fluid:

$$W_{\text{comp}} = \frac{N_c}{\eta_{s,c}} \left[R^{\frac{\gamma-1}{N_c \gamma}} - 1 \right] T_{\min} mc_p, \quad (80)$$

where T_{\min} is the minimum temperature of the working fluid.

Equations (78)–(80) can be expressed in abbreviated form as follows:

$$W_{\text{gen}} = \Gamma_1 mc_p, \quad (81)$$

$$Q_{\text{regen}} = \Gamma_2 mc_p, \quad (82)$$

and

$$W_{\text{comp}} = \Gamma_3 mc_p, \quad (83)$$

where

$$\Gamma_1 \equiv \eta_N T_{\max}, \quad (84)$$

$$\Gamma_2 \equiv \varepsilon_{\text{regen}} \left[(1 - \eta_N) T_{\max} - \left(1 + \frac{1}{\eta_{s,c}} \left[R^{\frac{\gamma-1}{N_c \gamma}} - 1 \right] \right) \right], \quad (85)$$

and

$$\Gamma_3 \equiv \frac{N_c}{\eta_{s,c}} \left[R^{\frac{\gamma-1}{N_c \gamma}} - 1 \right] T_{\min}. \quad (86)$$

Equations (81) and (83) can then be used to derive an expression for the net electrical power generated; this latter quantity is clearly equal to the total electrical power generated minus that required to power the compressor(s) and is given by

$$W_{\text{gen}} - W_{\text{comp}} = (\Gamma_1 - \Gamma_3)mc_p , \quad (87)$$

which can then be used to eliminate m_{cp} from equations (81), (82), and (83):

$$W_{\text{gen}} = (W_{\text{gen}} - W_{\text{comp}}) \frac{\Gamma_1}{\Gamma_1 - \Gamma_3} , \quad (88)$$

$$Q_{\text{regen}} = (W_{\text{gen}} - W_{\text{comp}}) \frac{\Gamma_2}{\Gamma_1 - \Gamma_3} , \quad (89)$$

and

$$W_{\text{comp}} = (W_{\text{gen}} - W_{\text{comp}}) \frac{\Gamma_3}{\Gamma_1 - \Gamma_3} . \quad (90)$$

With these expressions, one can express the various masses (M_{struc} , M_{coil} , M_{regen} , and M_{comp}) in terms of the net electrical power generated ($W_{\text{gen}} - W_{\text{comp}}$):

$$M_{\text{struc}} = \alpha_{\text{struc}} (W_{\text{gen}} - W_{\text{comp}}) \frac{\Gamma_1}{\Gamma_1 - \Gamma_3} , \quad (91)$$

$$M_{\text{coil}} = \alpha_{\text{coil}} (W_{\text{gen}} - W_{\text{comp}}) \frac{\Gamma_1}{\Gamma_1 - \Gamma_3} , \quad (92)$$

$$M_{\text{regen}} = \alpha_{\text{regen}} (W_{\text{gen}} - W_{\text{comp}}) \frac{\Gamma_2}{\Gamma_1 - \Gamma_3} , \quad (93)$$

and

$$M_{\text{comp}} = \alpha_{\text{comp}} (W_{\text{gen}} - W_{\text{comp}}) \frac{\Gamma_3}{\Gamma_1 - \Gamma_3} . \quad (94)$$

Equivalently, an overall mass constant (α_{tot}) can be derived by

$$\alpha_{\text{tot}} = \frac{(\alpha_{\text{struc}} + \alpha_{\text{coil}})\Gamma_1 + \alpha_{\text{regen}}\Gamma_2 + \alpha_{\text{comp}}\Gamma_3}{\Gamma_1 - \Gamma_3} , \quad (95)$$

where

$$M_{\text{tot}} = M_{\text{struc}} + M_{\text{coil}} + M_{\text{regen}} + M_{\text{comp}} \quad (96)$$

$$= \alpha_{\text{tot}} (W_{\text{gen}} - W_{\text{comp}}) .$$

To support HOPE program mission analysis efforts, it is necessary to establish numerical values for the four alphas— α_{struc} , α_{coil} , α_{regen} , and α_{comp} —as well as the three gammas— Γ_1 , Γ_2 , and Γ_3 . In order to do this, several lower-level parameters must first be assigned reasonable numerical values, and they are given in table 24.

Table 24. Low-level parameters.

Parameter	Description	Units	Selected Value
R	Cycle pressure ratio	–	8
B	Magnetic field	T	8
P_{gen}	Power density in MHD generator	W/m ³	500×10 ⁶
(s_t/ρ)	MHD generator structural material working stress/mass density	J/kg	107×10 ³
μ_0	Permeability of free space	–	4 π ×10 ^{–7}
ρ_c	Mass density of coil material	kg/m ³	3,000
j_c	Current density in MHD generator	A/m ²	100×10 ⁶
W_{gen}	Total electrical power generated*	W	1×10 ⁶
β_{regen}	Regenerator mass per unit area	kg/m ²	1
U_{regen}	Regenerator overall heat transfer coefficient	W/(m ² ×K)	500
η_N	MHD generator enthalpy extraction parameter	–	0.4
T_{max}	Maximum working fluid temperature	K	2,500
T_{min}	Minimum working fluid temperature	K	500
$\varepsilon_{\text{regen}}$	Regenerator effectiveness	–	0.9
$\eta_{s,c}$	Compressor stage isentropic efficiency	–	0.87
N_c	Number of compressor stages	–	3
γ	Working fluid specific heats ratio	–	1.6667 (for GHe)

* Note that it is necessary to specify W_{gen} in order to calculate α_{coil} . As W_{gen} appears in the denominator of α_{coil} , selection of a relatively low value builds some additional conservatism into the resulting value.

Using the values from table 24, the following can be derived:

- $\alpha_{\text{struc}}=4.75977\times10^{-7}$ kg/W.
- $\alpha_{\text{coil}}=1.16586\times10^{-5}$ kg/W.
- $\alpha_{\text{regen}}=2.14203\times10^{-5}$ kg/W.
- $\alpha_{\text{comp}}=2\times10^{-5}$ kg/W.
- $\Gamma_1=1,000$.
- $\Gamma_2=734.7372989$.
- $\Gamma_3=550.8756704$.
- $\alpha_{\text{tot}}=8.65916\times10^{-5}$ kg/W.

REFERENCES

1. Troutman, P.A.; Bethke, K.; Stillwagen, F.; et al.: "Revolutionary Concepts for Human Outer Planet Exploration (HOPE)," *STAIF-2003 Conference Proceedings*, 20th Symposium on Space Nuclear Power and Propulsion, Albuquerque, NM, February 2-5, 2003.
2. Borowski, S.K.; McGuire, M.L.; Mason, L.S.; et al.: "'Bimodal' Nuclear Thermal Rocket (BNTR) Propulsion for an Artificial Gravity HOPE Mission to Callisto," *STAIF-2003 Conference Proceedings*, 20th Symposium on Space Nuclear Power and Propulsion, Albuquerque, NM, February 2-5, 2003.
3. McGuire, M.L.; Borowski, S.K.; Mason, L.S.; et al.: "High Power MPD Nuclear Electric Propulsion (NEP) for Artificial Gravity HOPE Missions to Callisto," *STAIF-2003 Conference Proceedings*, 20th Symposium on Space Nuclear Power and Propulsion, Albuquerque, NM, February 2-5, 2003.
4. Adams, R.B.; and Straw, T.: "Launch Vehicle Conceptual Design," Chapter 3 in *Space Launch and Transportation Systems*, Larson et al. (eds.), to be published 2003.
5. Thio, Y.C.F.; Freeze, B.; Kirkpatrick, R.C.; et al.: "High-Energy Space Propulsion Based on Magnetized Target Fusion," Proceedings of 35th AIAA/ASME/SAE/ASEE Joint Propulsion Conference and Exhibit, Los Angeles, CA, June 20-24, 1999. Paper No. AIAA 99-2703, 1999.
6. Sercel, J.; and Krauthamer, S.: "Multimegawatt Nuclear Electric Propulsion: First Order System Design and Performance Evaluation," Proceedings of AIAA Space Systems Technology Conference, San Diego, CA, June 9-12, 1986.
7. Buden, D.A.; Bennet, G.A.; Cooper, K.; et al.: "Selection of Power Plant Elements for Future Space Reactor Electric Power Systems," *LANL-7858*, Los Alamos Scientific Laboratory, Los Alamos, NM, September 1979.
8. Moyers, J.C.; and Nichols, J.P.: "ALKASYS—A Computer Program for Studies of Rankine Cycle Space Nuclear Power Systems," *ORNL-TM-10427*, September 1987.
9. Litchford, R.J.; Bitteker, L.J.; and Jones, J.E.: "Prospects for Nuclear Electric Propulsion Using Closed-Cycle Magneto-Hydrodynamic Energy Conversion," *NASA/TP-2001-211274*, Marshall Space Flight Center, AL, October 2001.
10. Patton, B.W.; and Sorensen, K.: "Application of Molten Salt Reactor Technology to MMW In-Space NEP and Surface Power Missions," Proceedings of 2002 ANS Annual Meeting, International Conference on Advanced Nuclear Power Plants, Hollywood, FL, June 9-13, 2002.
11. Philips, A.: "Launch Vehicle Analysis (LVA)," Marshall Space Flight Center.

12. Heller, J.A.; Moss, T.A.; and Barna, G.J.: "Study of a 300-Kilowatt Rankine-Cycle Advanced Nuclear-Electric Space-Power System," *NASA—TM—X—1919*, Cleveland, OH, November 1969.
13. Sauer, C.G.: "A Users Guide to VARITOP—A General Purpose Low-Thrust Trajectory Optimization Program," Jet Propulsion Laboratory, Pasadena, CA, November 4, 1991.
14. Williams, S.N.: "An Introduction to the Use of VARITOP—A General Purpose Low-Thrust Trajectory Optimization Program," Jet Propulsion Laboratory, Pasadena, CA, January 24, 1994.
15. Melbourne, W.G.; and Sauer, C.G.: "Performance Computations With Pieced Solutions of Planeto-centric and Heliocentric Trajectories for Low-Thrust Missions," *Supporting Research and Advanced Development, Space Programs Summary 37–36*, Vol. IV, pp. 14–19, Jet Propulsion Laboratory, Pasadena, CA, 1965.
16. Sandorff, P.E.: *Orbital and Ballistic Flight; An Introduction to Space Technology*, Massachusetts Institute of Technology, Department of Aeronautics and Astronautics, Cambridge, MA, 1960.
17. Irving, J.H.: "Lot-Thrust Flight: Variable Exhaust Velocity in Gravitational Fields," Chapter 10 in *Space Technology*, Howard Siefert (ed.), Wiley and Sons, New York, 1959.
18. Tsien, H.S.: "Take-off From Satellite Orbit," *J. Am. Rocket Soc.*, Vol. 23, pp. 233–236, 1953.
19. Hill, P.; and Peterson, C.: *Mechanics and Thermodynamics of Propulsion*, 2d ed., 752 pp., Addison-Wesley Publishing Co., Reading, MA, 1992.
20. "NASA Habitability Data Handbook, Vol 1," *MSC–03909*, 1971.
21. Woodson, W.E.; Tillman, B.; and Tillman P.: "Effects of Artificial Gravity Depend on Rotational Radius and Angular Velocity," *Human Factors Design Handbook*, 2d ed., by McGraw-Hill, New York, NY, 1992.
22. Bond, A. (ed.): "Project Daedalus Final Report," *JBIS* Supplement, 1978.
23. Malang, S.: "Proposal of a Blanket Concept Based on FliBe and Advanced Ferritic Steel," Proceedings of APEX Meeting, San Diego, CA, April 17–19, 2002.
24. Wittenberg, L.J.; Cameron, E.N.; Kulcinski, G.L.; et al.: "A Review of ^3He Resources and Acquisition for Use as a Fusion Fuel," *Fusion Technology*, Vol. 21, pp. 2230–2253, July 1992.
25. Roark, R.J.; Budynas, R.G.; and Young, W.C.: *Roark's Formulas for Stress and Strain*, McGraw-Hill, New York, NY, pp. 209–285, 1982.
26. "Astronautic Structures Manual, Volume 1," *NASA/TM—X—73305*, Marshall Space Flight Center, AL, August 1975.

27. Briesmeister, J.: "MCNP—A General Purpose Monte Carlo N-Particle Transport Code, Version 4C," *LANL-12625-M*, Los Alamos National Laboratory, Los Alamos, NM, March 1997.
28. Williams, C.H.; Dudzinski, L.A.; Borowski, S.K.; et al.: "Realizing '2001: A Space Odyssey': Piloted Spherical Torus Nuclear Fusion Propulsion," Proceedings of 37th AIAA/ASME/SAE/ASEE Joint Propulsion Conference and Exhibit, Salt Lake City, UT, July 8–11, 2001.
29. Orth, C.D.: "Interplanetary Space Transport Using Inertial Fusion Propulsion (UCRL-JC-129237 Rev. 1, April 20, 1998)," Proceedings of Ninth International Conference on Emerging Nuclear Energy Systems (ICENES '98), Tel-Aviv, Israel, June 28–July 2, 1998.
30. Wilson, J.W.; Badavi, F.F.; Cucinotta, F.A.; et al.: "HZETRN: Description of a Free-Space Ion and Nucleon Transport and Shielding Computer Program," *NASA/TP-3495*, Langley Research Center, Hampton, VA, May 1995.
31. Nealy, J.E.; Anderson, B.M.; Cucinotta, F.A.; et al.: "Transport of Space Environment Electrons: A Simplified Rapid-Analysis Computational Procedure," *NASA/TP-2002-211448*, Langley Research Center, Hampton, VA, March 2002.
32. Santarius, J.F.; and Sawan, M.E.: "Interim Progress Report for Research on Field Reversed Configuration and Magnetized-Target Fusion Propulsion: Covering the Period April 1–July 31, 2002," *NASA Project NAG8-1719*.
33. Litchford, R.J.; Bitteker, L.; and Jones, J.: "Prospects for Nuclear Electric Propulsion Using Closed-Cycle Magnetohydrodynamic Energy Conversion," Proceedings of 39th AIAA Aerospace Sciences Meeting & Exhibit, Paper No. *AIAA 2001-0961*, Reno, NV, January 8–11, 2001.

REPORT DOCUMENTATION PAGE			Form Approved OMB No. 0704-0188	
Public reporting burden for this collection of information is estimated to average 1 hour per response, including the time for reviewing instructions, searching existing data sources, gathering and maintaining the data needed, and completing and reviewing the collection of information. Send comments regarding this burden estimate or any other aspect of this collection of information, including suggestions for reducing this burden, to Washington Headquarters Services, Directorate for Information Operation and Reports, 1215 Jefferson Davis Highway, Suite 1204, Arlington, VA 22202-4302, and to the Office of Management and Budget, Paperwork Reduction Project (0704-0188), Washington, DC 20503				
1. AGENCY USE ONLY (Leave Blank)		2. REPORT DATE November 2003		3. REPORT TYPE AND DATES COVERED Technical Publication
4. TITLE AND SUBTITLE Conceptual Design of In-Space Vehicles for Human Exploration of the Outer Planets				5. FUNDING NUMBERS
6. AUTHORS R.B. Adams, R.A. Alexander, J.M. Chapman, S.S. Fincher, R.C. Hopkins, A.D. Philips, T.T. Polsgrove, R.J. Litchford, B.W. Patton, G. Statham,* P.S. White,* and Y.C.F. Thio**				
7. PERFORMING ORGANIZATION NAMES(S) AND ADDRESS(ES) George C. Marshall Space Flight Center Marshall Space Flight Center, AL 35812				8. PERFORMING ORGANIZATION REPORT NUMBER M-1087
9. SPONSORING/MONITORING AGENCY NAME(S) AND ADDRESS(ES) National Aeronautics and Space Administration Washington, DC 20546-0001				10. SPONSORING/MONITORING AGENCY REPORT NUMBER NASA/TP-2003-212691
11. SUPPLEMENTARY NOTES Prepared by the Program Planning and Development Office, Space Transportation Directorate *ERC, Inc., Huntsville, AL, **U.S. Department of Energy, Germantown, MD				
12a. DISTRIBUTION/AVAILABILITY STATEMENT Unclassified-Unlimited Subject Category 16 Availability: NASA CASI (301) 621-0390			12b. DISTRIBUTION CODE	
13. ABSTRACT (Maximum 200 words) During fiscal year 2002, a team of engineers from TD30/Advanced Concepts and TD40/Propulsion Research Center embarked on a study of potential crewed missions to the outer solar system. This study was conducted under the auspices of the Revolutionary Aerospace Systems Concepts activity administered by Langley Research Center (LaRC). The Marshall Space Flight Center (MSFC) team interacted heavily with teams from other Centers, including Glenn Research Center, LaRC, Jet Propulsion Laboratory, and Johnson Space Center. The MSFC team generated five concept missions for this project. The concept missions use a variety of technologies, including magnetized target fusion (MTF), magnetoplasmadynamic thrusters, solid core reactors, and molten salt reactors in various combinations. This Technical Publication (TP) reviews these five concepts and the methods used to generate them. The analytical methods used are described for all significant disciplines and subsystems. The propulsion and power technologies selected for each vehicle are reviewed in detail. The MSFC team also expended considerable effort refining the MTF concept for use with this mission. The results from this effort are also contained within this TP. Finally, the lessons learned from this activity are summarized in the conclusions section.				
14. SUBJECT TERMS fusion propulsion, nuclear electric propulsion, Jupiter, Callisto, Galilean moon, crewed vehicles			15. NUMBER OF PAGES 140	
			16. PRICE CODE	
17. SECURITY CLASSIFICATION OF REPORT Unclassified	18. SECURITY CLASSIFICATION OF THIS PAGE Unclassified	19. SECURITY CLASSIFICATION OF ABSTRACT Unclassified	20. LIMITATION OF ABSTRACT Unlimited	